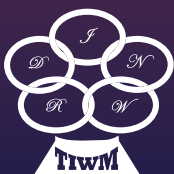


A photograph of a welding process, showing bright blue sparks and a glowing blue light emanating from a welding torch. The background is dark, making the sparks stand out.

Transactions on Intelligent Welding Manufacturing

Volume III No. 2 2019



 Springer

The Springer logo, which consists of a stylized chess knight (horse) facing right, positioned to the left of the word 'Springer'.

Transactions on Intelligent Welding Manufacturing

Editors-in-Chief

Shanben Chen
Shanghai Jiao Tong University
Shanghai, China

Yuming Zhang,
Department of Electrical
and Computer Engineering
University of Kentucky
Lexington, KY, USA

Zhili Feng,
Oak Ridge National Laboratory
Oak Ridge, USA

Honorary Editors

G. Cook, USA
K. L. Moore, USA
Ji-Luan Pan, PRC
S. A. David, USA

S. J. Na, KOR
Lin Wu, PRC
Y. Hirata, JAP
J. Norrish, AUS

T. Lienert, USA
T. J. Tarn, USA

Guest Editors

H. P. Chen, USA
J. C. Feng, PRC
H. J. Li, AUS

X. Q. Chen, NZL
D. Hong, USA
W. Zhou, SGP

D. Du, PRC
X. D. Jiao, PRC

D. Fan, PRC
I. Lopez-Juarez, MEX

Regional Editors

Asia: L. X. Zhang, PRC
America: Y. K. Liu, USA

Australia: Z. X. Pan, AUS
Europe: S. Kononov, RUS

Associate Editors

Q. X. Cao, PRC
B. H. Chang, PRC
J. Chen, USA
H. B. Chen, PRC
S. J. Chen, PRC
X. Z. Chen, PRC
A.-K. Christiansson, SWE
Z. G. Li, PRC
X. M. Hua, PRC

Y. Huang, USA
S. Kononov, RUS
W. H. Li, PRC
X. R. Li, USA
Y. K. Liu, USA
L. M. Liu, PRC
H. Lu, PRC
Z. Luo, PRC
G. H. Ma, PRC

Pedro Neto, PRT
G. Panoutsos, UK
Z. X. Pan, AUS
X. D. Peng, NL
Y. Shi, PRC
J. Wu, USA
J. X. Xue, PRC
L. J. Yang, PRC
M. Wang, PRC

S. Wang, PRC
X. W. Wang, PRC
Z. Z. Wang, PRC
G. J. Zhang, PRC
H. Zhang, B, PRC
H. Zhang, N, PRC
L. X. Zhang, PRC
W. J. Zhang, USA

Academic Assistant Editors

J. Cao, PRC
B. Chen, PRC
Y. Luo, PRC
N. Lv, PRC
F. Li, PRC

S. B. Lin, PRC
Y. Shao, USA
Y. Tao, PRC
J. J. Wang, PRC
H. Y. Wang, PRC

S. L. Wang, PRC
J. Xiao, PRC
J. J. Xu, PRC
Y. L. Xu, PRC
C. Yu, PRC

H. W. Yu, PRC
K. Zhang, PRC
W. Z. Zhang, PRC
Z. F. Zhang, PRC

Editorial Staff

Executive Editor (Manuscript and Publication):

Dr. Yan Zhang, PRC

Responsible Editors (Academic and Technical):

Dr. Na Lv, PRC

Dr. Jing Wu, USA

More information about this series at <http://www.springer.com/series/15698>

Shanben Chen · Yuming Zhang · Zhili Feng
Editors

Transactions on Intelligent Welding Manufacturing

Volume III No. 2 2019

 Springer

Editors

Shanben Chen
Shanghai Jiao Tong University
Shanghai, China

Zhili Feng
Oak Ridge National Laboratory
Oak Ridge, TN, USA

Yuming Zhang
Department of Electrical
and Computer Engineering
University of Kentucky
Lexington, KY, USA

ISSN 2520-8519

ISSN 2520-8527 (electronic)

Transactions on Intelligent Welding Manufacturing

ISBN 978-981-15-6921-0

ISBN 978-981-15-6922-7 (eBook)

<https://doi.org/10.1007/978-981-15-6922-7>

© Springer Nature Singapore Pte Ltd. 2020

This work is subject to copyright. All rights are reserved by the Publisher, whether the whole or part of the material is concerned, specifically the rights of translation, reprinting, reuse of illustrations, recitation, broadcasting, reproduction on microfilms or in any other physical way, and transmission or information storage and retrieval, electronic adaptation, computer software, or by similar or dissimilar methodology now known or hereafter developed.

The use of general descriptive names, registered names, trademarks, service marks, etc. in this publication does not imply, even in the absence of a specific statement, that such names are exempt from the relevant protective laws and regulations and therefore free for general use.

The publisher, the authors and the editors are safe to assume that the advice and information in this book are believed to be true and accurate at the date of publication. Neither the publisher nor the authors or the editors give a warranty, expressed or implied, with respect to the material contained herein or for any errors or omissions that may have been made. The publisher remains neutral with regard to jurisdictional claims in published maps and institutional affiliations.

This Springer imprint is published by the registered company Springer Nature Singapore Pte Ltd. The registered company address is: 152 Beach Road, #21-01/04 Gateway East, Singapore 189721, Singapore

Editorials

This issue of the Transactions on Intelligent Welding Manufacturing (TIWM) is a collection of high-quality contributions recommended by “2018 International Conference on Robotic Welding, Intelligence and Automation (RWIA’2018)”. It includes one feature article, six research papers and two short papers.

The featured article in this issue is the first paper “[Hybrid Intelligence Problems in Intelligentized Welding Manufacturing Systems](#)” contributed by Prof. Shanben Chen, Cheung Kong Scholar, from Shanghai Jiao Tong University. This paper discusses artificial intelligence-based scientific methods for complex systems and their applications in intelligentized welding manufacturing technology/systems/workshop/factory (IWMT/S/W/F).

The first research paper “[Double Electrode Micro-plasma Arc Welding Curved Surface Part Additive Manufacturing Control System](#)” is contributed by Ding Fan, Nan Li, Jiankang Huang, Shurong Yu, Wen Yuan from the Lanzhou University of Technology. Aiming at key problems in wire and arc additive manufacturing, this paper uses the principle of bypass coupled arc welding and the method of the micro-plasma arc welding to build a DE-MPAW additive manufacturing control system. This system takes the UG/NX as the supporting platform and creates the DE-MPAW additive manufacturing rapid prototyping system arc tool library, which helps realize the integration and automation of curved parts from 3D models.

The second research paper “[Arc Contraction Behavior of GMA Welding Process Based on Change of Arc Length at Hyperbaric Air Condition](#)” contributed by a research team from Beijing Institute of Petrochemical Technology studies the underwater hyperbaric dry GMA welding that is considered one of the best emergency maintenance methods for underwater structures. In order to find the main factors that affect the GMA welding quality, theoretical analysis, numerical simulation and experimental verification are conducted to study the contraction behavior of GMAW arc under high pressure. The results show that the axial and radial dimensions of hyperbaric GMA welding arc decrease with the increase of ambient pressure, showing the phenomenon that the arc contraction increases the frequency of short-circuit drop transfer and affects the stability of the welding process.

The third research paper titled “[Online Defect Detection of Laser-Arc Hybrid Welding Based on Spectral Information and MSPC](#)” is contributed by researchers from Harbin Institute of Technology and Harbin Institute of Technology at Weihai. This paper studies online monitoring of welding quality. In this paper, a quality detection system for laser arc hybrid welding process has been established by using a spectrometer. Principal component analysis (PCA) and multivariate statistical process control (MSPC) were used to analyze the collected spectral information. The results showed that the welding defects could be effectively detected by selecting the specific elements.

The fourth research paper, “[Research on Laser DP-TIG Hybrid Thin Plate High-Speed Welding Process](#)”, is from Zhu Jialei, Feng Cong, Jiao Xiangdong, Li Zhibo, Li Wei, affiliated with Beijing Institute of Petrochemical Technology, China. Compared with traditional TIG welding, deep penetration TIG welding can effectively increase weld penetration and improve welding efficiency. This paper explores the maximum welding speed that can be achieved by laser DP-TIG hybrid welding. The results show that the laser DP-TIG hybrid welding can significantly improve the welding speed and has good adaptability to the gap and misalignment.

The fifth research paper, “[Influence of Welding Sequence on Welding Deformation of T-Joint](#)”, is from Guilin University of Electronic Technology and Beibu Gulf University. This paper simulates three practical welding processes and studies the effect of welding sequence on distortion. The results show that the final distortion by cross-back welding and simultaneous back welding is smaller, while the requirements of cross-back welding on the process are lower.

The last research paper in this issue, “[Research on Machine Vision Image Mosaic Algorithm for Multi-workpiece Cutting Platform](#)”, is a contribution from Beijing Institute of Petrochemical Technology. To reduce the complexity of the algorithm on the basis of ensuring the stitching precision, this paper studies an image stitching algorithm, which uses ROI to limit the image-matching feature points in the region of interest. The algorithm uses ORB algorithm to extract feature points, determine the main direction of feature points and describe the detected feature points.

Short paper “[Intelligent Welding Technology for Large Deep and Narrow Shaped Box with Robot](#)” is from Zhejiang Normal University and Shanghai Zhenhua Heavy Industries Co., Ltd. In this paper, a fast parameter programming system suitable for robot welding of shaped box is developed. A composite sensing method-based arc tracking is proposed, which overcomes the difficulty of positional accessibility of deep and narrow lattice space and the longtime and single contact of traditional online/offline task programming.

The second short paper “[Optimization of Laser Deep Penetration TIG Hybrid Welding Technology for Stainless Steel](#)” is from Beijing University of Chemical Technology and Beijing Institute of Petrochemical Technology. A laser deep penetration TIG welding machine is used in hybrid welding. This paper analyzes the influence of the main process parameters on weld forming. High-quality weld is obtained.

This issue of TIWM demonstrates new perspectives and developments in the field of intelligent welding research, as well as the topics related to the RWIA'2018 conference. All contributions from this issue are expected to provide new inspirations to our loyal readers, either researchers or practitioners in the field of intelligent welding manufacturing.

Yuming Zhang Ph.D.
TIWM Editor-in-Chief
yuming.zhang@uky.edu

James R. Boyd
Professor of Electrical Engineering, University of Kentucky
Fellow, American Welding Society (AWS)
Fellow, American Society of Mechanical Engineers (ASME)
Fellow, Society of Manufacturing Engineers (SME)

Contents

Feature Articles

| | |
|--|---|
| Hybrid Intelligence Problems in Intelligentized Welding Manufacturing Systems | 3 |
| Shanben Chen | |

Research Papers

| | |
|--|----|
| Double-Electrode Micro-plasma Arc Welding Curved Surface Part Additive Manufacturing Control System | 35 |
| Ding Fan, Nan Li, Jiankang Huang, Shurong Yu, and Wen Yuan | |
| Arc Contraction Behavior of GMA Welding Process Based on Change of Arc Length at Hyperbaric Air Condition | 47 |
| Jiqiang Huang, Wenwen Guo, Junfen Huang, Long Xue, Jizong Wang, and Yong Zou | |
| Online Defect Detection of Laser-Arc Hybrid Welding Based on Spectral Information and MSPC | 61 |
| Chengyuan Ma, Bo Chen, Caiwang Tan, Xiaoguo Song, and Jicai Feng | |
| Research on Laser DP-TIG Hybrid Thin Plate High-Speed Welding Process | 73 |
| Jialei Zhu, Cong Feng, Xiangdong Jiao, Zhibo Li, and Wei Li | |
| Influence of Welding Sequence on Welding Deformation of T-Joint | 83 |
| Yong Qin, Ziquan Jiao, Zhiqiang Feng, Nanhui Shi, Junfeng Han, and Xian Wei | |

Short Papers and Technical Notes

**Research on Machine Vision Image Mosaic Algorithm
for Multi-workpiece Cutting Platform** 101
Long Xue, Yingyu Cao, Junfen Huang, Jiqiang Huang, Zhengyu Zhang,
Lanlan Bai, and Jianting Xi

**Intelligent Welding Technology for Large Deep and Narrow Shaped
Box with Robot** 113
Hu Lan, Huajun Zhang, Jun Fu, Libin Gao, and Rui Pan

**Optimization of Laser Deep Penetration TIG Hybrid Welding
Technology for Stainless Steel** 123
Jialei Zhu, Wei Li, Zhibo Li, Xiangdong Jiao, Cong Feng, and Kai Wang

Information for Authors 131

Author Index 133

Feature Articles

Hybrid Intelligence Problems in Intelligentized Welding Manufacturing Systems



Shanben Chen

Abstract This paper discusses the intelligent scientific methods in the complex system produced by the compound application of AI technology in the intelligentized welding manufacturing technology/systems/workshop/factory (IWMT/S/W/F), which are being researched and developed in the hot spot at present, i.e., the hybrid intelligence problems in the IWMT/S. Based on the technological constitution of the IWMT/S, the paper investigates the hybrid or compound, multiple and mixed effects of different intelligent methods and technologies applied in IWMT/S, which includes the hybrid intelligence problems existing in multi-information sensing, knowledge modeling of arc welding process and intelligent control methodology for welding dynamic process, and the hybrid intelligence problems existing in intelligentized technologies for robotic welding process and systems. A IWMW for piles and legs of the offshore platform with the pentabasic structure function of the IWMT is shown, and the HI features of the intelligent pentabasic technology, systems and methodology of the IWMW for the platform and the hybrid intelligent function of the IWMW are analyzed in this paper.

Keywords Hybrid intelligence problems · Intelligentized welding manufacturing · IWMT/S/W/F · Artificial intelligence (AI) · Robotic welding · Multi-information sensing · Knowledge modeling · Intelligent control · Arc welding process

1 Introduction

It is well known that welding technology has experienced the development course of semi-mechanization, automatic welding and robot welding from the traditional handicraft operation [1–5]. It has become an inevitable trend to adopt the machine instead of the manual welding, i.e., the modern welding from handicraft to scientific manufacturing, intelligentized welding manufacturing (IWM) [1, 6, 7].

S. Chen (✉)

Intelligentized Robotic Welding Technology Laboratory (IRWTL), School of Materials Science and Engineering, Shanghai Jiao Tong University (SJTU), Shanghai 200240, China
e-mail: sbchen@sjtu.edu.cn

The intelligentized welding manufacturing (IWM) is to simulate intelligent behaviors and functions of the human's sense, brain and body activity in welding process of various manufacturing products by the artificial intelligence (AI) technology about in recent two decades [8–10]. And the IWM undoubtedly is the most representative in the smart/intelligent manufacturing techniques of all modern industries.

Many scholars have explored the application of various AI methods and technologies to intelligentized welding manufacturing processes and systems [11–14], such as that multi-source information sensing technologies such as computer vision, arc sound, spectrum and so on are used to obtain welding process information [8]; the AI algorithms and techniques, such as machine learning and data mining, are used to extracting and modeling of the knowledge in welding process [9]; and various intelligent control methods, such as fuzzy logic, neural network, self-learning and adaptive control, are used to realize intelligent control of welding dynamic process and its complex system [10].

And the combination of various intelligent sensing, information processing, knowledge modeling and control algorithms and methods is integrated into highly complex and intelligent welding systems, such as robotic welding workstations, automatic welding production line and intelligent welding workshop/factory.

In the previous published literature, the intelligent welding technology, the system and the intelligent structure of the intelligentized welding manufacturing workshop are put forward in [6, 7]. References [8, 15–40] show the research of multi-information sensing and fusion algorithm for visual image of welding zone, arc sound, arc spectrum, current and voltage, position track deviation and so on in the welding dynamic process. Many intelligent methods such as data-driven, system identification, fuzzy identification, artificial neural network, support vector machine, rough set, Petri net and multi-agent are presented for welding process and intelligent modeling method of robot welding system and complex welding manufacturing system in [9, 15, 16, 41–53]. References [10, 15, 16, 54–61] show various intelligent control methods, such as classical PID, adaptive, self-learning, neural network, fuzzy control, neural network control, hybrid logic dynamic (MLD), expert control, and their combined or composite control algorithms and methods, for realized intelligent control of weld pool dynamics, weld seam tracking, welding seam forming and complex intelligent welding system.

It is obvious, in the above-mentioned use of various welding process sensing, information processing, knowledge modeling and real-time intelligent control methods and algorithms to achieve results, and the inevitable scientific and technological implementation problems are the combination of these intelligent methods and algorithms based on different theories, different description forms and different implementation methods, i.e.,

How to evaluate the controlled processes and the effects of combination or mixing with various intelligent algorithms and methods?

How to analyze and construct the most reasonable or optimal composite or hybrid intelligent algorithms and methods in order to achieve the optimal control objectives for the controlled object?

The above-mentioned problems are not only the confusion of the hybrid intelligent control method used in the complex intelligent welding system. At the same time, it is also the most challenging problem to realize the disordered application of artificial intelligence technology in a large number of intelligent manufacturing systems.

The second part of this paper will describe the existing general concepts and problems of hybrid intelligence in complex intelligent systems and related research work. The third part of this paper will classify and analyze the intelligent methods and algorithms existing in the intelligent control of welding process and robot welding system. Furthermore, the hybrid intelligence problem in intelligentized welding manufacturing process and system is put forward. In the fourth part of this paper, some examples of hybrid intelligent sensing, modeling and control methods in intelligentized welding manufacturing process and system are presented, and some preliminary analysis results are given. In the last part of this paper, we will discuss the future research direction of hybrid intelligence problem in intelligentized welding manufacturing process and system.

2 Hybrid Intelligence Problems in General Intelligent Systems

Since Minsky, McCarthy and other scholars put forward the concept of artificial intelligence (AI) in the 1950s, the AI has made some epoch-making achievements, for example, with the development and composite application of many AI technologies, such as perceptron, fuzzy set theory, expert system, error backpropagation algorithm, genetic algorithm, particle swarm optimization and so on. Many scholars have noticed that with the combination of various AI methods and the complexity of composite and integrated applications [62–64]. As early as 1991, Minsky, a famous expert in the field of AI, recognized the necessity of studying artificial intelligence systems composed of different intelligent technologies in [65]. Furthermore, in the 1990s, a new research direction in the field of AI, hybrid intelligent system (HIS), has been put forward in [66].

The HIS is an updated research direction with the development of AI, the purpose of which is to make the complicated intelligent system more effective in knowledge representation, reasoning, management and so on [64–80].

2.1 *The Preliminary Concept of Hybrid Intelligent Systems*

At present, there is no uniform definition on the concept of hybrid intelligent system (HIS) in AI academia [62, 64]. The early definition simply considered the HIS as an integrated system composed of expert system and artificial neural network, or considered that any system with two or more intelligent technologies is a HIS. Later, with

the addition of genetic algorithm, evolutionary computation, fuzzy logic, immune algorithm and traditional hard computing technology, the HIS has been developed into a special research direction of AI.

From now on, there are two academic concepts leading the research of hybrid intelligent system. One is “computational intelligence,” which focuses on hybrid intelligent systems as a combination of new computational intelligence and traditional artificial intelligence “symbolism” [67]. The other is “intelligent application,” which mainly investigates the HIS with integration of “soft computing” and “hard computing” in various AI technologies, that is, so that the problems in reality can be solved better [68].

Therefore, the HIS can be summed up as an intelligent system with integrating at least one intelligent technology and non-intelligent technology for complex practical problems in order to obtain a better knowledge representation, reasoning and problem-solving capabilities, and run robust and more efficient applications.

2.2 Research on Theory of Hybrid Intelligent System

The theoretical research of hybrid intelligent system mainly includes the research motivation, the classification, the construction method, the evaluation criterion of hybrid intelligent system and so on, as follows.

The motivation of hybrid intelligent system

- The idea of hybrid intelligent system is to overcome the deficiency of single technology.
- The hybrid intelligent system is proposed because a single technology cannot solve all the subproblems of practical application problems.
- The hybrid intelligent system uses a hybrid structure to realize the ability of multi-information processing, which is better than the single intelligent technology imitating human intelligence.

The classification of hybrid intelligent system

- According to the structure of the HIS, the HIS is divided into: stand-alone models, transformation models, loose-coupling models, tight-coupling models, fully integrated models [69].
- According to the motivation of the study, the HIS is divided into: function replacing hybrids, intercommunicating hybrids and polymorphic hybrids [70]. This paper analyzes whether these hybrid intelligent systems, which are grouped into one class because of “common reason,” have any common ground in the choice of concrete construction methods.
- According to the different fusion forms of “soft computing” and “hard computing,” HIS is divided into seven categories: There are mainly isolated, parallel, feedback, cascaded, designed, augmented, assisted [71].

The HIS is classified from the point of view of system theory, especially the input and parameter value of the system are considered. In addition, some papers [72, 73] have studied the classification of the HIS.

The construction method of hybrid intelligent system

The construction method of HIS is one of the most important research fields in HIS. It is not only the most operational part of the methodology of HIS, but also the least studied part of HIS [74]. The main research reports are as follows:

Goonatilake first put forward a six-stage development method of HIS [70]: problem analysis, prototype matching, hybrid category selection, implementation, validation and maintenance. The problem analysis is mainly to determine the sub-task and its attributes, prototype matching is mainly to select the appropriate technology for each sub-task, and the hybrid category selection is to select the type selection of the HIS to be used. The six-stage development method proposed in reference [70] is carried out according to the steps of information system development, which is of great significance to the development of a new HIS.

In recent years, some scholars have proposed a HIS construction method based on agent. According to the dynamic interaction characteristics of agent, Zhang proposed “agent-based hybrid intelligent system framework” [75]. The framework is composed of interactive agent, planning agent, problem-solving agent, synthetic agent, intermediate agent and various technology agents. The most important part is the intermediate agent, which mainly stores the capability of each technology and retrieves the ability according to the demand. Li et al. also proposed a HIS framework based on agent (MAHIS [76]), which consists of eight models: hybrid strategy identification model, organization model, task model, agent model, specialist model, coordination model, etc., reorganize model and design model. The “agent-based hybrid intelligent system framework” can be built independently according to the needs of the task, but the problem of this framework is that it must be described according to the problem to be solved. They are stored in agent in the form of ontology, and problem-solving agent must have knowledge in this field, which is difficult to achieve.

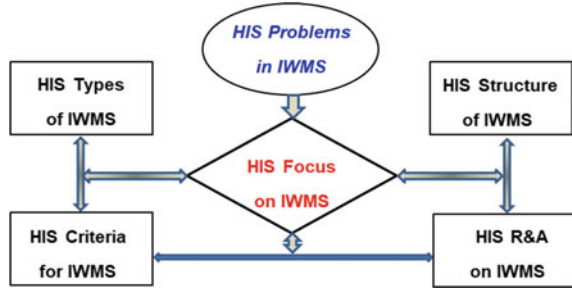
The evaluation criteria of hybrid intelligent system

It is of great significance to determine the evaluation criteria for hybrid intelligent systems to guide the design and construction of hybrid intelligent systems. At present, there is little systematic research in this area, which is basically the evaluation of the results of hybrid intelligent system.

The evaluation criteria proposed by Hefny et al. in [77] include: error level, training process, structural complexity, reasoning capability. Reference [77] also pointed out that with the increase of various technologies used in the mixing process, there may be problems in coupling, structural complexity, learning algorithm and computational complexity of the system.

In the process of studying the industrial data analysis, according to the developing process of the hybrid intelligent system, Kordon put forward the evaluation criterion of the HIS [78]: robustness, speed and cost of the development process; sensitivity to change; self-evaluation of performance; and maintenance costs.

Fig. 1 HIS problems for the IWMS



To sum up, we summarize the research background, motivation content and key problems of general HIS in the following diagram, Fig. 1, including the relationship between the types, structures, criteria and application effects of HIS for the IWMS.

3 Hybrid Intelligence Problems in Intelligentized Welding Manufacturing Systems

3.1 The Intelligent Functions and Structure of IWMT/S

In our previous published literature [1, 6, 7], we have put forward and expounded the conceptual and technical framework of intelligentized welding manufacturing (IWM), intelligentized welding manufacturing technology/system (IWMT/S), intelligentized robotic welding technology/system (IRWT/S), intelligentized welding manufacturing engineering (IWME) and so on. Of course, it is mainly aimed at the most representative arc welding process without losing its generality.

In Ref. [1], the intelligentized welding manufacturing (IWM) is preliminarily defined as for simulating intelligent behaviors and functions of welder's sense, brain and body activity in welding process by the artificial intelligence technology; see Fig. 1 for composition parts of the IWM process. Furthermore, investigating the constitution of general intelligentized manufacturing, functions and systems, we present a pentabasic framework of intelligentized functions in the IWMS, as shown in Fig. 2.

Replacing manual welding with machines, which is also a dream that has been pursued by welding practitioners for thousands of years, Fig. 3, it also is the key technology of the IWM, i.e., IRWT in Fig. 4.

Based on scientific and technical contents related to development of modern welding manufacturing technology, the concept on intelligentized welding manufacturing technology (IWMT) is introduced [1, 6, 7], and it shows for the key scientific and technical formwork of the IWMT, which contains three advanced manufacturing fields: the virtual and digital welding manufacturing and technology (V&DWMT) including the virtual manufacturing; intelligentized robotic welding

Fig. 2 A pentabasic framework of intelligentized functions in the IWMS

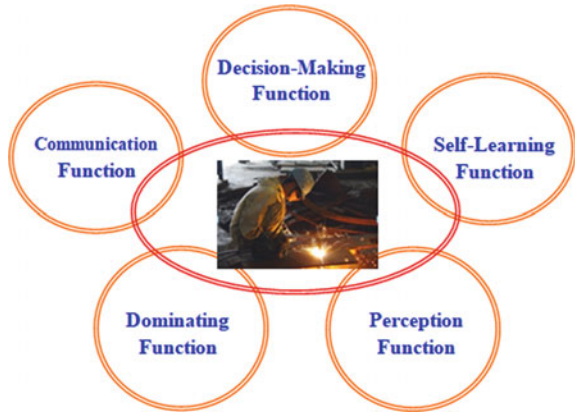
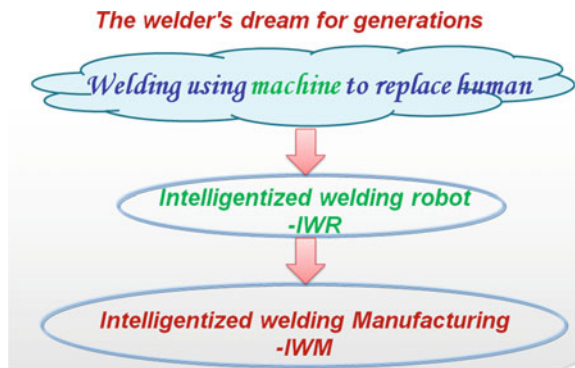


Fig. 3 Welder’s dream for generations: IWR to IWM



technology (IRWT) and the flexible and agile welding manufacturing and technology (F&AWMT); and key technical elements and system techniques of the IWMT including the network manufacturing.

In the process and systems of the IWM for the large equipment, a composition of the IWME/T/S is shown in Fig. 4.

For example, in an intelligentized welding manufacturing workshop/factory for major equipment, corresponding to the pentabasic intelligence functions in Fig. 2, it can be summarized as follows: a functional diagram of IWMW’s pentabasic framework of the IWMS, as shown in Fig. 5.

The Fig. 5 shows an IWMW construction, its core technology is the IWT and its IWMS, which can be divided into five types of technologies, such as the WT, RT, NT, IT, and DT. And constitute the corresponding five kinds of intelligent systems, such as the MS, FS, DS, IS and VS.

Obviously, in the above-mentioned IWMT/S, it involves the combination or mixed application of a variety of AI techniques and methods.

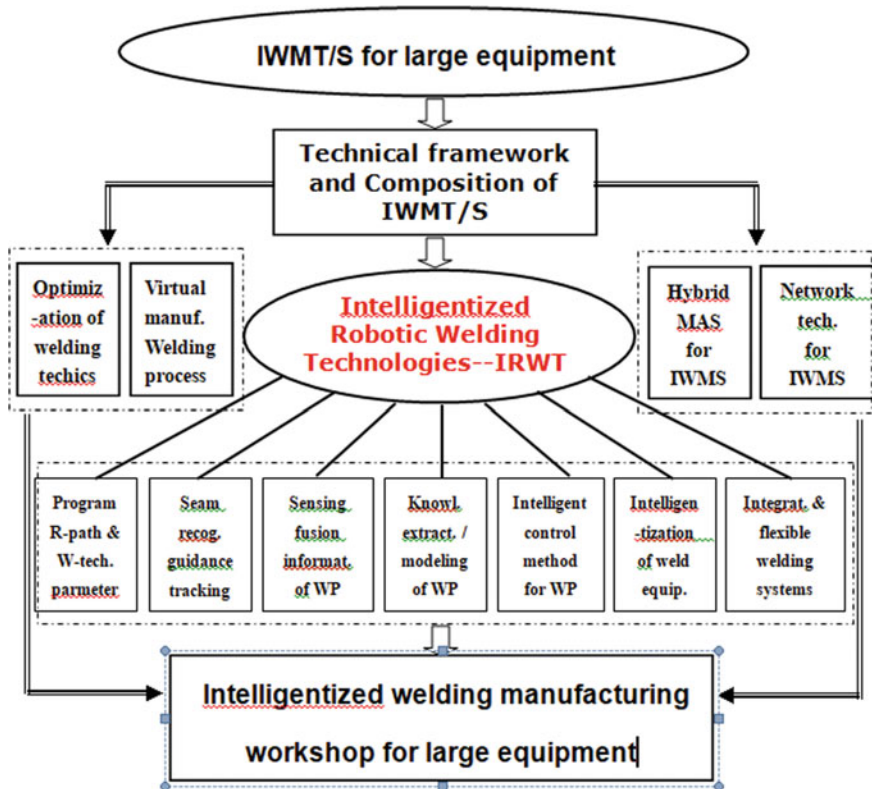
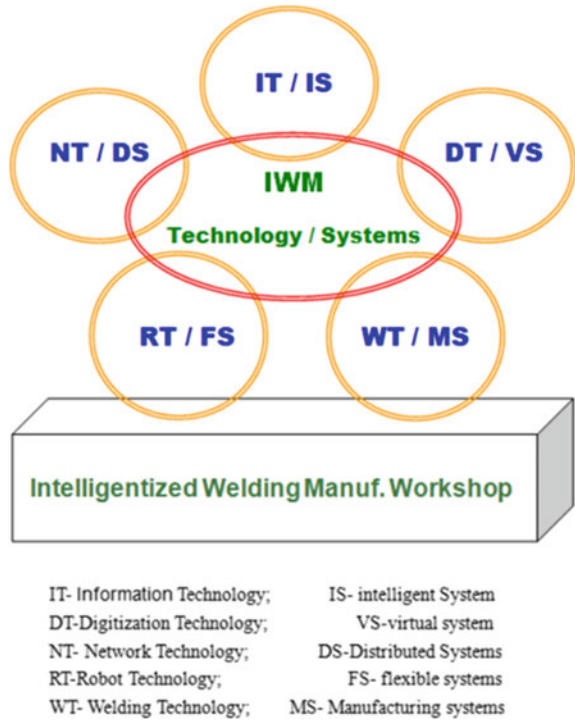


Fig. 4 A composition of IWME/T/S for a large equipment

As one can see, the IWMT/S involves three key elements of intelligentized technology for welding process and systems: sensing welding process for imitating welder’s sense organ function, knowledge extraction and modeling of welding process for imitating welder’s experience reasoning function and intelligent control of welding process for imitating welder’s decision-making operation function.

In the research literature published by us and other scholars, the various AI techniques and methods used in the welding process and system under different conditions are shown, such as the optimal planning of robot welding task, process and its parameters. The AI includes the fuzzy logic, neural networks, expert systems, data mining, knowledge extraction and modeling, machine learning, adaptive and self-learning control algorithms and combination of these different algorithms. In the intelligent welding process, sensing, information processing, feature extraction, knowledge modeling and feedback control methods and algorithms, there are a lot of problems in the analysis and optimization of hybrid intelligence phenomenon and hybrid intelligent action process. In the past, only the sensing of specific processes and systems has been studied. Modeling and control are a very important and practical AI complexity problem that has not attracted attention or been specifically discussed.

Fig. 5 A pentabasic framework of the IWMW



It is also an unavoidable bottleneck and challenge in the theory and application of hybrid intelligent algorithms and techniques. Therefore, this paper seriously put forward in order to attract scientists and engineers’ enough attention on a so-called hybrid intelligence problem in the IWM process and systems.

One can see the following examples of hybrid intelligence in the IWMS.

3.2 Hybrid Intelligence Features of Multi-information Processing and Fusion for Arc Welding Process

HI features of acquisition and processing of multi-source information in GTAW process

In the Refs. [8, 15–40], the multi-information and complexity in arc welding dynamical process are presented in Fig. 6, which includes four categories, such as welding process, arc, vision and motion information, and about 20 kinds of measurable information that occur during welding in Fig. 6.

The experimental system with multiple sensors and acquisition for sensing and acquiring arc, sound, spectrum and other signals in the dynamic process of GTAW established in SJTU’s Robot Welding Intelligent Technology Laboratory is shown

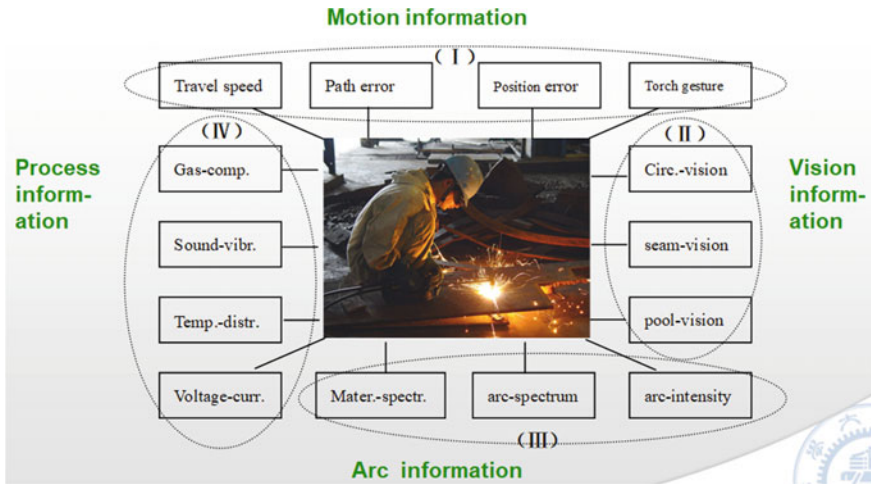


Fig. 6 Multi-information and complexity in arc welding dynamical process

in Fig. 7, which includes vision, sound, spectrum sensors for arc features during the pulsed GTAW. Based on the above experimental system, Fig. 8 shows experimental results of arc voltage, arc sound, spectrum, weld pool image and other signals during the pulsed GTAW dynamic process.

The image information features of the weld pool are also shown in Fig. 8, which are unwelded or under-penetration, as well as burn-through or weld leakage.

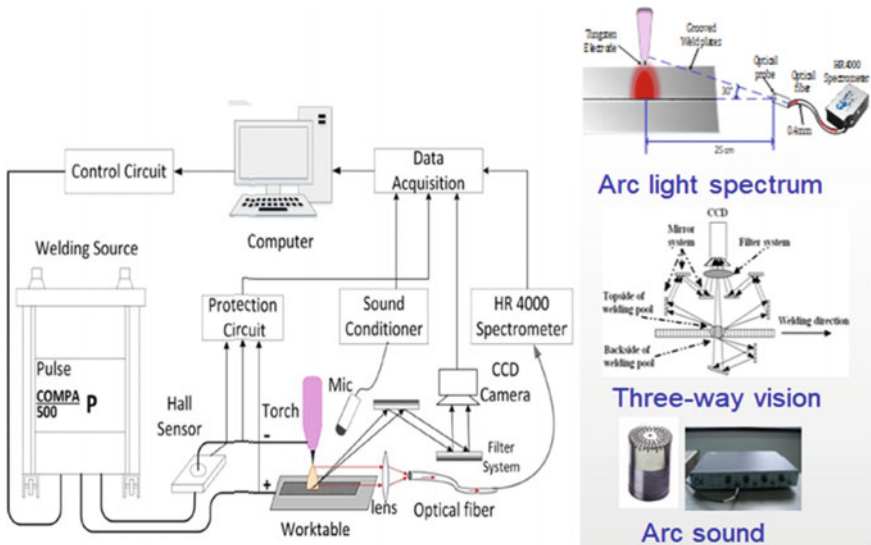
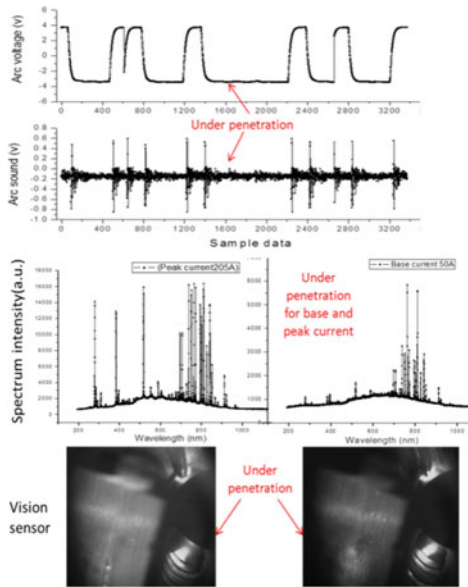
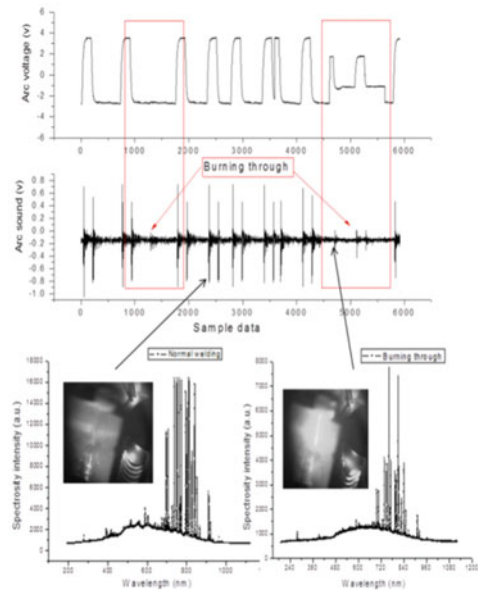


Fig. 7 Multiple signal acquisition systems for pulsed GTAW

Fig. 8 Arc voltage, sound, spectrum and image information during pulsed GTAW



(a) Defect of under penetration



(b) Defect of burning through

Among these methods to process the multi-information features, there are many different intelligent computing methods and their hybrid application. The mixed effect of hybrid intelligent processing algorithms is obviously a very important problem, and it is needed for further analysis and investigation.

HI features of multi-information fusion algorithms for predicting welding penetration in GTAW dynamical process

In Refs. [9, 26–28, 40], the method and algorithm of multi-source information fusion in welding process are studied and discussed. Based on the information of arc voltage, visual image and arc sound in GTAW process, intelligent processing algorithm is used to extract penetration features, and then multi-information feature layer fusion method and neural network and DS evidence algorithm are used to predict welding penetration.

HI features of multi-information fusion for arc welding dynamical process

Summarized our research and current literature [9, 26–28, 40], a variety of intelligent processing algorithm and multi-information fusion methods and their algorithms are used in the welding dynamic process for monitoring and quality prediction of welding process, and the combination of various intelligent algorithms or hybrid features can be seen in the following illustration; i.e., various combined or hybrid intelligent algorithms have been widely used in multi-source information fusion algorithms, such as sensing, feature extraction, classification and prediction for welding dynamic process, shown in Fig. 9.

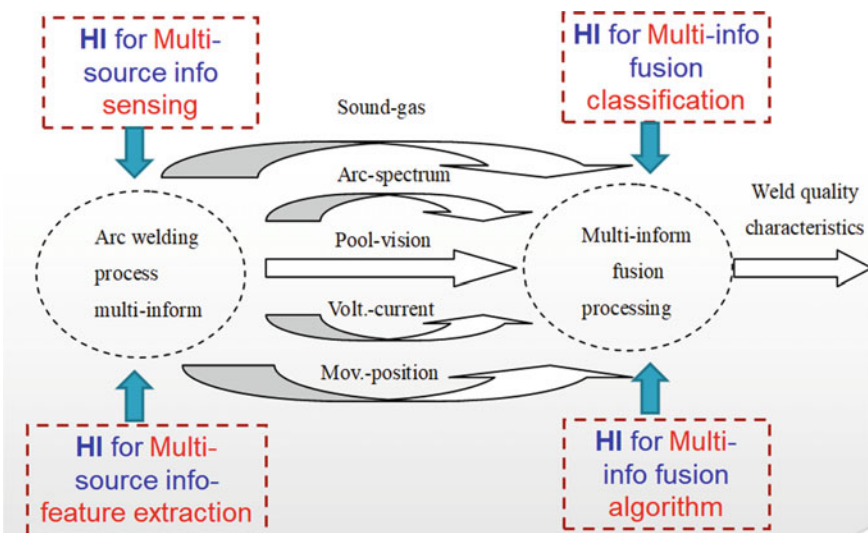


Fig. 9 HI features of multi-information acquisition and processing of arc welding process

3.3 Hybrid Intelligence Features in Intelligent Modeling Methodology for Welding Dynamic Process

In the literature on modeling method of welding dynamic process [9, 15, 16, 41–53], several typical methods and algorithms of intelligent modeling for welding process can be summarized as shown in Fig. 10.

The intelligent modeling methods for welding dynamic process are given as follows:

- Knowledge modeling class: including expert system, fuzzy logic, empirical rules, rough set, identification modeling and so on;
- Artificial neural network (ANN) modeling class: including support vector machine, genetic algorithm, ant colony algorithm and other methods;
- Multi-agent, hybrid logic dynamics, various programming and optimization algorithm modeling methods, etc.;
- The combination of modeling methods and algorithms of various intelligent algorithms mentioned above.

Neural network prediction model for characteristics of welding pool.

The neural network (NN) method has been applied to the modeling of welding process for nearly 30 years [9, 15, 16]. The typical NN model is suitable for predicting the dynamic process characteristics of welding pool, for example, the prediction of the back pool size and penetration by NN model, which is very important in the closed-loop control of penetration during welding process. There are other welding seam forming, welding quality evaluation using NN model prediction and classification, etc.

Knowledge modeling of welding dynamic process.

One of the key intelligent technologies is to establish knowledge model from extracting welder manipulations so that the computer or robotic systems could play back human knowledge and intelligent decision-making function.

Because the differences of human describing himself experience capability and uncertainty in welding process, it is very difficult or almost impossible for one to

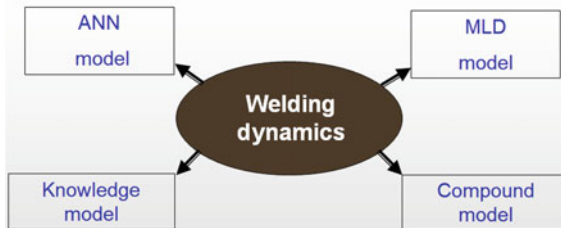


Fig. 10 HI features in intelligent modeling methodology for welding dynamic process

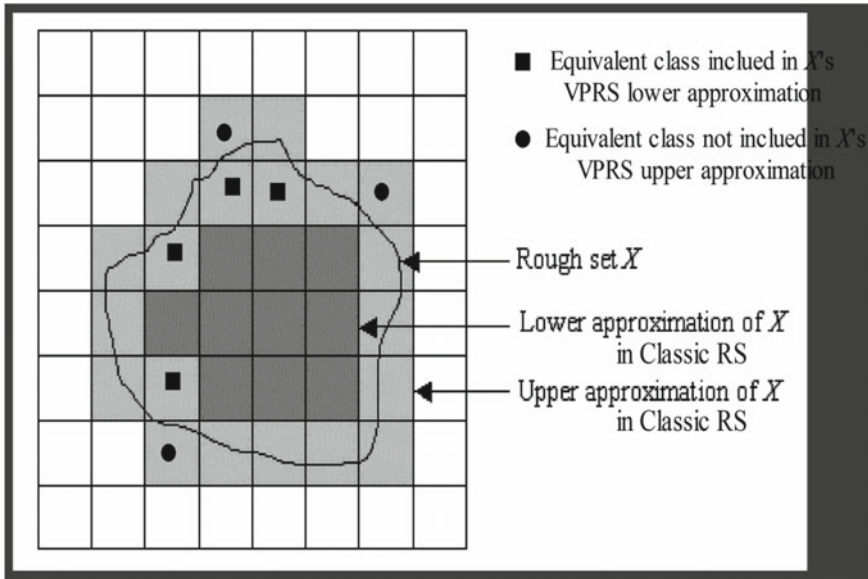


Fig. 11 Rough set (RS) theory for knowledge modeling methods for welding process

directly get enough expert knowledge from welder's experiences [41–47]. A feasible way is extracting knowledge from measured experimental data by fuzzy computing, rough set theory and other soft computing methods. A fuzzy rule model of weld pool dynamics in the pulsed GTAW process was developed by fuzzy identification algorithms in Refs. [42–45]. Knowledge modeling methods for welding process from collected data were investigated by the basic rough set (RS) theory as shown in Fig. 11.

Mixed Logical Dynamical (MLD) modeling of GTAW dynamics during robotic welding.

In the research direction of control theory in the last 20 years, a hot topic is the so-called mixed logical dynamical (MLD) modeling and control method for the complex system, which is useful to model and control the so-called hybrid systems with interacting physical laws, logical rules, continuous and discrete variables, and operating constraints. References [48–52] develop MLD modeling methodology for pulsed GTAW process in robotic welding systems and robotic welding process and systems, which shows the MLD method is highly suitable for welding dynamical process, particularly, automatic and robotic welding systems.

Figure 12 shows the weld pool with misalignment-mixed logical dynamical (WPM-MLD) model and the weld pool with gap-mixed logical dynamical (WPG-MLD) model for estimating the backside weld width [48–50].

And Fig. 13 shows mixed logical dynamical (MLD) modeling of GTAW dynamics during robotic welding, the welding robot movement process (WRMP)-MLD model

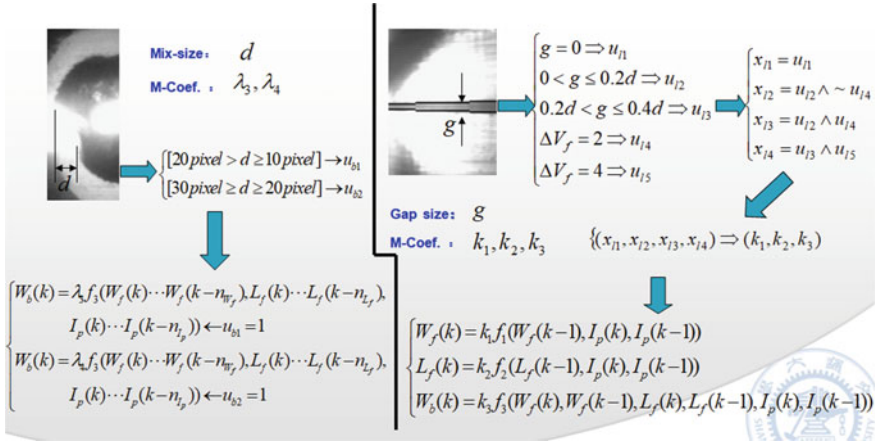


Fig. 12 WPM-MLD model and WPG-MLD model

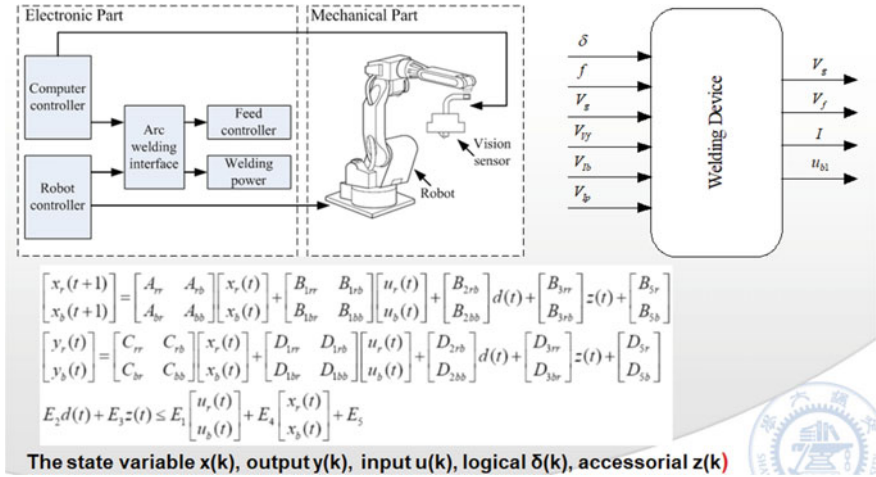


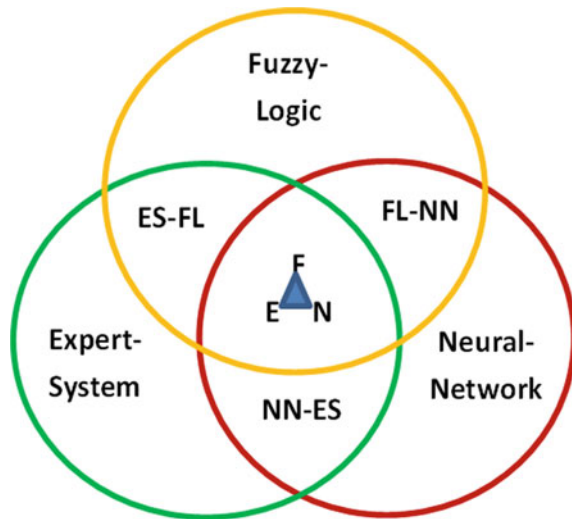
Fig. 13 WRMP-MLD model and WDOP-MLD model for robotic welding process and system

with 34 equations and the welding device operation (WDOP)-MLD model with 65 equations [48, 52].

HI modeling of expert systems, fuzzy logic and artificial neural networks.

The most common modeling methods, such as expert system (ES), fuzzy logic (FL) and neural network (NN), are the most common methods in the modeling of welding dynamic process. A single intelligent method or algorithm is represented in a monochromatic outer circle in Fig. 14.

Fig. 14 Interaction of FL-NN-ES intelligent modeling methods



In Refs. [10, 15, 16, 42–47], the knowledge model obtained by using FL, NN and ES modeling methods to the welding dynamic process is presented, respectively.

As shown in Fig. 14, there are two overlapping circles in the middle layer, such as the FL-NN, NN-ES and ES-FL, which represents a composite indication of two intelligent methods or algorithms.

The central part in Fig. 14 is the overlapping part of the three circles, i.e., N-F-E, which represents a composite representation of all three intelligent methods or algorithms.

Furthermore, the hybrid knowledge model of cross and combination of the FL, NN and ES methods for welding dynamic process is developed in Refs. [10, 16].

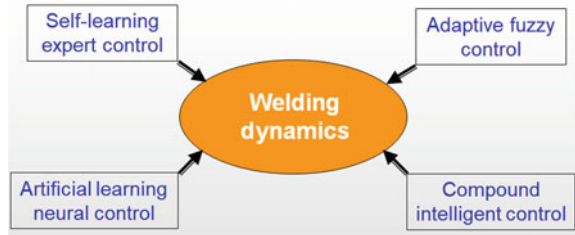
The interaction of these three intelligent modeling methods is shown in Fig. 14.

Other HI complexity of multi-interaction with intelligent modeling methods and algorithms can be further analyzed and investigated.

3.4 Hybrid Intelligence Features—Intelligent Control Methodology for Welding Dynamic Process

Intelligent control strategy is mainly aiming at complex uncertainty of welding process. Because of especial complexity in welding dynamical process, such as strong nonlinear and multivariable coupling, time-variety and uncertainty, it is specially suitable to adopt intelligent control strategy for welding process and systems [1, 6–10]. At present, various intelligent control methods, fuzzy logic, artificial neural networks, expert system and their combination control schemes [11–16, 55–61, 81–85], are shown in Fig. 15.

Fig. 15 Intelligent control methods in the welding process



According to different welding conditions, such as based on plate welding, butt welding, with filler, gap variety and uncertainty in welding process, many intelligent control methods, such as a self-learning expert control, fuzzy neural control, adaptive fuzzy neural control, compound intelligent controller with feed-forward compensating control methods for gap variety [59] and so on, have been developed for the penetration, the width of the upside and backside pool and seam, face reinforcement and fine forming of the weld seam during arc welding process.

The expert system for real-time control of welding process is an important part in intelligentized welding systems. Some advanced autonomous expert system for control of welding dynamical process should be still investigated for mode recognition of weld workpiece, environment and seam type, and autonomous programming robotic welding path and techniques, intelligent control of welding process in the IWMT [1, 10, 59, 85].

Because various intelligent methods and algorithms act on welding dynamic process and welding equipment system at the same time, for example, robot welding system, the special hybrid intelligent characteristics of welding process and system control are shown in Fig. 16.

The diagram shows the HI characteristics of various methods and algorithms of intelligent information extraction, such as the MSS, MSIF in the HIS, the HIM and IPM in the HIIIF for modeling, and control methods and algorithms, such as the KRC, ILC and ESC in the HIC of the dotted box.

In Fig. 17, the characteristics in hybrid intelligent control of robotic welding process and systems, the diagram shows the HI characteristics of various methods and algorithms for the HKT including ER, EK and AP; the HICT including AG, WT and MC; the HIT including MS, MIF and PM; and the HDIT including ICSM and NC, which are circled in the red dotted box in the diagram [1, 81–84, 86–98].

4 HI Features in Application on the IWMS/W/F

The previous section discusses the complex, mixed or hybrid intelligence characteristics that are shown in the combination of various intelligent methods used in IWM technology and methodology with the various AI algorithms.

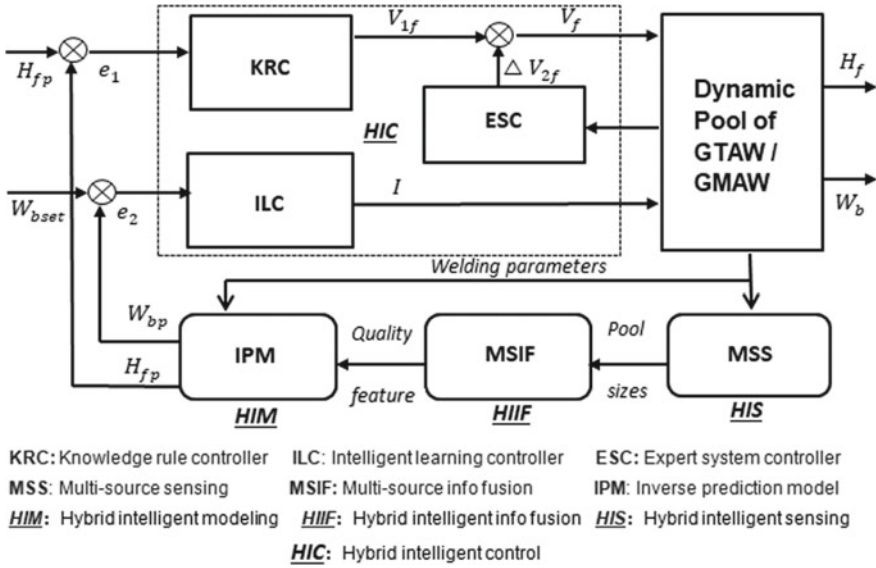


Fig. 16 HI features in intelligent control of arc welding process

The next section will discuss the hybrid intelligence features of multiple intelligent methods and AI algorithms shown in IWM engineering applications, such as the IWMS (systems)/W (workshop)/F (factory).

4.1 Hybrid Intelligence in IWMS/W/F by Internet of Things

With the application of the Internet of things technology in the industrial field, it has effectively promoted the innovation and development of intelligent manufacturing technology and system based on the Internet of things. We also propose an Internet of things-based IWMT/S in the welding field as shown in Fig. 18 for design and structure of IWM workshop and factory. The part of the red dashed frame in Fig. 18 includes a variety of intelligent welding methods based on the Internet of things technology and the system of AI algorithm in the application of in intelligentized welding manufacturing engineering (IWME), such as the hybrid intelligent methods and algorithms displayed in MES level and intelligent control level of the intelligentized welding manufacturing workshop by Internet of things (IWMWIT) in Fig. 18.

The optimal planning method and algorithm for welding product task, such as robotic welding path, attitude and welding process parameter planning, expert system of welding process, visual recognition method and algorithm for welding initial point; The autonomous guidance and tracking control method and algorithm in robotic

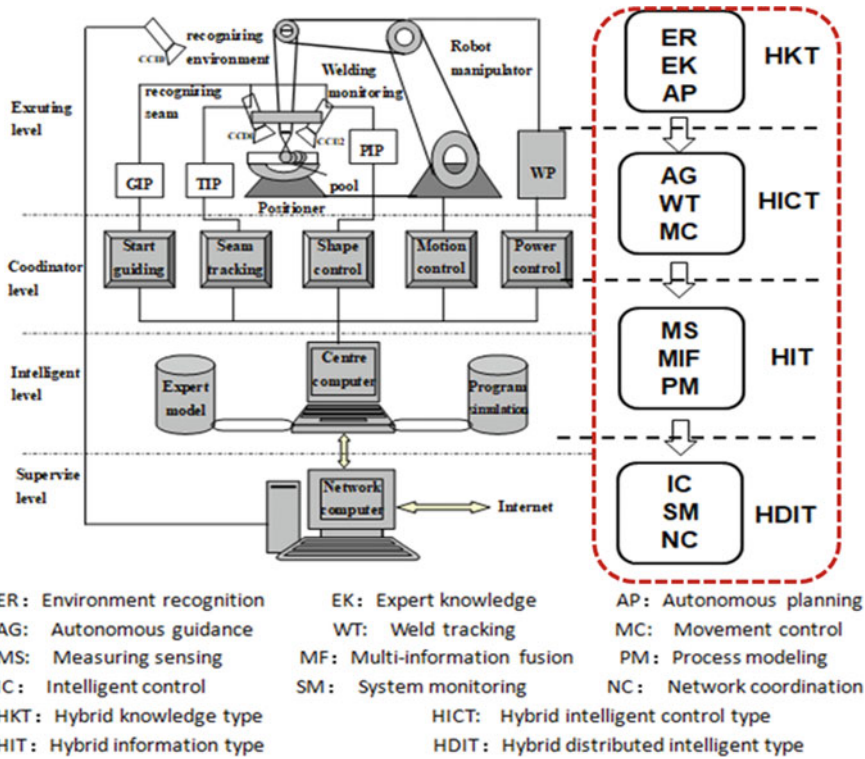


Fig. 17 HI features in intelligent control of robotic welding process and systems

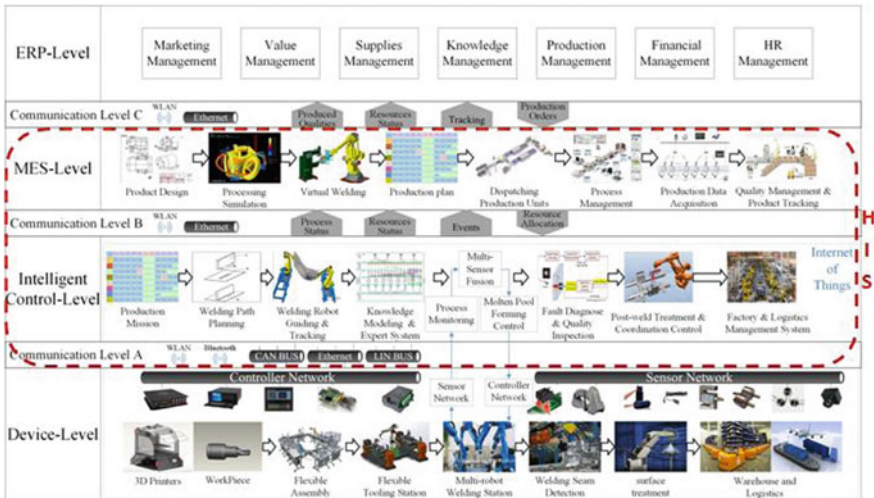


Fig. 18 HI features displayed in application of the IWM workshop by Internet of things

welding process, such as acquisition and processing of multi-source sensing information such as vision, arc, sound and spectrum in the process of welding, and the technology and algorithm of multi-source sensing information acquisition and processing in the process of welding; The Data driven expert system for monitoring of welding process; The knowledge model and penetration prediction model; The intelligent control method and algorithm of weld pool penetration and weld forming, prediction algorithm of welding quality; The fault diagnosis of welding process and system; The communication and coordination control of welding production line and workshop equipment, and the intelligent management of the whole process of welding product manufacturing, all of which highlight the complexity of hybrid intelligent technology features in the IWMWIT, are shown as the red dashed frame HIS in Fig. 18.

4.2 A Multi-agent Hybrid Intelligence Structure for IWMS

A hierarchical MAS coordinated control structure of intelligentized welding manufacturing system (IWMS) is proposed in this paper. The IWMS is designed as so-called a multi-robot device follower and a network virtual leader for the IWMS [99, 100]. It is a hierarchical multi-agent system; i.e., the IWMS is divided into “leader MAS” and “follower MAS” and “bottom follower MAS” structure with multi-intelligent cooperative operation. It implements the “total goal coordination” and “sub-task coordination” two-level MAS coordination mechanism of the IWMS. The “leader MAS” in the first layer of the IWMS completes the “goal coordination” (LMAS-0) of multiple MAS. The first layer of multiple “follower MAS” (FMAS-1i) is the control of sub-task coordination (LMAS-2i), which is the leader of the second layer of multiple MAS. The sub-task coordination (MAS-2i) of multiple MAS leaders in the second layer is directly controlled by root task coordination of multiple agent (F-agent-3-ij) execution units. This paper proposes the “leadership-follow” mechanism for the MAS hierarchical network coordination control structure diagram shown in Fig. 19, which contains the complex HIS characteristics of multi-agents and IWMT/S.

For the design and implementation of hybrid intelligent system of MAS and IWMT/S, this paper presents a structure diagram of a hybrid intelligent system of welding manufacturing (HISWM) shown in Fig. 20, which contains the different classifications of MAS and various intelligent methods and algorithms.

4.3 An Intelligentized Welding Manufacturing Workshop for Offshore Drilling Platform

As one of the application practices of the IWMT, our research team and Shanghai ZMPC have developed a kind of intelligentized welding manufacturing workshop

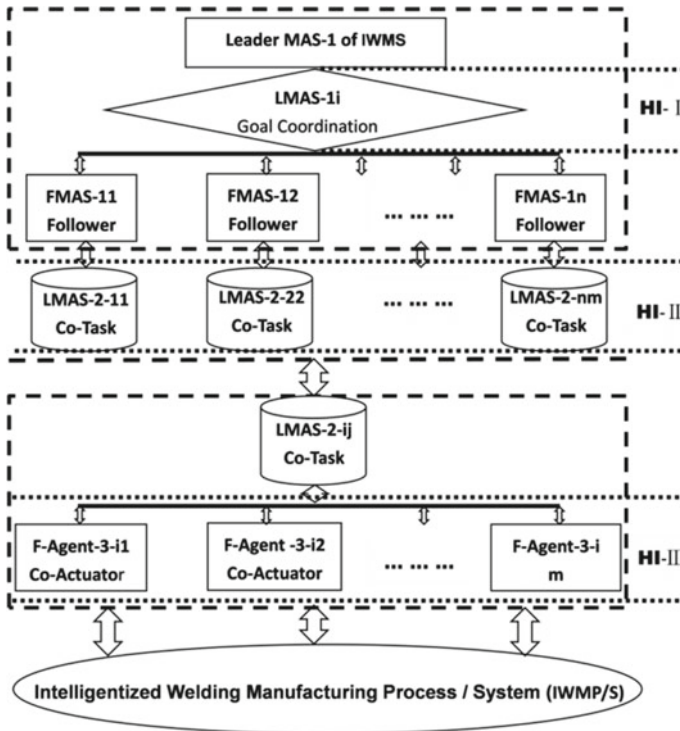


Fig. 19 Leader–follower MA—HI structure of the IWMP/S

(IWMW) for the pile legs of the offshore drilling platform as shown in Fig. 21. In this IWMW, the IWMS technology has been successfully applied to the construction of the IWMW for supporting the pile legs of the offshore drilling platform. The intelligent welding technology, production system and product quality and benefit of offshore drilling platform are greatly improved.

The IWMW for piles and legs of the offshore platform reflects the pentabasic structure function of the IWMT proposed in this paper, as shown in Fig. 22. On the basis of the general intelligent manufacturing system, it shows the key technology in the robotic welding flexible system, as well as the information, digitalization, networking and intelligentized manufacturing technologies in Fig. 22, combined with the welding process requirement of the pile leg of the offshore platform, the IWMW for piles and legs of the offshore platform is integrated and implemented.

Furthermore, the intelligent pentabasic technology, systems and methodology of the IWMW for the pile legs of the offshore drilling platform and the hybrid intelligent function of the IWMW can be analyzed accordingly, as shown in Fig. 23.

It shows the hybrid pentabasic intelligent function of IWMW for the pile legs of the drilling platform, which can be divided into the single intelligent tech./syst. in outer layer, such as IT/IS, DT/VS, WT/MS, RT/FS and NT/DS; the triple intelligent

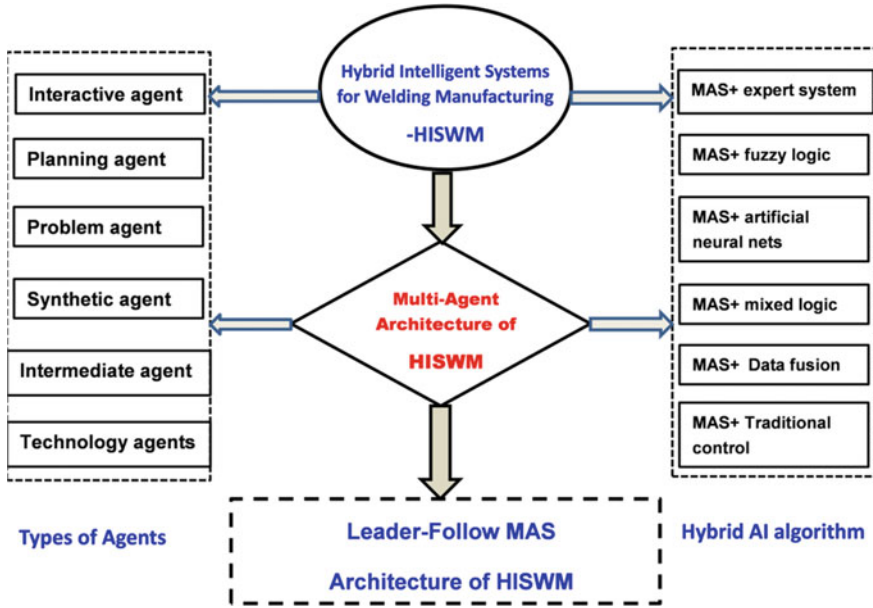


Fig. 20 A hybrid intelligent system of welding manufacturing (HISWM)

recombination in the middle layer, such as I/D/R, D/W/N, W/R/I, R/N/D and N/I/W tech./syst.; and the quintuple or hybrid intelligence phenomena I/W/D/R/N tech./syst. in the core, as shown in Fig. 23. Further, hybrid intelligence features are related to different AI methods and algorithms used in practice.

5 Concluding Remarks

This paper presents some hybrid intelligence problems and the HI features in IWMT/S/W/F. Based on the technological constitution of the IWMT/S, the paper investigates the hybrid or compound, multiple and mixed effects of different intelligent methods and technologies applied in IWMT/S, which includes the hybrid intelligence problems existing in multi-information sensing, knowledge modeling of arc welding process and intelligent control methodology for welding dynamic process, and the hybrid intelligence problems existing in intelligentized technologies for robotic welding process and systems. The HI problems in the IWMT/S are also an unavoidable bottleneck and challenge in the theory and application of hybrid intelligent algorithms and techniques. Therefore, this paper put forward the HIS problems in the IWM process and systems in order to attract scientists and engineers' enough attention on that.

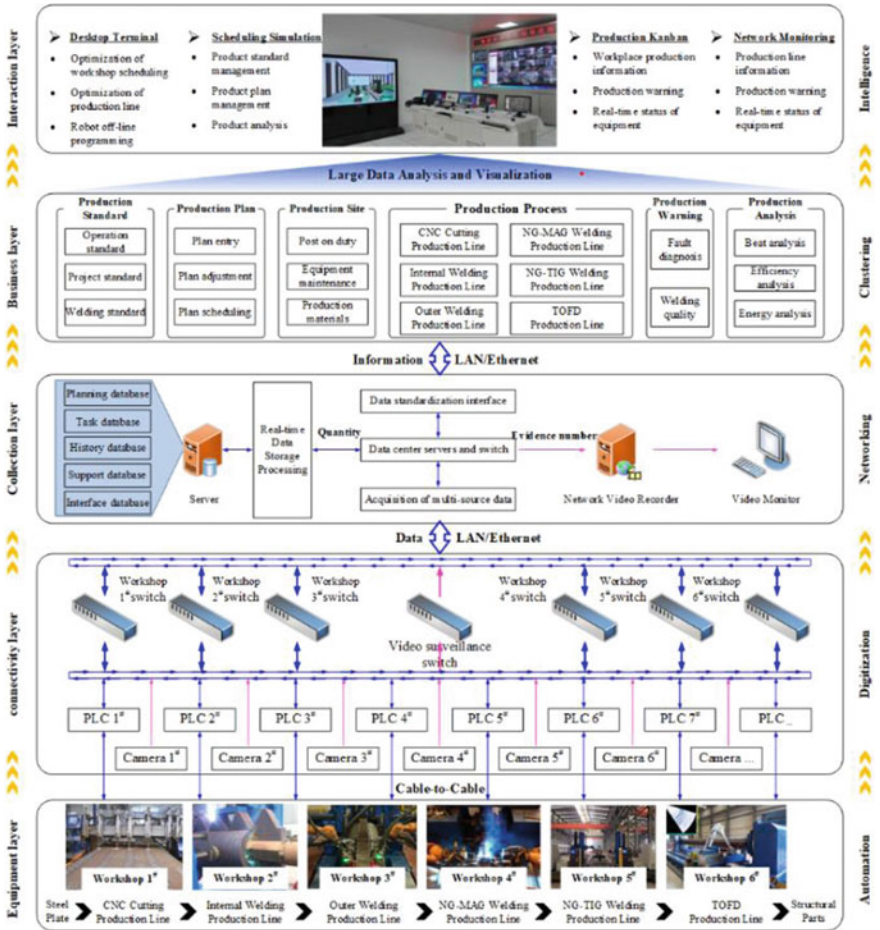


Fig. 21 A realization of the IWMW for the pile legs of the offshore drilling platform

The author hopes to further explore the optimization methods of hybrid or composite intelligent algorithms of IWMT/S by putting forward the problems of the HI methods and techniques existing in IWMT/S, and the optimization design of the HIS of the IWMS and IWME.

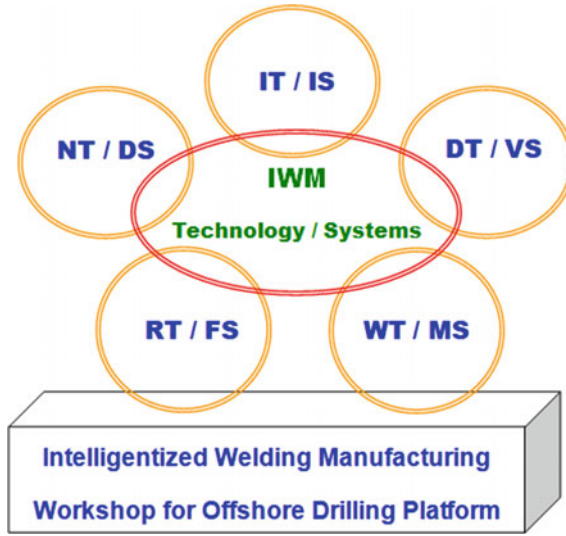


Fig. 22 Pentabasic function of the IWMW for piles and legs of the offshore platform

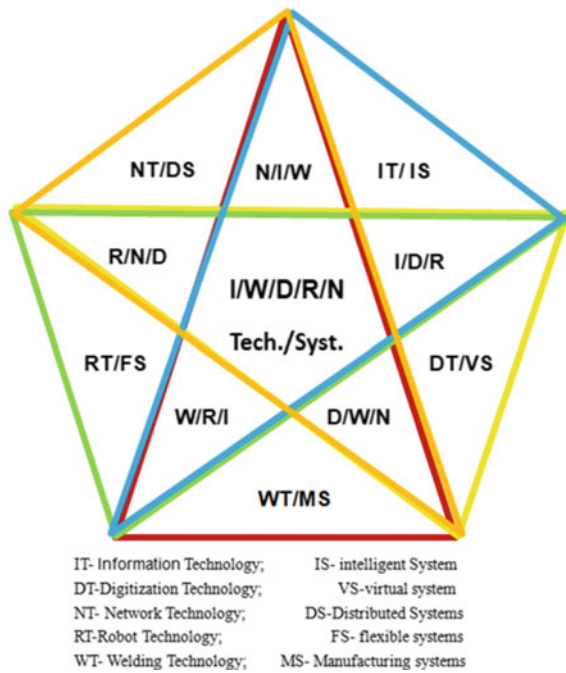


Fig. 23 Hybrid intelligent function of the IWMW for the offshore drilling platform

Acknowledgements This work was supported by National Natural Science Foundation of China, No. 61873164, 51575349 and 61374071. The author thanks all his Ph.D. students for their contributions to this paper.

References

1. Chen SB (2015) On intelligentized welding manufacturing. In: 2014 International conference on robotic welding, intelligence and automation (RWIA'2014), vol 363. Springer, Berlin, pp 3–34
2. Paul D, Starke G (1994) Welding in the century of information technology. *Weld World* 34:1–20
3. Dilthey U, Stein L (1992) Robot system for arc welding—current position and future trends. *Weld Cutting* 8:150–152
4. Pan JL (1999) A survey of welding sciences in 21th century. In: Proceeding of 9th Chinese welding conference, Tianjin, China, vol 1, pp 1–17
5. Trailer (1995) Manufacturer depends on robotic welding to boost production. *Weld J* 74(7):49–51
6. Chen SB, Qiu T, Tao LT et al (2003) On intelligentized technologies for modern welding manufacturing. *Chin J Mech Eng* 16(4):367–370
7. Chen SB, Lin T, Chen WJ et al (2004) Concepts and technologies on intelligentized welding manufacturing engineering. *Trans China Weld Inst* 25(6):124–128
8. Chen SB (2011) Research evolution on intelligentized technologies for robotic welding at SJTU. In: Robotic welding. Lecture notes in electrical engineering LNEE, vol 88, pp 3–14
9. Chen SB, Lv N (2014) Research evolution on intelligentized technologies for arc welding process. *J Manuf Process* 16(1):109–122
10. Chen SB, Wu J (2008) Intelligentized technology for arc welding dynamic process. In: Lecture notes in electrical engineering LNEE, vol 29. Springer, Berlin
11. Tarn TJ, Chen SB, Chen XQ (2015) The advances in intelligent systems and computing. In: Robotic welding, intelligence and automation. Springer, Berlin
12. Tarn TJ, Chen SB, Fang G (2011) Lecture notes in electrical engineering. In: Robotic welding, intelligence and automation. LNEE, vol 88. Springer, Berlin
13. Tarn TJ, Chen SB, Zhou CJ (2007) Robotic welding, intelligence and automation. Lecture notes in control and information sciences LNCIS, vol 362. Springer, Berlin
14. Tarn TJ, Chen SB, Zhou CJ (2004) Robotic welding, intelligence and automation. Lecture notes in control and information sciences LNCIS, vol 299. Springer, Berlin
15. Chen SB, Lou YJ, Wu L et al (2000) Intelligent methodology for measuring, modeling, control of dynamic process during pulsed GTAW—Part I bead-on-plate welding. *Weld J* 79:151–163
16. Chen SB, Zhao DB, Wu L et al (2000) Intelligent methodology for measuring, modeling, control of dynamic process during pulsed GTAW—Part II butt welding. *Weld J* 79:164–174
17. Masumoto L, Araya T, Iochi A, Normura H (1983) Development and application of sensors and sensor system for arc welding. *J Japan Weld Soc* 52:39–47
18. Carlson NM, Johnson JA (1988) Ultrasonic sensing of weld pool penetration. *Weld J* 67:239–246
19. Zhang YM, Kovacevic R, Li L (1996) Characterization and real-time measurement of geometrical appearance of weld pool. *Int J Mach Tool Manuf* 36(7):799–816
20. Chen Z, Chen J, Feng Z (2017) Monitoring weld pool surface and penetration using reversed electrode images. *Weld J* 96:367–375
21. Wang JJ, Lin T, Chen SB (2005) Obtaining of weld pool vision information during aluminum alloy TIG welding. *Int J Adv Manuf Tech* 26:219–227

22. Lp Li, Chen SB, Lin T (2005) The modeling of welding pool surface reflectance of aluminum alloy pulse GTAW. *Mater Sci Eng A* 394:320–326
23. Chen SB (2007) Visual information acquirement and real-time control methodologies for weld pool dynamics during pulsed GTAW. *J Mater Sci Forum* 539–543
24. Cj F, Fl Lv, Chen SB (2009) Visual sensing and penetration control in aluminum alloy pulsed GTAW. *Int J Adv Manuf Technol* 42:126–137
25. Chen Z, Chen J, Feng Z (2018) Welding penetration prediction with passive vision system. *J Manuf Process* 36:224–230
26. Chen B, Wang JF, Chen SB (2010) A study on applications of multi-sensor fusion in pulsed GTAW. *Ind Robot Int J* 37(2):168–176
27. Chen B, Wang JF, Chen SB (2010) Prediction of pulsed GTAW penetration status based on BP neural network and D-S evidence theory information fusion. *Int J Adv Manuf Technol* 48(1–4):83–94
28. Chen B, Chen SB (2010) Multi-sensor information fusion in pulsed GTAW based on fuzzy measure and fuzzy integral. *Assembly Autom* 30(3):276–285
29. Itti L, Koch C, Niebur E (1998) A model of saliency-based visual attention for rapid scene analysis. *Pattern Anal Mach Intell* 20(11):1254–1259
30. Zhang Y, Lv N, Huang YM et al (2014) Feature characters extraction with visual attention method based on three-path vision sensing of Al alloy GTAW welding. *Trans China Weld Inst* 35(6):53–56
31. Cudina M, Prezelj J, Polajnar I (2008) Use of audible sound for on-line monitoring of gas metal arc welding process. *Metalurgija* 47(2):81–85
32. Wang JF, Lv FL, Chen SB (2009) Analysis of arc sound characteristics for gas tungsten argon welding. *Sens Rev* 29(3):240–249
33. Ye Z, Chen SB et al (2011) Feature selection of arc acoustic signals used for penetration monitoring. In: *Robotic welding, intelligence and automation. Lecture notes in electrical engineering LNEE*, vol 88, pp 203–210
34. Lv N, Xu YL et al (2013) Research on detection of welding penetration state during robotic GTAW process based on audible arc sound. *Ind Robot Int J* 40(5):474–493
35. Lv N, Xu YL et al (2013) Audio sensing and modeling of arc dynamic characteristic during pulsed Al alloy GTAW process. *Sens Rev* 33(2):141–156
36. Mirapeix J, Cobo A, Fernandez S et al (2008) Spectroscopic analysis of the plasma continuum radiation for on-line arc-welding defect detection. *J Phys D Appl Phys* 41(13):1–8
37. Yu HW, Chen SB et al (2013) Arc spectral processing technique with its application to wire feed monitoring in Al-Mg alloy pulsed gas tungsten arc welding. *J Mater Process Technol* 213(5):707–716
38. Yu HW, Chen HB et al (2013) Spectroscopic diagnostics of pulsed gas tungsten arc welding plasma and its effect on weld formation of Al-Mg alloy. *Spectrosc Lett* 46(5):350–363
39. Yu HW, Chen HB et al (2013) Application of arc plasma spectral information in the monitor of Al-Mg alloy pulsed GTAW penetration status based on fuzzy logic system. *Int J Adv Manuf Technol* 68(9–12):2713–2727
40. Zhang ZF, Yu HW, Chen HB et al (2013) Real-time defect detection in pulsed GTAW of Al alloys through on-line spectroscopy. *J Mater Process Technol* 213(7):1146–2115
41. Kovacevic R, Zhang YM (1997) Neuro-fuzzy model-based weld fusion state estimation. *IEEE Trans Control Syst Technol* 5(4):30–42
42. Wang B, Chen SB, Wang JJ (2005) Rough set based knowledge modeling for the aluminum alloy pulsed GTAW process. *Int J Adv Manuf Technol* 25(9–10):902–908
43. Wang WY, Chen HB et al (2013) Rough set-based model for penetration control of GTAW. In: *Robotic welding, intelligence and automation. Lecture notes in electrical engineering LNEE*, vol 88, pp 211–218
44. Li WH, Chen SB, Lin T (2007) Discretization in rough set modeling method for welding process. In: *Robotic welding, intelligence and automation. Lecture notes in control and information sciences LNCIS*, vol 362, pp 325–332

45. Li WH, Chen SB, Wang B (2008) A variable precision rough set based modeling method for pulsed GTAW. *Int J Adv Manuf Technol* 36(11–12):1072–1079
46. Huang XX, Chen SB (2006) SVM-based fuzzy modeling for the arc welding process. *Mater Sci Eng A* 427(1–2):181–187
47. Huang XX, Shi FH, Chen SB (2009) SVM-based fuzzy rules acquisition system for pulsed GTAW process. *Eng Appl Artif Intell* 22(8):1245–1255
48. Ma HB (2010) Research on mixed logical dynamical modeling method of robotic Al alloy pulsed TIG welding process based in vision sensing. Dissertation, Shanghai Jiao Tong University
49. Ma H, Wei S, Li L et al (2011) Mixed logical dynamical model of the pulsed gas tungsten arc welding process with varied gap. *Proc Inst Mech Eng Part I J Syst Control Eng* 225(3):270–280
50. Ma HB, Wei SC, Lin T et al (2010) Mixed logical dynamical model for back bead width prediction of pulsed GTAW process with misalignment. *J Mater Process Technol* 210(14):2036–2044
51. Ma HB, Chen SB (2011) Study on the MLD modeling method of pulsed GTAW process for varied welding speed. In: *Robotic welding, intelligence and automation. Lecture notes in electrical engineering*, vol 88, pp 271–278
52. Ma HB, Chen SB (2011) Mixed logical dynamical model for robotic welding system. In: *Robotic welding, intelligence and automation. Lecture notes in electrical engineering LNEE*, vol 88, pp 23–128
53. Sarailoo M, Rezaie B, Rahmani Z (2012) MLD model of boiler-turbine system based on PWA linearization approach. *Int J Control Sci Eng* 2(4):88–92
54. Yin YJ, Hosoe S, Luo ZW (2007) A mixed logic dynamical modeling formulation and optimal control of intelligent robots. *Optim Eng* 8(3):321–340
55. George E (1995) Weld modeling and control using artificial neural networks. *IEEE Trans Ind Appl* 31:1484–1491
56. Zhang YM, Kovacevic R, Li L (1996) Adaptive control of full penetration GTA welding. *IEEE Trans Control Syst Technol* 4(4):394–403
57. Chen SB, Wu L, Wang QL (1997) Self-learning fuzzy neural networks for control of uncertain systems with time delays. *IEEE Trans* 27:142–148
58. Zhao DB, Chen SB, Wu L et al (2001) Intelligent control for the double-sided shape of the weld pool in pulsed GTAW with wire filler. *Weld J* 80:253–260
59. Zhang GJ, Chen SB, Wu L et al (2005) Intelligent control of pulsed GTAW with filler metal. *Weld J* 80(1):9–16
60. Fan CJ (2008) Weld pool characters extraction and intelligent control during varied gap Al alloy pulsed GTAW process. Dissertation, Shanghai Jiao Tong University
61. Chen SB, Wu J, Du QY (2011) Non-linear modelling and compound intelligent control of pulsed gas tungsten arc welding dynamics. *Proc Inst Mech Eng Part I J Syst Control Eng* 225(11):113–124
62. Medsker L (1995) *Hybrid intelligent systems*. Kluwer, Boston
63. Yang SZ, Ding H (1992) Development and research of intelligent manufacturing technology and intelligent manufacturing Systems. *China Mech Eng* 3(2)
64. Wang G, Huang LH, Zhang CH (2010) A survey of hybrid intelligent systems. *J Syst Eng* (4)
65. Minsky M (1991) Logic versus analogical or symbolic versus connection is to neat versus scruffy. *AI Mag* 12(2):35–51
66. Abraham A, Nath B (2002) *Hybrid intelligent systems design: a review of a decade of research*. Technical Report, Monash University, Melbourne
67. Negoita MG, Neagu D, Palade V (2005) Computational intelligence. *Studies in fuzziness and soft computing*, vol 174. Springer, Berlin
68. Ovaska SJ (2005) *Computationally intelligent hybrid systems: the fusion of soft computing and hard computing*. Wiley, New York
69. Medsker LR, Bailey DL (1992) Models and guidelines for integrating expert systems and neural net works. In: *Proceeding of hybrid architecture for intelligent systems*. CRC Press, Florida pp 153–171

70. Goonatilake S, Khebbal S (1995) Intelligent hybrid systems. Wiley, New York
71. Ovaska SJ, Van Landingham HF (2002) Fusion of soft computing and hard computing in industrial applications: an overview. *IEEE Trans. Syst Man Cybern Part C* 32(2):72–79
72. Khosla R, Dillon T (1997) Engineering intelligent hybrid multi-agent systems. Kluwer, Boston
73. Lertpalangsunt IN, Chan CW (2000) An architectural framework for hybrid intelligent systems: implementation issues. *Intell Data Anal* 4(3, 4):375–393
74. Jacobsen HA (1998) A generic architecture for hybrid intelligent systems. In: *Proceeding of IEEE international conference on fuzzy systems*. Springer, Berlin, pp 709–714
75. Zhang ZL, Zhang C (2004) Agent-based hybrid intelligent systems, vol 3. Springer, Berlin
76. Li CS, Liu L, Mahi S (2005) An agent-oriented methodology for constructing dynamic platform-based HIS. In: *Proceeding of the 18th Australian joint conference on artificial intelligence*. Springer, Berlin, pp 705–714
77. Hefny HA, Wahab A, Bahnasawi A (1999) A novel framework for hybrid intelligent systems. In: *Proceeding of the 12th international conference on industrial and engineering applications of artificial intelligence and expert systems*. Springer, Berlin, pp 761–770
78. Kordon AK (2004) Hybrid intelligent systems for industrial data analysis. *Int J Intell Syst* 19(4):367–383
79. Grossmann RL, Nerode A, Ravn AP et al (1993) Hybrid systems. *Lecture notes in computer science*, vol 736. Springer, New York
80. Antsaklis PJ (2000) Special issue on hybrid systems: theory and applications a brief introduction to the theory and applications of hybrid systems. *Proc IEEE* 88(7):879–887
81. Chen SB, Wang WY, Ma HB (2010) Intelligent control of arc welding dynamics during robotic welding process. The invited paper of the THERMEC'2009. *J Mater Sci Forum* 638–642
82. Chen HB, Lv FL, Lin T, Chen SB (2009) Closed-loop control of robotic arc welding system with full-penetration monitoring. *J Intell Rob Syst* 56:565–578
83. Shen HY, Ma HB, Lin T, Chen SB (2007) Research on weld pool control of welding robot with computer vision. *Ind Robot* 34(6):467–475
84. Kong M, Chen SB (2008) Al alloy weld pool control of welding robot with passive vision. *Sens Rev* 29(1):28–37
85. Chen SB, Zhang YM, Feng ZL (2018) *Transactions on intelligent welding manufacturing*, vol 2. Springer, Berlin, pp 1–4
86. Chen SB (2007) On the key intelligentized technologies of welding robot. In: *Lecture notes in control and information sciences LNCIS*, vol 362, pp 105–116
87. Chen XZ, Chen SB (2010) The autonomous detection and guiding of start welding position for arc welding robot. *Ind Robot Int J* 37(1):70–78
88. Ye Z, Fang G, Chen SB (2013) A robust algorithm for weld seam extraction based on prior knowledge of weld seam. *Sens Rev* 33(2):125–133
89. Zhou L, Lin T, Chen SB (2006) Autonomous acquisition of seam coordinates for arc welding robot based on visual servoing. *J Intell Rob Syst* 47(3):239–255
90. Shen HY, Wu J, Lin T, Chen SB (2008) Arc welding robot system with seam tracking and weld pool control based on passive vision. *Int J Adv Manuf Technol* 39(7–8):669–678
91. Shen HY, Lin T, Chen SB (2010) Real-time seam tracking technology of welding robot with visual sensing. *J Intell Rob Syst* 59:283–298
92. Chen SB, Chen XZ, Li JQ, Lin T (2005) Acquisition of welding seam space position information for arc welding robot based on vision. *J Intell Rob Syst* 43(1):77–97
93. Wei SC, Kong M, Lin T, Chen SB (2011) Three-dimensional weld seam tracking for robotic welding by composite sensing technology. *Ind Robot Int J* 38(5):500–508
94. Xu YL, Lv N, Chen SB et al (2012) Research on the real-time tracking information of three-dimension welding seam in robotic GTAW process based on composite sensor technology. *J Intell Rob Syst* 68(2):89–103
95. Zhang T, Chen SB, Wu MH (2013) Optimal motion planning of all position autonomous mobile welding robot system for fillet seams. *IEEE Trans Autom Sci Eng* 10(4):1147–1151
96. Piao YJ, Lin T, Qiu T, Chen SB (2002) Application of multi-agent systems in welding flexible manufacturing system. *Trans China Weld Inst* 23(5):87–90

97. Piao YJ, Zhu ZY, Chen SB (2004) Multi-agent collaboration control for multi-manipulator WFMS. *J Syst Simul* 16(11):2571–2574
98. Yang CD, Chen SB (2011) Survey on modeling and controlling of welding robot systems based on multi-agent. In: *Robotic welding, intelligence and automation. Lecture notes in electrical engineering LNEE*, vol 88, pp 107–113
99. Su H, Wang X, Lin Z (2009) Flocking of multi-agents with a virtual leader. *IEEE Trans Autom Control* 54(2):293–307
100. Cheng L, Hou ZG, Tan M, Lin Y, Zhang W (2010) Neural-network-based adaptive leader-following control for multiagent systems with uncertainties. *IEEE Trans Neural Networks* 21(8):1351–1358

Research Papers

Double-Electrode Micro-plasma Arc Welding Curved Surface Part Additive Manufacturing Control System



Ding Fan, Nan Li, Jiankang Huang, Shurong Yu, and Wen Yuan

Abstract With the xPC target real-time environment, double-electrode micro-plasma arc welding additive manufacturing control system is set up. And UG/NX software system is used to make parts integrative and automatically from modeling, tool path planning as well as simulating to execution code generation. Furthermore, the elliptical and cylindrical curved surfaced parts are deposited with 304L stainless steel material by changing the bypass welding current value in this system. Also, the ring parts are well produced by using this double-electrode micro-plasma arc welding rapid prototyping system with milling method together.

Keywords Double-electrode micro-plasma arc welding · Additive manufacturing · UG/NX · Tool path planning · Arc tool library · Curved surface part

1 Introduction

Wire and arc additive manufacturing (WAAM) plays a decisive role in military industry, aerospace, automotive and other manufacturing and processing fields due to its advantages of saving raw materials, shortening the processing cycle, having high-density parts and high forming efficiency compared with the traditional manufacturing methods by using molds, flasks and tools when forming large and complex parts [1]. WAAM mainly uses the arcs of gas metal arc welding (GMAW), gas tungsten arc welding (GTAW) and plasma arc welding (PAW) as welding heat sources

D. Fan (✉) · N. Li · J. Huang · W. Yuan
School of Materials Science and Engineering, Lanzhou University of Technology, Lanzhou 730050, China
e-mail: fand@lut.edu.cn

S. Yu
School of Mechanical and Electrical Engineering, Lanzhou University of Technology, Lanzhou 730050, China

D. Fan · J. Huang · S. Yu
State Key Laboratory of Advanced Processing and Recycling of Non-ferrous Metals, Lanzhou University of Technology, Lanzhou 730050, China

with the digital control technology to build 3D metal object parts layer by layer [2]. But in the rapid prototyping of WAAM, continuous and consistent layer-by-layer surfacing requires the automation of the stacking process, the rationalization of the stack deposition path and the good repeatability of each layer's composition, size, organization and performance, especially for the parts with curved shapes. Therefore, the WAAM rapid prototyping system has become the key to stacking complex functionally graded parts as well as a hotspot and a difficult point in the research of universities and enterprises at home and abroad due to its high degree of automation, controllable heat during the stacking process and accurate forming quality and size [3].

Spencer et al. [4] used additive manufacturing technology controlled by Siemens RCM CNC robot system based on GMAW to perform several stacking experiments. They studied the problem of high surface roughness and deterioration of the structure caused by excessive heat input during the stack forming process with the help of infrared thermal sensing technology. Based on GTAW, Professor Li et al. [5] established an additive manufacturing forming system and studied the collapse of two sides of the formed part due to heat accumulation during the stack forming process.

However, Professor Lu et al. [6] proposed a new method called bypass-coupled double-electrode arc welding (DE-AW), which adds a PAW or GTAW torch in the arc between the welding wire and the workpiece to form a bypass arc to shunt the current flowing into the base material. This method not only effectively controls the heat input of the base material on the basis of ensuring a high deposition rate, but also lays a foundation for easy automatic control. Further, under the xPC target real-time environment, the research group established a real-time target software and hardware platform for double-electrode arc welding by using rapid prototyping technology. Experimental research on welding processes under different controllers was carried out, and stable welding and well beam formation were achieved [7].

In addition, UG/NX as an interactive CAD/CAM system produced by Siemens PLM Software is powerful enough to implement the construction of complex entities and shapes, tool path design and digital machine simulation. As a result, it is widely used in automotive, aerospace, heavy equipment manufacturing and processing fields [8–10].

Therefore, the purpose of this article is to set up a bypass-coupled double-electrode micro-plasma arc welding (DE-MPAW) additive manufacturing control system based on the principle of bypass-coupled arc welding and the characteristics of small arc shape, large energy density and small heat-affected zone of micro-plasma arc welding (MPAW) to manufacture the 304L stainless steel material oval cylindrical parts and ring parts with the target real-time environment.

2 DE-MPAW Additive Manufacturing Control System

2.1 System Composition

DE-MPAW additive manufacturing control system is mainly composed of LHM-50 precision micro-plasma arc welder, WF-007A multifunctional automatic argon arc welding wire filler, AMR-300 rheostat, industrial control machine, PCL-812PG data acquisition card, PCL-728 analog output card, MIK-DZV-250 voltage transmitter, TKC100BR series Hall sensor, CP-80 high-speed photography and $X-Y-Z$ three-dimensional motion platform which is controlled by computer.

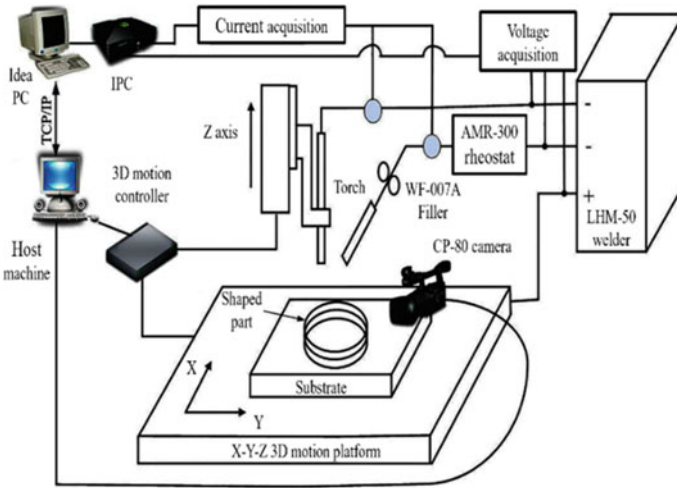
The hardware connection system is shown in Fig. 1. The LHM-30 micro-plasma welding torch and the wire feeding gun were fixed at a certain angle to the Z -axis of the 3D motion platform, while the base plate was fixed to the $X-Y$ -axis platform. The stacking and forming of the complex-shaped parts were completed by the movement of the $X-Y-Z$ 3D motion platform which was controlled by host machine. The forming process was based on DC direct connection, and the welding wire was in series with the AMR-300 adjustable rheostat to form a bypass of the welding circuit to divert the base material. Under the xPC target real-time environment of the MATLAB/Simulink toolbox, the collection of current and voltage were performed by the cooperation between the host and the target computers which were interconnected via the TCP/IP network communication protocol. Based on the collected current and voltage signals, AMR-300 rheostat was adjusted to control the heat of the base material. Meanwhile, CP-80 high-speed photography was connected to the host computer to catch the real-time information of the molten pool and arc shape during the forming process and monitor the entire stacking process.

2.2 Setting Up Arc Tool Library

UG/NX takes the processing basic module as the framework, connects all processing modules and provides users with a user-friendly graphical window environment, enabling it to complete all steps from the construction of three-dimensional models of complex solid parts to the design of processing programs in a graphical manner.

The premise of designing and planning of the deposition path in DE-MPAW additive manufacturing control system is the UG/NX platform. The forming experiment under different welding parameters should rely on the characteristics of layer-by-layer stack forming of the DE-MPAW additive manufacturing as well as the characteristics of the arc and weld beam morphology, so as to establish the DE-MPAW additive manufacturing system arc tool information database.

According to the welding parameters in Table 1 and the arc size captured by high-speed photography, the created DE-MPAW arc tool information is shown in Fig. 2. Figure 2a shows the arc tool information collected through experiments, and 1 represents the blade length, which is the distance between the micro-plasma arc



(a) hardware system diagram

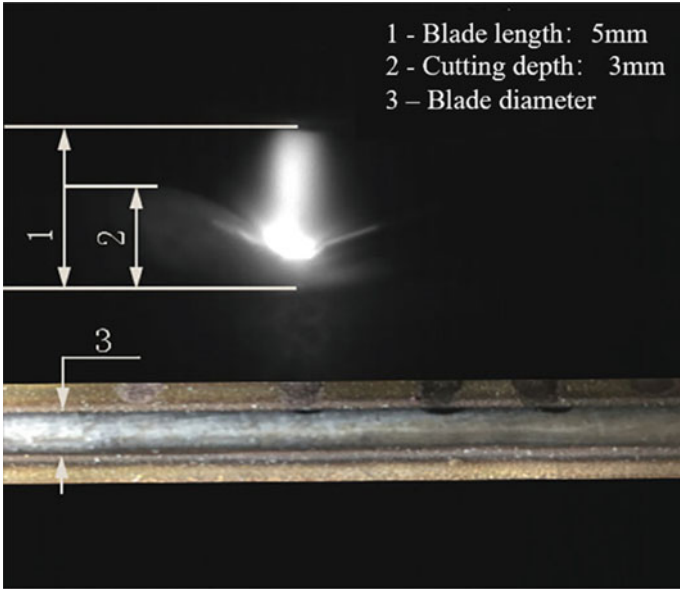


(b) physical composition of hardware

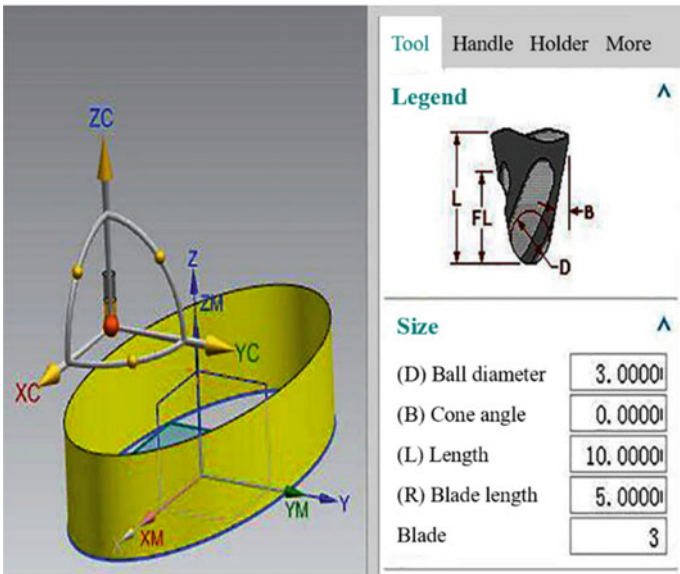
Fig. 1 DE-MPAW system

Table 1 Welding parameters in deposition process

| Parameters | Current (A) | Weld speed (m/min) | Feed speed (m/min) | Plasma gas (l/min) | Shielding gas (l/min) |
|------------|-------------|--------------------|--------------------|--------------------|-----------------------|
| Value | 50 | 0.08 | 1.2 | 1.0 | 10.0 |



(a) arc tool information collection



(b) creation of UG/NX arc tool information

Fig. 2 Arc tool parameters in DE-MPAW system

welding torch nozzle and the workpiece, here 5 mm; 2 represents the cutting depth of the blade, which is the height of the weld metal on the solidified side of the molten pool when stable welding process, here 3 mm; 3 represents the diameter of the blade, which is the width of the beam after welding, here 3 mm. Figure 2b shows the process of establishing arc tool model in the processing module of UG/NX with the arc tool information collected in Fig. 2a and the process of being added into the tool library. The tool model here is a ball and cylinder model, and the parameters blade length, blade and ball diameter, respectively, corresponded to the blade length, blade cutting depth and blade diameter information collected in Fig. 2a.

2.3 Curved Surface Part Modeling and Tool Path Planning

The curved surface part modeling and tool path planning were developed based on the UG/NX and the control together with the execution hardware facilities of the DE-MPAW additive manufacturing system. The flowchart of modeling and designing of tool path plans is shown in Fig. 3.

The part adopted the design idea of parametric modeling, comprehensively considered the shape and size of the part and performed feature decomposition. Taking the complete size reference as a starting point, the position relationship between the

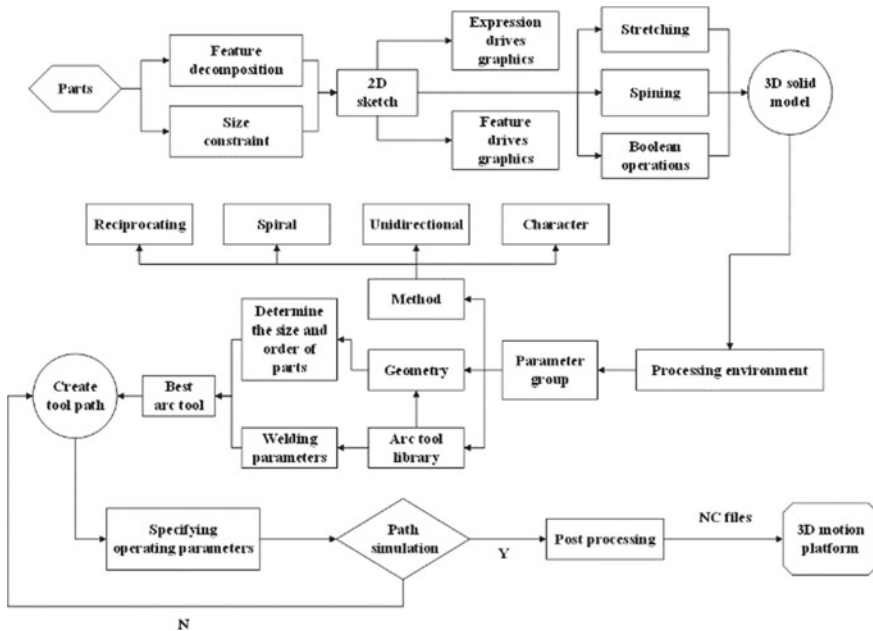


Fig. 3 Planning path and curved surface part model tree in DE-MPAW depositing process

graphic and the coordinate axes which is the size constraint was determined. The system took the input size constraint as the feature parameters, saved and converted into system parameters which can be visually modified in subsequent product design. Similarly, the UG/NX module provides different standard design features. It highlighted the key feature size and positioning size so as to offer an easy call and edition. Graphic expressions can also be used to write features and establish feature sets. By driving the graphics with features and expressions, stretching, rotating and Boolean operating feature shapes in the 2D sketch, the 3D solid model of the part was drawn. A 3D solid model of a simple curved surface part is drawn in Fig. 4 by using UG/NX parametric modeling.

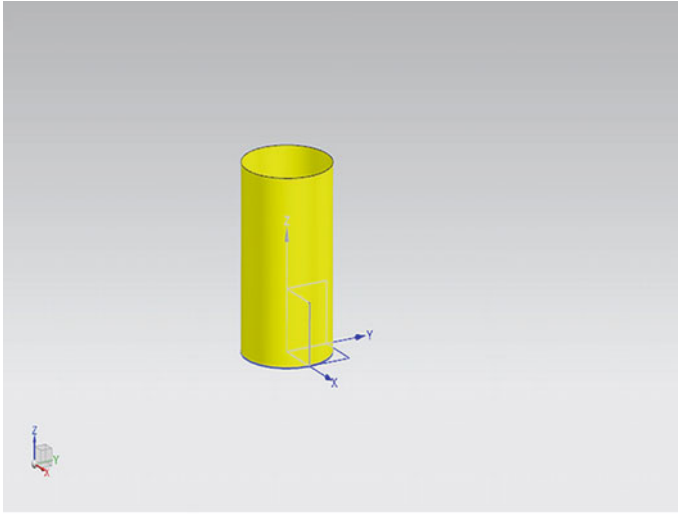
The planning of the stacking tool path of curved surface parts is shown in Fig. 3. Based on the establishment of the three-dimensional solid model, it was transferred to the processing environment module of UG/NX, where the parameter group is set and the stacking order of positions of the parts together with the relevant sizes was determined.

Considering the arc tool information and part size and taking the least travel path as the principle, the best arc tool in the arc tool library was selected, and the appropriate cutting method was chosen among the reciprocating, spiral, unidirectional and character according to the feature shape of the part to create a tool path operation program. After specifying the operating parameters, the simulation experiment of the deposition path was performed to verify the rationality and accuracy of the tool path and made it visual to modify. Finally considering the hardware requirements of the X–Y–Z 3D motion platform, an executable NC file was generated for operation. Figure 5 shows the deposition path simulation process of stacking elliptical columns and cylindrical curved surface parts with the help of DE-MPAW additive manufacturing control system.

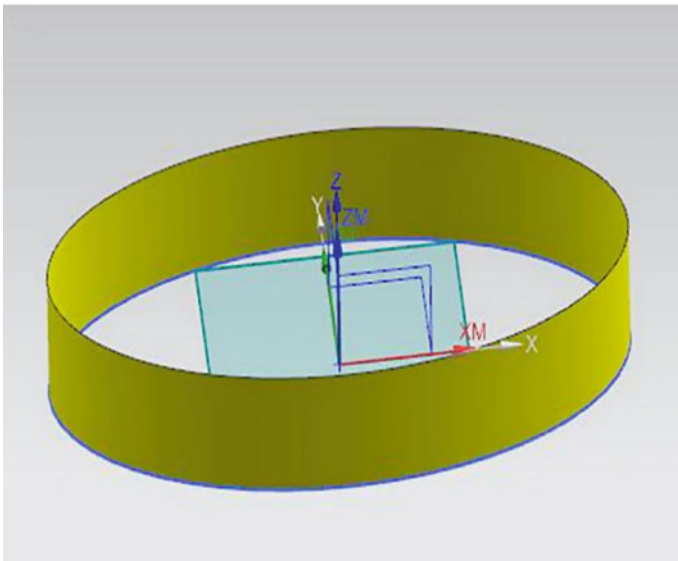
3 Curved Surface Part Forming

In the DE-MPAW additive manufacturing control system, 0.8-mm ER304L stainless steel welding wire was used for stacking oval-shaped simple curved part materials with a long axis of 50 mm and a short axis of 25 mm. The arc tools were chosen according to the welding parameters shown in Table 1, and the stack tool path adopted the characteristic cutting method. At the premise of a 50 A total welding current, the bypass 16 A shunt reduced the current flowing through the substrate and the stacking layer, thereby reducing the problem of melting collapse caused by the overheating of the stacking layer during the stack forming process. The stack forming of elliptic cylindrical curved surface part is shown in Fig. 6, and Fig. 6a shows the welding current signal collected in the stack forming process, while Fig. 6b shows the stack forming part. The measured height of the stack forming part was 24 mm with a total of 24 layers, and the average height of each layer was about 1 mm.

Under the same parameters, 0.8-mm ER304L stainless steel welding wire was selected as the stack forming material to stack cylindrical curved surface parts with

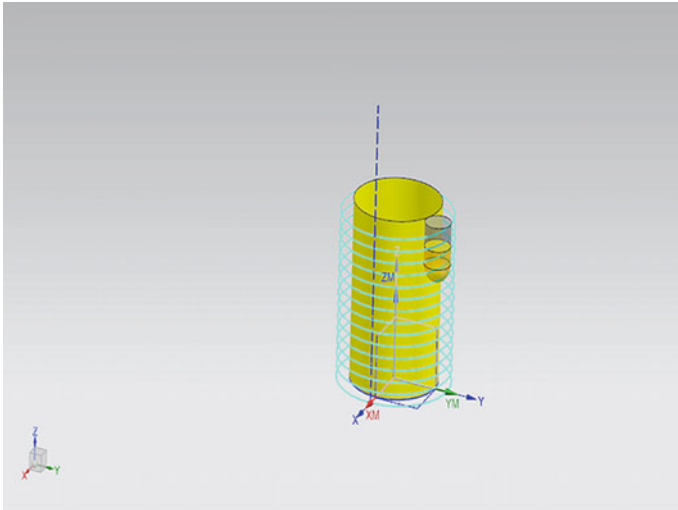


(a) cylindrical model

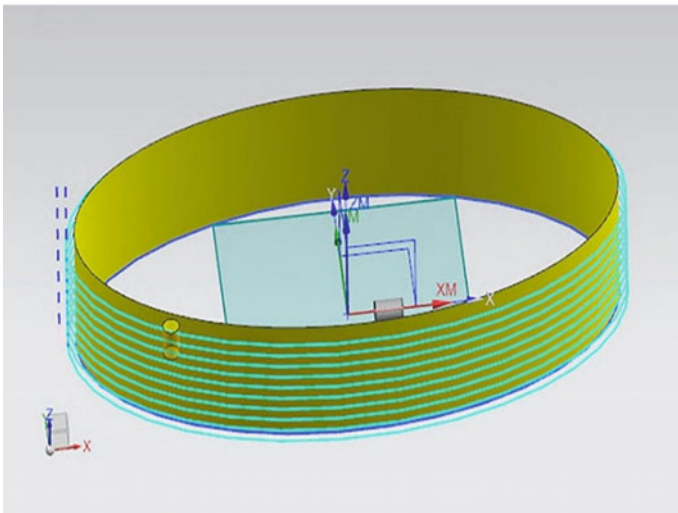


(b) elliptical cylindrical model

Fig. 4 Three-dimensional model with curved surface parts



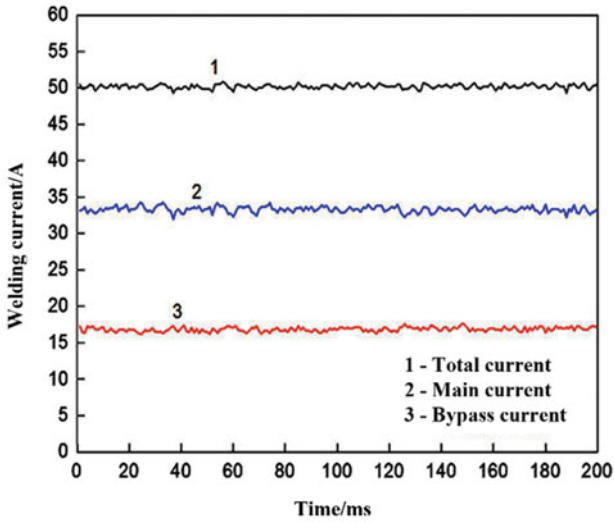
(a) simulation of deposition path of cylindrical surface part



(b) simulation of tool path of elliptic cylindrical surface part

Fig. 5 Curved surface part and deposition path simulation in DE-MPAW system

a diameter of 10 mm and a height of 15 mm. Further, the obtained cylindrical curved parts were surface milled by a machine tool into a pair of stainless steel rings with a diameter of 10 mm and a height of 3 mm. Figure 7 shows the stainless steel ring parts manufactured by the DE-MPAW system and the cylindrical part after stacking, which was the mother part of the stainless steel ring part as shown in Fig. 7a. The measured height of the part was 15 mm with a total of 15 layers which means the



(a) welding current signal acquisition



(b) elliptic cylindrical surface part

Fig. 6 Elliptic cylinder curved surface part depositing in DE-MPAW system

average height of each layer was about 1 mm. Figure 7b shows a pair of stainless steel ring parts with the diameter of 10 mm which was surface milled by a machine tool from the mother part above. It is obvious that the parts were dense and thick without pores, and the surface was well formed with high accuracy.

Fig. 7 Ring parts with stainless material depositing in DE-MPAW system



(a) cylindrical surface part



(b) stainless-steel ring part

4 Conclusions

This paper uses the principle of bypass-coupled arc welding and the method of the micro-plasma arc welding to build a DE-MPAW additive manufacturing control system with low software and hardware costs under the xPC target real-time environment. The system takes the UG/NX as the supporting platform and creates the DE-MPAW additive manufacturing rapid prototyping system arc tool library, which helps realize the integration and automation of curved parts from 3D modeling, tool path planning and simulation to stack forming, significantly shortening processing time and optimizing deposition paths. Combining the heat control effect of bypass current shunt, the phenomenon of melting collapse of the stacking layer is reduced effectively, and dense, thick, well-formed curved parts are manufactured successfully.

References

1. Lu BH, Li DC (2013) Development of the additive manufacturing (3D printing) technology. *Mach Manuf Autom* 42(4):1–4
2. Ding D, Pan Z, Cuiuri D et al (2015) Wire-feed additive manufacturing of metal components: technologies, developments and future interests. *Int J Adv Manuf Technol* 81(1–4):465–481
3. Geng HB, Xiong JT, Huang D et al (2015) Research status and trends of wire and arc additive manufacturing technology. *Welding* (11):17–21
4. Spencer JD, Dickens PM, Wykes CM (1998) Rapid prototyping of metal parts by three-dimensional welding[J]. *Proc Inst Mech Eng Part B J Eng Manuf* 212(3):175–182
5. Li YL, Zhang H, Zhang GY et al (2009) Precision rapid prototyping of steel parts using TIG deposition technology. *Trans China Weld Inst* 30(9):37–40
6. Lu Y, Chen SJ, Shi Y et al (2014) Double-electrode arc welding process: principle, variants, control and developments. *J Manuf Process* 16(1):93–108
7. Huang JK, Shi Y, Li Y et al (2010) Realization of rapid controller prototyping based on DE-GMAW control system. *Trans China Weld Inst* 31(6):37–40
8. Mohamad MH, Zahid MNO (2018) Investigation of roughing machining simulation by using visual basic programming in NX CAM system. 319(1):012010
9. Pedagopu VM (2014) Design and machining simulation of a prismatic part using NX CAD/CAM an overview
10. Liu DS (2018) Research on post processing technology of UGNX CNC lathe. *Manuf Technol Mach Tool* (1):159–164

Arc Contraction Behavior of GMA Welding Process Based on Change of Arc Length at Hyperbaric Air Condition



Jiqiang Huang, Wenwen Guo, Junfen Huang, Long Xue, Jizong Wang, and Yong Zou

Abstract The underwater hyperbaric dry GMA welding method is one of the best emergency maintenance methods for underwater structures. With the increase of ambient pressure, GMA welding quality decreases. The main reason is that GMA welding arc shrinks under high pressure, which leads to the instability of welding process. In order to find out the main factors that affect the contraction of GMA welding arc, theoretical analysis, numerical simulation and experimental verification are used to study the contraction behavior of GMAW arc under high pressure. Based on the governing equation of high-pressure GMA welding arc, the numerical simulations of GMA welding arc under the two conditions of constant arc length and arc length adjustment were carried out by FLUENT software under the environmental pressure of 0.1 MPa, 0.3 MPa, 0.5 MPa and 0.7 MPa, respectively. The contraction of the arc under the two arc length conditions was compared. Through the underwater high-pressure GMA welding test platform, the welding experiments under 0.1, 0.3, 0.5 and 0.7 MPa ambient pressures were carried out. A high-speed camera was used to obtain the arc morphology under different ambient pressures. It was verified the accordance between the experiment results and the simulation data. The results show that the axial and radial dimensions of hyperbaric GMA welding arc decrease with the increase of ambient pressure, showing the phenomenon of arc contraction, especially the arc length decreases significantly, which increases the frequency of short-circuit drop transfer and affects the stability of welding process.

Keywords Hyperbaric welding · Underwater welding · Gas metal arc welding · Arc contraction · Arc self-adjustment · Numerical simulation

J. Huang · W. Guo · J. Huang (✉) · L. Xue · J. Wang · Y. Zou
Beijing Institute of Petrochemical Technology, Beijing 102617, China
e-mail: huangjunfen@bipt.edu.cn

© Springer Nature Singapore Pte Ltd. 2020
S. Chen et al. (eds.), *Transactions on Intelligent Welding Manufacturing*,
Transactions on Intelligent Welding Manufacturing,
https://doi.org/10.1007/978-981-15-6922-7_3

1 Preface

With the rapid development of exploitation and utilization of marine resources, underwater welding technology as an effective method for installation and emergency repair of underwater structures has attracted wide attention. Among the numerous underwater welding methods, the underwater high-pressure dry welding method has become a research hotspot at home and abroad due to its characteristics of good welding quality and high safety [1–3]. Underwater high-pressure dry welding method is conducted in the high-pressure chamber, where the environmental pressure increases as water depth increases, which would lead to welding arc contraction and instability of welding process. The impacts are greater in GMAW; it affects the welding droplet transition and even the whole welding process when the welding parameter adjustment is improper, which seriously deteriorates the underwater welding quality.

Scholars at home and abroad have done a lot of research on the stability and welding quality of high-pressure welding. In the early stage, Perlman did a lot of research on the influence of high-pressure environment on GMAW welding, but the research was not in-depth enough due to the limited research means at that time [4]. Azsar et al. used statistical methods to predict the behavior and stability of GMAW welding arc and proposed that the mismatch of welding current and voltage would have a great impact on the stability of welding process in high-pressure environment [5]. Hart et al. studied the influence of high-pressure GMAW dynamic electrical characteristics and the impact on weld penetration and weld width of environmental pressure, providing reference for quality control of high-pressure welding forming [6]. Akselsen et al. studied the weld performance of X70 pipeline steel under high pressure [7], and Akselsen et al. studied the welding performance of duplex stainless steel under high pressure [8]. The research team of the author studied the weld forming and properties obtained by different welding processes under high-pressure environment [9–11]. Most of the above researches focus on obtaining welding seams of higher quality by various means under high-pressure environment. There are few researches on arc shrinkage causes and shrinkage behaviors under high-pressure environment, failing to reveal the adverse effects of high-pressure environment on the welding process fundamentally.

Jiang et al. studied the high-pressure GTAW arc, revealing the characteristics of the high-pressure GTAW arc, which increased with the increase of environmental pressure [12]. The author studied the characteristics of high-pressure GMAW arc and found that the arc voltage of high-pressure GMAW increased as environmental pressure increases [13]. Li et al. also studied the behavior of high-pressure GMAW welding arc, and again verified that the electric field intensity in the arc column increases with the increase of environmental pressure [14]. These studies have explored the arc behavior in high-pressure environments, but the arc shrinkage behavior mechanism has not been explained systematically.

In this paper, in terms of the high-pressure GMAW welding process, the shrinkage behavior of high-pressure GMAW arc is preliminarily studied by numerical simulation and experimental methods, considering the self-regulating effect of arc, so as to reveal the internal mechanism of arc shrinkage of high-pressure GMAW and provide basic data for the solution of unstable problem in high-pressure welding process.

2 Governing Equation of High-Pressure GMAW Welding Arc

GMAW welding arc can be regarded as the local thermal dynamic equilibrium (LTE) state. It is considered that the plasma of welding arc is optically thin, where the radiation re-absorption in the arc region is so small compared with the total radiation loss that it is ignored. The arc is mapped to the cylindrical coordinate system, and the governing equation of the high-pressure GMAW welding arc is expressed as follows.

When the arc is in a dynamic stable process, the mass of the fluid flowing in and out of the arc region is zero, thus the mass continuity equation is:

$$\frac{1}{r} \frac{\partial}{\partial r}(r\rho v_r) + \frac{\partial}{\partial z}(\rho v_z) = 0 \quad (1)$$

where r is the radial distance between the calculation unit and the welding wire axis, z is the axial distance between the calculation unit and the welding wire end, ρ is the density, v_r , v_z is the radial velocity component and the axial velocity component, respectively.

The energy conservation equation is

$$\begin{aligned} \frac{1}{r} \frac{\partial}{\partial r}(r\rho v_r h) + \frac{\partial}{\partial z}(\rho v_z h) &= \frac{1}{r} \frac{\partial}{\partial r} \left(r \frac{\lambda}{c_p} \frac{\partial h}{\partial r} \right) + \frac{\partial}{\partial z} \left(\frac{\lambda}{c_p} \frac{\partial h}{\partial z} \right) \\ &+ \frac{5k_b}{2e} \left(\frac{j_r}{c_p} \frac{\partial h}{\partial r} + \frac{j_z}{c_p} \frac{\partial h}{\partial z} \right) + \frac{j_r^2 + j_z^2}{\sigma} - S_r \end{aligned} \quad (2)$$

where h is the specific enthalpy, λ is the thermal conductivity, j is the current density, c_p is the specific heat, and S_r is the radiant heat loss, which can be calculated by Stefan-Boltzmann empirical correction formula:

$$S_r = \varepsilon A \zeta T^4$$

where ε is the emissivity of the object, A is the radiation area, and T is the thermodynamic temperature of the blackbody and ζ is constant $5.67 \times 10^{-8} \text{ W}/(\text{m}^2 \text{ K}^4)$.

The radial and axial momentum equations are shown in Eqs. (3) and (4), respectively.

$$\begin{aligned} \frac{1}{r} \frac{\partial}{\partial r} (r \rho v_r^2) + \frac{\partial}{\partial z} (r v_r v_z) = & -\frac{\partial p}{\partial r} + \frac{1}{r} \frac{\partial}{\partial r} \left(2r \mu \frac{\partial v_r}{\partial r} \right) \\ & + \frac{\partial}{\partial z} \left(\mu \frac{\partial v_r}{\partial z} + \mu \frac{\partial v_z}{\partial r} \right) - \frac{2\mu v_r}{r^2} - j_z B_\theta \end{aligned} \quad (3)$$

$$\begin{aligned} \frac{1}{r} \frac{\partial}{\partial r} (r \rho v_z v_r) + \frac{\partial}{\partial z} (\rho v_z^2) = & -\frac{\partial p}{\partial z} + \frac{\partial}{\partial z} \left(2\mu \frac{\partial v_z}{\partial z} \right) \\ & + \frac{1}{r} \frac{\partial}{\partial r} \left(\mu r \frac{\partial v_z}{\partial r} + \mu r \frac{\partial v_r}{\partial z} \right) + j_r B_\theta + \rho g \end{aligned} \quad (4)$$

where μ is the viscosity, and j_r, j_z is the radial and axial current density components, respectively, B_θ is the magnetic field strength and is the pressure.

Current continuity equation:

$$\frac{1}{r} \frac{\partial}{\partial r} \left(r \sigma \frac{\partial \phi}{\partial r} \right) + \frac{\partial}{\partial z} \left(\sigma \frac{\partial \phi}{\partial z} \right) = 0 \quad (5)$$

Ohm's law:

$$j_r = -\sigma \frac{\partial \phi}{\partial r}, \quad j_z = -\sigma \frac{\partial \phi}{\partial z} \quad (6)$$

The magnetic field intensity is given by Maxwell's equation

$$B_\theta = \frac{\mu_0}{r} \int_0^r j_z r \, dr \quad (7)$$

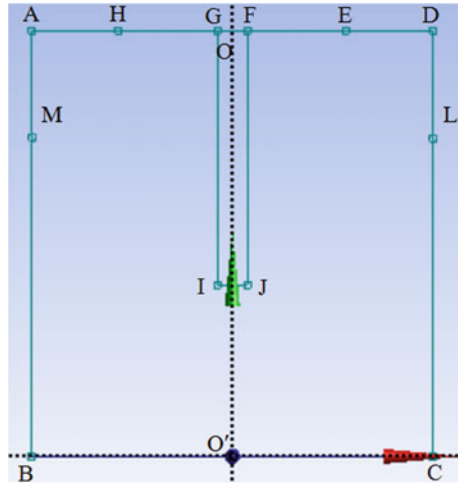
In Eqs. (5), (6), and (7), ϕ is the electric potential, μ_0 is the permeability, and σ is the conductivity.

3 Numerical Simulation of High-Pressure GMAW Arc with Fixed Arc Length

For the numerical simulation of high-pressure GMAW welding arc, some hypothesis is put forward: (1) The welding arc burns stably with internal heat transfer, and the arc is in an incompressible state of laminar flow; (2) the arc is steady-state and axisymmetric, and the arc model can be simplified into a two-dimensional model; (3) the welding base material is a plane, which means the influence of molten pool and molten drop on the arc shape is ignored.

FLUENT software was used in numerical simulation of welding arc. The simulated welding arc area was the ABCD square area as shown in Fig. 1, with a horizontal length of 14 mm and a vertical length of 16 mm. According to the above assumptions,

Fig. 1 Numerical simulation area



the welding arc area is symmetric about the center axis OO' . AH, ED is the welding protection gas inlet; EF, GH is the end edge of the conductive nozzle; GIJF is the edge of the extension part of the welding wire; the diameter of the wire IJ is 1.2 mm; M, L is the lower end of the nozzle; BC is the base material surface; and the arc area is between IJ and BC.

The boundary conditions defined are shown in Table 1, where v_g is the airflow inlet velocity, v_w is the wire feeding velocity, and the physical parameters of the arc refer to the physical parameters of argon at different temperatures [15].

In the numerical model above, the environmental pressure of GMAW welding is set as 0.1, 0.3, 0.5, 0.7 MPa and the welding current is 250 A. The result is shown in Fig. 2; as can be seen from the diagram, with the increase of the environmental pressure, the bright area of the arc gradually becomes thinner and thinner, which shows that the arc tends to decrease in the radial direction when pressure increases.

In order to further observe and compare the high-temperature area of the arc, the high-temperature area is highlighted by adjusting the numerical simulation result

Table 1 Boundary conditions

| Boundary | u | v | φ | T/K |
|----------|-------------------------------------|-------|--|-------------------------------------|
| OO' | $\frac{\partial u}{\partial r} = 0$ | 0 | $\frac{\partial \phi}{\partial z} = 0$ | $\frac{\partial T}{\partial r} = 0$ |
| $O'C$ | 0 | 0 | 0 | 1600 |
| CD | $\frac{\partial u}{\partial r} = 0$ | 0 | $\frac{\partial \phi}{\partial z} = 0$ | 1000 |
| DE | 0 | v_g | $\frac{\partial \phi}{\partial z} = 0$ | 298 |
| EF | 0 | 0 | $\frac{\partial \phi}{\partial z} = 0$ | 1000 |
| FO | 0 | v_w | $-\sigma \frac{\partial \phi}{\partial r} = \frac{1}{\pi R^2}$ | 298 |

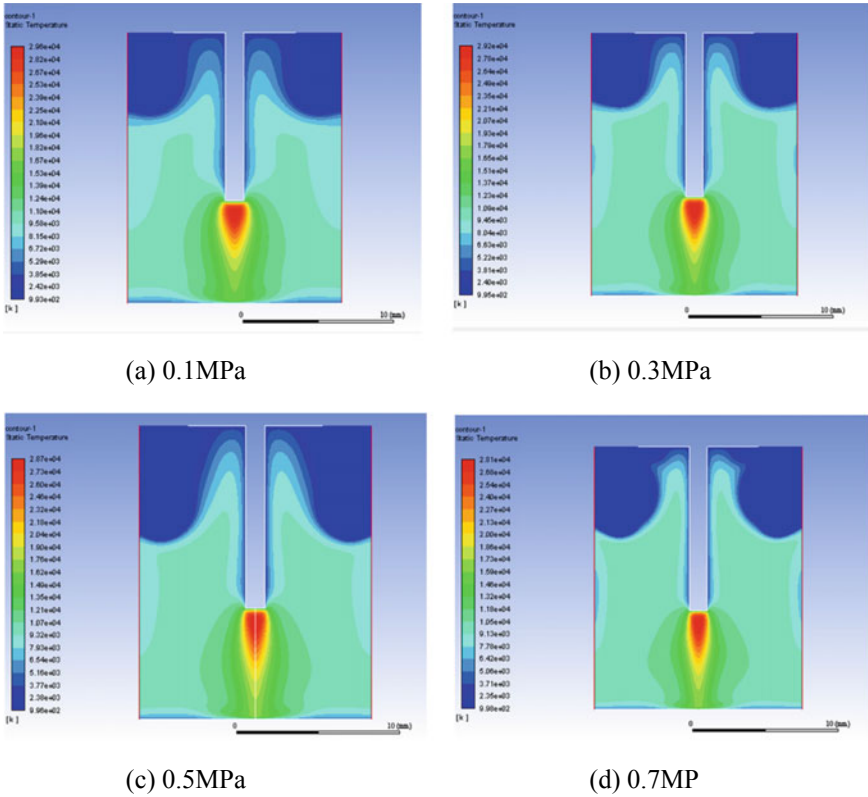


Fig. 2 Simulation results of arc in different ambient pressure/welding current 250 A

ruler to 0–12,000 K, where the temperature higher than 12,000 K is white, as shown in Fig. 3. From the center of the high-temperature area, it is obvious that, with the increase of environmental pressure, the high-temperature of arc area decreased

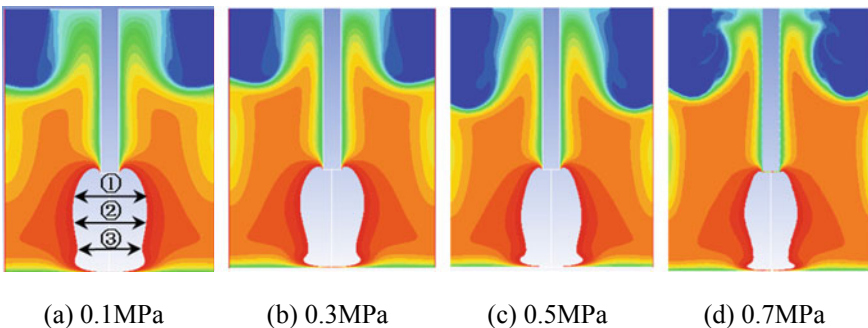


Fig. 3 High temperature of arc in different pressures

Table 2 Radial dimension of the arc at different pressures/mm

| Position | Pressure/MPa | | | |
|----------|--------------|-----|-----|-----|
| | 0.1 | 0.3 | 0.5 | 0.7 |
| ① | 5.2 | 4.5 | 4.0 | 3.3 |
| ② | 5.0 | 4.3 | 4.4 | 3.8 |
| ③ | 4.5 | 3.4 | 3.7 | 3.0 |

significantly in the radial direction. In order to further analysis, three locations are chosen in the height direction of the arc, as shown in Fig. 3a. The diameter of the luminous part of the arc was measured as is shown in Table 2. It can be seen that with the increase of the environmental pressure, the arc diameter in the high-temperature area of the arc decreases significantly, the shape of the arc changes from a bell jar to a bowling ball, and the arc shrinks more obviously in the anode area.

4 Numerical Simulation of High-Pressure GMAW Arc with Arc Length Adjustment

4.1 Arc Length Variation Under High-Pressure Environment

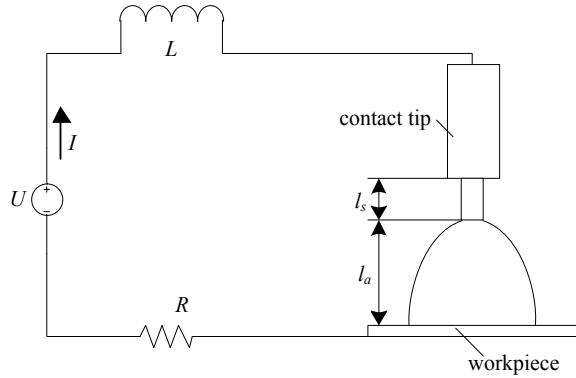
In the actual GMAW welding process, due to the self-regulating effect of arc length, it will be automatically adjusted to the appropriate length as the environment changes to meet the requirements of the minimum voltage principle [16]. In the high-pressure environment, due to the change of heat dissipation conditions in the ambient atmosphere, the dissipated energy of the welding arc increases, resulting in the increase of electric field intensity E of the welding arc [12–14]. Under the condition that the output voltage U of the welding power supply remains unchanged, the changes of arc length l_a of the arc are discussed as follows.

GMAW welding circuit is shown in Fig. 4. The output voltage of welding power supply is U , the equivalent output inductance and resistance in the circuit are denoted as L and R , respectively, and the voltage drop on it is U_L and U_R , respectively. The extension length of welding wire is l_s , the voltage drop of welding wire is U_s , and the voltage drop of arc is U_a ; then there is

$$U = U_R + U_L + U_s + U_a \quad (8)$$

In the formula, $U_R = IR$, $U_L = L \frac{dI}{dt}$, $U_s = \rho \frac{l_s}{s} I$, $U_a = El_a$ where I is the current flowing in the circuit. During the stable GMAW welding process, the welding current does not change much, so the voltage drop on the inductance can be approximately 0. ρ is the wire resistivity; s the cross-sectional area of the welding wire, and for the convenience of discussion, Formula (8) can be written as

Fig. 4 Welding circuit schematic



$$U = K + l_a \left(E - \frac{\rho}{s} I \right) \quad (9)$$

In terms of $K = RI + \rho \frac{l_s + l_a}{s} I$, In the stable welding process, K is basically unchanged. It can be seen from the above equation that under the high-pressure environment, electric field intensity E increases, and under the condition that the output voltage of welding power remains unchanged, arc length l_a decreases as the environmental pressure increases; that is, the arc shrinks in the axial direction.

4.2 Simulation Results of High-Pressure GMAW with Arc Length Variation

On the basis of the high-pressure GMAW welding arc change analysis above, considering the GMAW welding arc axial size changes, correction of the welding arc model is conducted with the environmental pressure of 0.3, 0.5, 0.7 MPa, and the welding current of 250 A, taking the information of arc length changes into the simulation model, as the reference Formula (9). The numerical simulation results are shown in Fig. 5. According to the aforementioned ruler adjustment method, the high-temperature region is highlighted and compared with the simulation results under atmospheric pressure, as shown in Fig. 6. High-temperature area axial and radial dimension measuring position is as shown in Fig. 6a and b, and the results of the measurement are shown in Table 3; it can be seen that with the increase of environmental pressure, electric arc of high-temperature area of the axial and radial dimensions shows a decrease trend, which means that with the increase of environmental pressures, arc contraction appears.

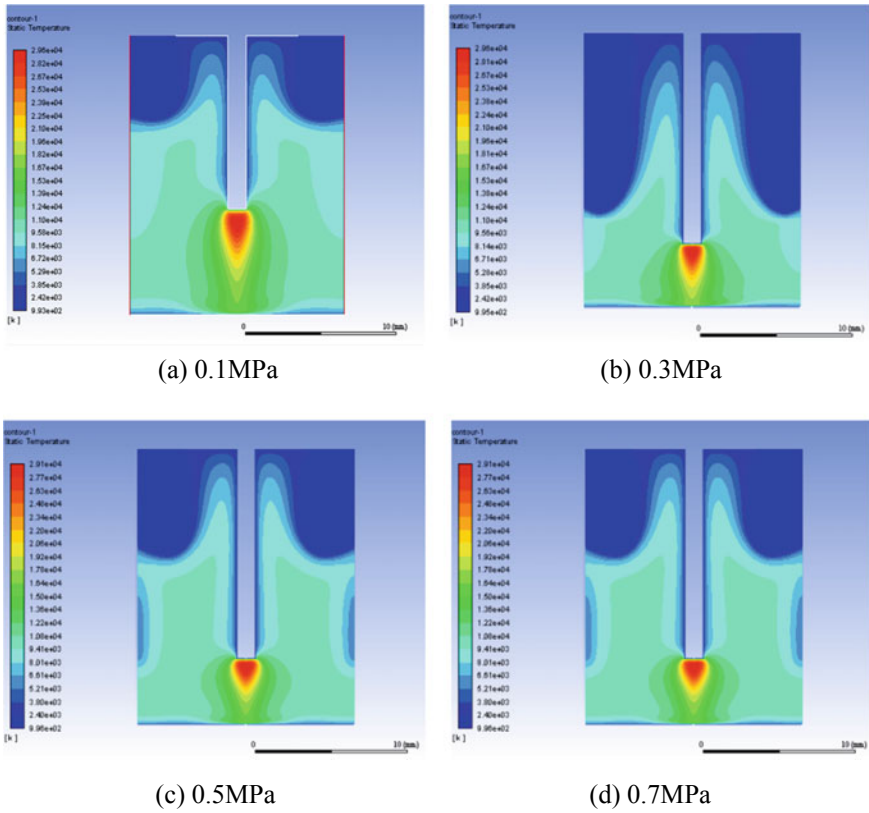


Fig. 5 Numerical simulation results considering the change of arc length

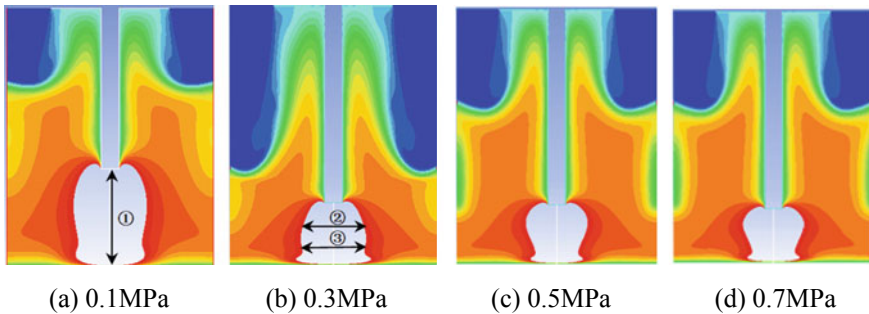


Fig. 6 Measuring position

Table 3 Numerical simulation of arc radial dimension

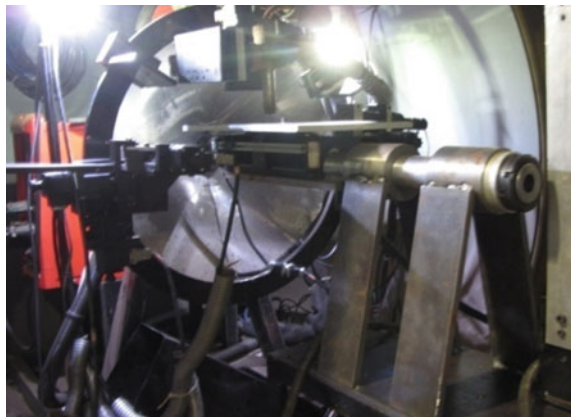
| Position | Pressure/MPa | | | |
|----------|--------------|-----|-----|-----|
| | 0.1 | 0.3 | 0.5 | 0.7 |
| ① | 7.8 | 4.8 | 4.4 | 4.1 |
| ② | 5.4 | 5.2 | 5.2 | 4.8 |
| ③ | 5.3 | 5.0 | 3.5 | 3.9 |

5 Experimental Results and Discussion

With the help of the high-pressure welding test platform (as shown in Fig. 7), the high-pressure GMAW welding test and arc morphology observation are conducted. The high-pressure welding test platform includes the high-pressure test chamber, air compression system, monitoring and control system, welding system and image acquisition system, etc. The block diagram is shown in Fig. 8. The welding power supply is Fronius CMT3200, the image acquisition USES MS55K color digital high-speed camera. Parent metal is made of Q235 steel plate, wire type ER50-6, wire diameter is 1.2, 15 mm wire stem elongation, welding current is 250 A, welding voltage 28.2 V, the welding speed is 25 cm, 1 min, welding protective gas is 80% Ar + 20% CO₂ gas mixture, shielding gas flow to 20 l, 1 min, welding environment pressure: 0.1, 0.3, 0.5, and 0.7 MPa, obtain the high-pressure GMAW welding process of arc photographs as shown in Fig. 9.

The luminous area of the arc image is measured as is shown in Fig. 9, including the axial and radial dimensions of the arc. The specific measurement results are shown in Table 4. Through data analysis, it can be found that with the increase of environmental pressure, the axial and radial dimensions of high-pressure GMAW welding arc both decrease, indicating the shrinkage of high-pressure GMAW arc, which is consistent with the previous simulation results. The simulation results and experimental results

Fig. 7 High-pressure GMA welding equipment



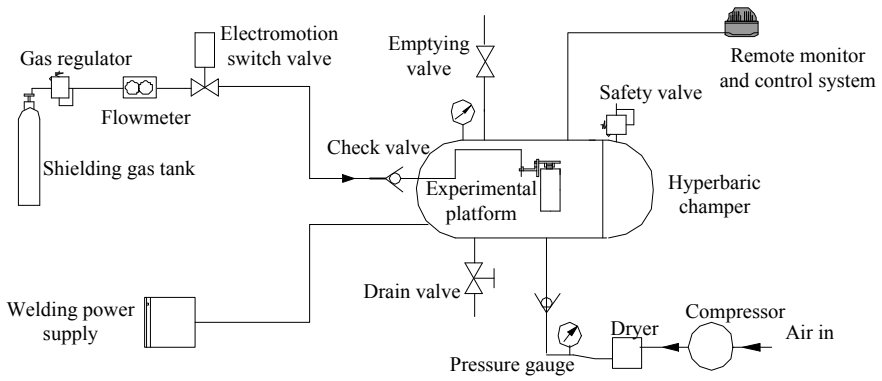


Fig. 8 Schematic diagram of hyperbaric welding equipment

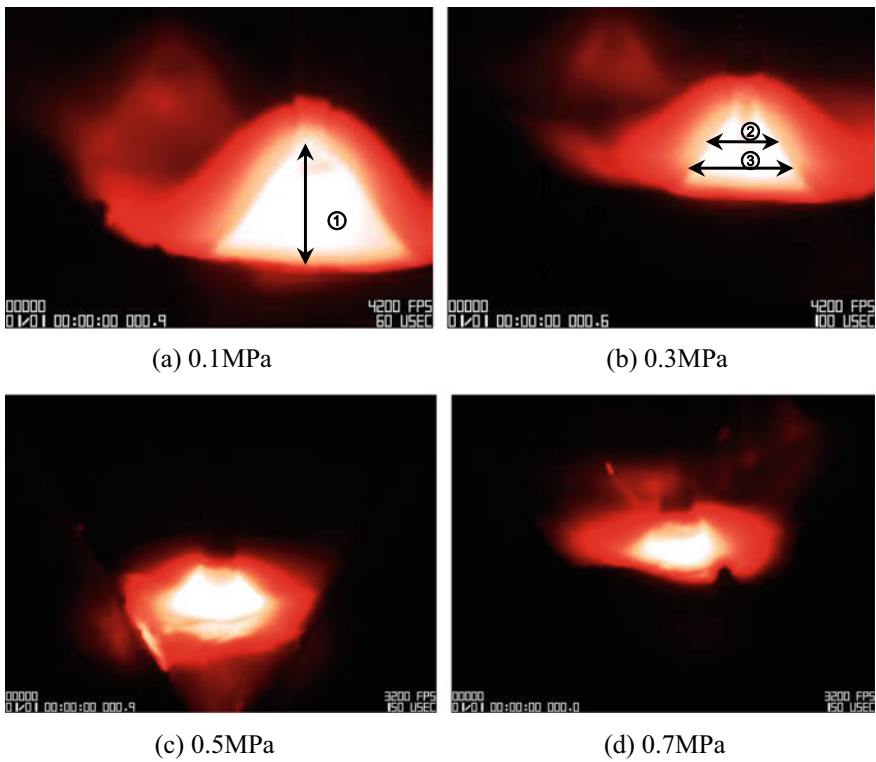
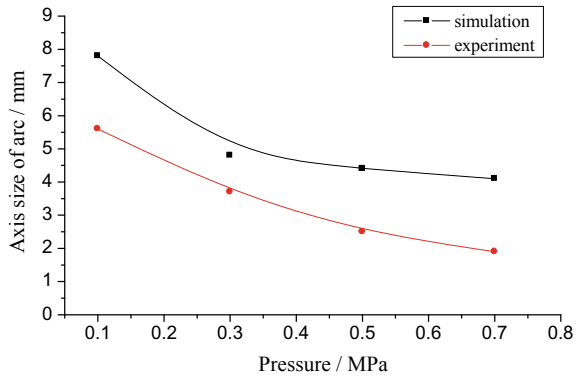


Fig. 9 Pictures of welding arc at different pressures

Table 4 Arc sizes of hyperbaric welding with current 250 A

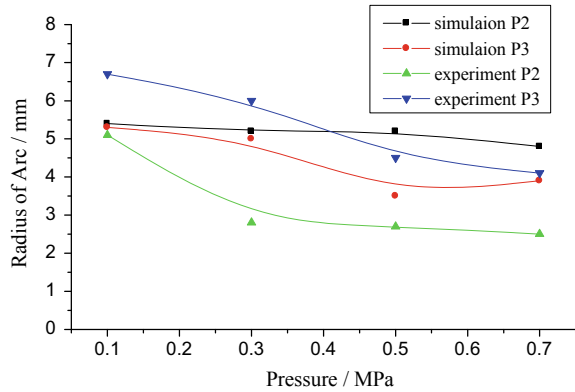
| Position | Pressure/MPa | | | |
|----------|--------------|-----|-----|-----|
| | 0.1 | 0.3 | 0.5 | 0.7 |
| ①/mm | 5.6 | 3.7 | 2.5 | 1.9 |
| ②/mm | 5.1 | 2.8 | 2.7 | 2.5 |
| ③/mm | 6.7 | 6.0 | 4.5 | 4.1 |

Fig. 10 Change of arc length with pressure

of the axial dimension of GMAW welding arc are given in Fig. 10. It can be seen clearly that the sizes of the two results tend to decrease with the increase of welding pressure. However, the axial dimensions in the simulation results are higher than the experimental results, because the influence of arc adaptive adjustment factors on the decrease of arc axial dimensions is considered in the simulation process. In fact, there are many factors affecting the decrease of arc axial dimensions, which need to be further explored. According to the experimental and simulation results, the axial dimension (arc length) of the arc decreases significantly in the high-pressure GMAW welding process. If the arc length is too short, it will directly affect the way of droplet transition, resulting in an increase of short-circuit frequency in the welding process and the instability of the arc. Therefore, in the actual high-pressure GMAW welding process, the welding voltage should be appropriately increased according to the increase of the environmental pressure, which is conducive to the welding arc to maintain a proper arc length, to avoid frequent short circuit caused by the arc length is too low, so as to improve the stability of the arc.

Figure 11 shows the high-pressure GMAW welding arc radial size of the simulation and experiment results, both of which decrease as the environment pressure increases. The reduction in simulation results is smaller than in the experimental results. The reasons of the difference may be: (1) the simulation results of the bright area sets 12,000 K (when the degree of ionization of about 0.5%) as the boundary, but the actual welding bright area is slightly different; (2) during the experimental welding, the dynamic change of high-pressure GMAW welding arc is large. The

Fig. 11 Change of arc radial sizes with ambient pressure



subjects of the study all choose the arc images with the largest luminous area of the burning arc, but there are differences in the morphology of the luminous area, and there are certain differences in the determination of the arc measurement position. But generally speaking, the simulation and experimental results of arc radial dimension have a good agreement, and both reflect the trend that radial dimension decreases with the increase of environmental pressure.

6 Conclusion

On the basis of the high-pressure GMAW welding arc simulation with constant arc length, considering arc length adjustment, the high-pressure GMAW welding arc is simulated, which is compared with experimental results welding test. The results show that axial and radial sizes of high-pressure GMAW welding arc are gradually contracted with the increase of environmental pressure, especially that the arc length is reduced obviously, thus increasing the short-circuit transition frequency and affecting the stability of welding process. In the actual welding process, welding voltage should be appropriately improved.

Acknowledgements Project jointly supported by Beijing Natural Science Foundation and Beijing Education Commission (KZ201810017022).

References

1. Woodward N (2006) Developments in diverless subsea welding. *Weld J* 10:35–39
2. Richardson IM, Woodward NJ, Armstrong MA, Berge JO (2010) Developments in dry hyperbaric arc welding—a review of progress over the past ten years. In: International workshop on

- the state of the art science and reliability of underwater welding and inspection technology, Houston, Texas, USA, pp 65–83
3. Shi Y, Zhang X, Lei Y et al (2000) Advances in welding technology under harsh conditions. *J Mech Eng* 13–16
 4. Azsar AS, Woodward N, Fostervoll H, Akselen O (2012) Statistical analysis of the arc behavior in dry hyperbaric GMA welding from 1 to 250 bar. *J Mater Process Technol* 212(1):211–219
 5. Hart P, Richardson IM, Nixon JH (2001) The effects of pressure on electrical performance and weld bead geometry in high pressure GMA welding. *Weld World* 45(11/12):29–37
 6. Perlman M, Pense AW, Stout RD (1969) Ambient pressure effects on gas metal-arc welding of mild steel. *Weld J* 6:231–238
 7. Akselsen OM, Fostervoll H, Ahlen CH (2009) Hyperbaric GMA welding of duplex stainless steel at 12 and 35 bar. *Weld J* 88(2):21s–28s
 8. Akselsen OM, Fostervoll H, Harsvcer A et al (2006) Mechanical properties in hyperbaric GTA welding of X70 pipeline. In: Proceedings of the sixteenth international offshore and polar engineering conference, San Francisco, California, USA, pp 152–159
 9. Huang J, Xue L, Huang J et al (2016) Arc behavior and joints performance of CMT welding process in hyperbaric atmosphere. *Acta Metall Sin* 52(01):93–99
 10. Liu H, Xue L, Huang J et al (2016) Influence of environmental pressure on strength and toughness of weld by gas metal arc welding. *J Shanghai Jiao Tong Univ* 50(10):1613–1617
 11. Huang J, Xue L, Huang J et al (2016) Effects of welding polarity on weld appearance of pulsed GMAW in hyperbaric environments. *J Mech Eng* 52(18):64–69
 12. Jiang LP, Wang Z, Jiao X et al (2007) Characteristics of GTAW arc in underwater welding under high-pressure air condition. *Trans China Weld Inst* 28(6):1–4
 13. Jiqiang H, Long X, Tao L et al (2012) Arc characteristics of GMA welding in high-pressure air condition. *China Weld* 21(4):26–31
 14. Li K (2014) Study on GMAW arc behavior and droplet transition by high pressure dry method. Dissertation, Harbin Institute of Technology
 15. Fan HG, Kovacevic R (1998) Dynamic analysis of globular metal transfer in gas metal arc welding—a comparison of numerical and experimental results. *J Phys D Appl Phys* 31(20):2929–2941
 16. Yin S (2016) Process foundation and application of gas shielded welding. *J Mech Eng* 60–61

Online Defect Detection of Laser-Arc Hybrid Welding Based on Spectral Information and MSPC



Chengyuan Ma, Bo Chen, Caiwang Tan, Xiaoguo Song, and Jicai Feng

Abstract Online monitoring of welding quality is always a research hotspot. The online detection of welding defects can effectively improve the processing efficiency and ensure the welding quality. In this paper, a quality detection system for laser-arc hybrid welding process has been established by using a spectrometer. Principal component analysis (PCA) and multivariate statistical process control (MSPC) were used to analyze the collected spectral information. The results showed that the welding defects such as oxide inclusion and the lack of penetration could be effectively detected by selecting the specific elements, such as the spectral lines of Fe/Cr/Ni/Ar/O.

Keywords Spectral information · Laser-arc hybrid welding · Welding defects detection · PCA · MSPC

1 Introduction

With the development of laser, laser manufacturing including laser welding, laser cladding and laser additive manufacturing has been paid more and more attention by researchers [1]. A series of physical and chemical changes will occur in welding, including arc spectrum, acoustic spectrum, changes in welding current and voltage [1, 2]. It is well known that laser-induced plasma is produced during laser-arc hybrid welding process, and the quality of weld could be reflected by the characteristics of the plasma [3]. Therefore, real-time monitoring of signals can provide reliable basis for welding quality prediction.

C. Ma · B. Chen (✉) · C. Tan · X. Song · J. Feng
State Key Laboratory of Advanced Welding and Joining,
Harbin Institute of Technology, Harbin 150001, China
e-mail: chenb@hit.edu.cn

Shandong Provincial Key Laboratory of Special Welding Technology,
Harbin Institute of Technology at Weihai, Weihai 264209, China

© Springer Nature Singapore Pte Ltd. 2020
S. Chen et al. (eds.), *Transactions on Intelligent Welding Manufacturing*,
Transactions on Intelligent Welding Manufacturing,
https://doi.org/10.1007/978-981-15-6922-7_4

To detect defects in welding from spectral information, many researchers have done a lot of work. Shea et al. used spectrum to monitor hydrogen pollution in welding arc in real time to control hydrogen and hydrogen pores in weld metal [4]. Morgan et al. studied the relationship between the non-fusion defects caused by laser spot offset from the joint and plasma spectral characteristics in narrow gap laser welding. The results of offline analysis of spectral intensity and electronic temperature showed that the combination of spectral characteristics and visual sensing is beneficial to the hybrid sensing tracking of weld seam [5]. Kong et al. used fiber laser with the maximum output power of 4 kW to weld 1.2 and 1.5 mm high-strength galvanized steel plate DP980. Their research found that the strength of spectral line in the welding process was related to welding spatter caused by zinc vapor, and the electronic temperature of plasma calculated by Boltzmann plot method could reflect whether there were pores in the weld [6]. Sibillano et al. conducted an online spectral study of butt welding of AA5083 aluminum alloy, which compared the effects of different shielding gas nozzles and the flow rate on the spectral strength during welding. Their results showed that when the state of shielding gas changes, it can be well reflected in the spectral characteristics [7]. Ribic et al. studied YAG laser-TIG hybrid welding plasma by means of spectroscopy, and studied the influence of welding current and heat source spacing on electron temperature and conductivity of plasma. The composition of plasma under different welding currents was calculated, and the fusion depth under different welding currents was deduced according to the heat transfer model and fluid model [8]. Harooni et al. studied the influence of oxide film on arc electron temperature and weld quality of AZ31B Al-Mg alloy during zero-gap laser lap welding. It was found that, compared with the complete cleaning of the oxide film, when the oxide film was not cleared, the electron temperature and fusion depth obtained based on the spectral lines of MgI at wavelengths of 383.83 and 517.26 nm were relatively high, but pores appeared on the surface [9].

In addition to time domain analysis of electron temperature and strength of characteristic spectral line, some researchers have applied statistical and machine learning algorithms to spectral data processing. By using spectral information and principal component analysis (PCA), Colombo et al. proposed a monitoring scheme to measure the gap in laser lap welding of galvanized steel. This scheme can not only monitor the assembly gap value but also evaluate the position where spectral emitted. This study also found a strong correlation between laser back reflection and assembly gap [10]. Zhang et al. studied the key technology of online detection of internal pores of Al-Mg alloy in pulsed GTAW by means of spectral detection. The internal pores in aluminum alloy welding could be measured online. The samples with different porosity were tested and characterized by SEM and EDS. The spectral lines of metal and hydrogen were selected before extracting the characteristics. The relationship between the principal component coefficients of HI and MgI lines and porosity was studied quantitatively. On this basis, an improved characteristic parameter, the absolute value coefficient of the H spectrum in first principal component, was proposed for the detection of internal porosity. Finally, feature reduction and visualization were realized through PCA and *t*-distribution random neighborhood embedding, and pores

density was successfully classified [11]. Lacroix and Jeandel [12] studied the spectral characteristics of plasma in pulsed Nd: YAG laser welding. The change of electron temperature directly related to material heat transfer under different processing modes was studied. The maximum temperature observed was 7150 K, which was lower than the CO₂ laser welding. Welding shielding gas has a cooling effect on plasma. The higher the velocity of shielding gas, the stronger the cooling effect. The temperature at the top of the keyhole is higher than that of the rest of the plasma.

In this paper, the detection of defects in 316LN welding was studied. 316LN is austenitic stainless steel, which is a kind of structural material commonly used in nuclear power field. N element plays the role of solution strengthening and aging strengthening to improve the strength, hardness, corrosion resistance and wear resistance of steel. 316LN stainless steel has excellent mechanical properties at high temperature, good weldability, corrosion resistance and fatigue resistance. It is a widely used material for nuclear reactor structures. Therefore, the quality of welding is of great significance. In this paper, a quality detection system for laser-arc hybrid welding process was established by using a spectrometer. Due to the large amount of spectral information, it is necessary to reduce the dimensionality. Thus, the principal component analysis (PCA) and multivariate statistical process control (MSPC) were used to analyze the collected spectral information. Since MSPC is a data-driven approach, compared with other machine learning algorithms, MSPC does not need any wrong data during the training phase. In addition, MSPC chart can continuously display variable status and be updated over time to perform dynamic monitoring.

2 Experiment

The experiments were conducted based on laser-arc hybrid welding system, the system was consisted of an Ytterbium-doped fiber laser (IPG YLS-6000), an arc welding power source (LINCOLN R350) and a KUKA six-axis robot with a self-designed laser-arc hybrid welding torch. The maximum output power of the laser used is 6000 W with wavelength of 1060–1070 nm; the beam parameter product (BPP) is greater than or equal to 4.0. An AvaSpec multichannel fiber optic spectrometer matched with a collecting fiber optic probe, of which the spectral resolution is 0.052 ± 0.001 nm, was used to collect the emission spectra ranging from 315 to 420 nm. The schematic diagram of the experimental system is shown in Fig. 1.

The butt-welding experiment was carried out with 316LN stainless steel plate cut by flame, and the dimensions of plate were $150 \times 75 \times 6$ mm. To explore the influences of the oil and oxide pollution on the spectrum, in the first experiment, the groove was cleaned before welding, but the oxide film generated by flame cutting was retained, as shown in Fig. 2a. In the second experiment, the welding gap was enlarged to 2 mm in the middle of the plate, as shown in Fig. 2b. The filler metal is 316L.

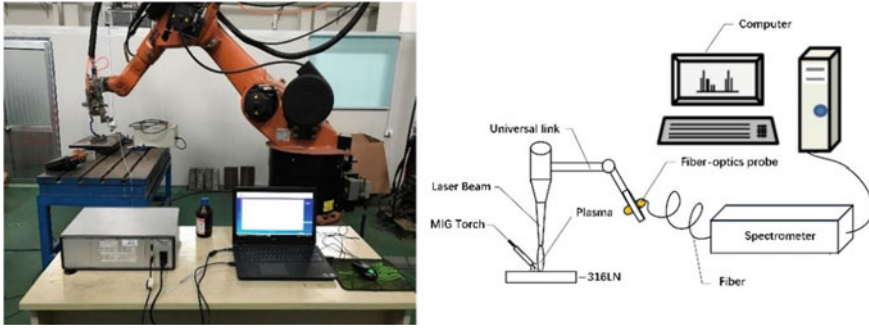


Fig. 1 Schematic diagram and photograph of welding system and spectral acquisition system

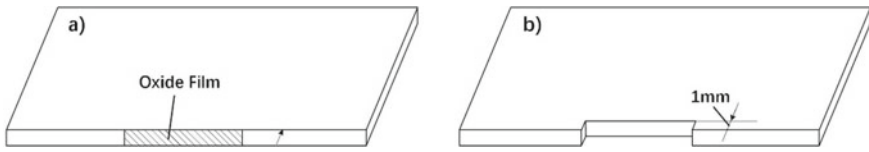


Fig. 2 Schematic diagram of base metal. a Retain the oxide film. b Welding gap variation

In this paper, the laser power, welding current, welding speed and the laser-arc distance were, respectively, set to 3300 W, 150 A, 0.8 m/min and 3 mm. The spectrometer was used to collect spectral signals during welding. The integral time was 10 ms, and the number of averages was 2.

3 Results and Discussion

3.1 Multivariate Statistical Process Control

In practice, multivariate statistical analysis often encounters two situations: One is to monitor the stability of a given sample of multivariate observations, and the other is to set a control field for future observations. The commonly used multivariate statistical control charts include square prediction error (SPE) chart, T^2 chart. The SPE chart depicts the deviation of the measured value from the predicted value at a certain moment, but it is difficult to give the predicted value to the spectral signal in the welding process. Therefore, T^2 chart based on Hotelling statistics was selected to conduct real-time monitoring of the spectral signals of the welding process. A T^2 control chart can handle no less than two variables, so that multiple characteristic spectral lines can be monitored simultaneously.

In monitoring the stability of a given sample, historical normal data are used to train a dimensionality reduction model such as PCA, in which high-dimensional feature data are represented by low-dimensional features (such as dominant principal components and independent components) [13]. The algorithm of PCA is briefly elaborated below.

Principal component analysis (PCA) is the most widely used in data reduction and data compression. The main idea of PCA is to find a k -dimensional space to map the original n -dimensional data into the k -dimensional space and retain the main information of the data. Each axis in the k -dimensional orthogonal eigenspace is also called the principal component (PC). The choice of the new axis is closely related to the data itself. Among them, the selection of the first new coordinate axis is the direction with the largest difference in the original data, the selection of the second new coordinate axis is the plane with the largest variance in the orthogonal plane with the first coordinate axis, and the third axis is the plane with the largest difference in the orthogonal plane with the first and second axis. And so on, you get k -dimensional space of these axes. With the new axis obtained in this way, we find that most of the variance is contained in the first k axis, and the variance in the latter axis is almost 0. Therefore, we can ignore the remaining axis and only keep the first k axis that contains most of the variance. In fact, this is equivalent to only retaining the dimension features that contain most of the variance, while ignoring the feature dimensions that contain almost zero variance, so as to realize the dimensionality reduction processing of data features.

When implementing multivariate statistical process control, it is necessary to establish a principal component model to reflect the normal process. The historical data reflecting the normal process were collected, the principal component analysis was carried out on these data, and the principal component model was established. Since the results of principal component analysis are affected by the data scale, the data should be standardized first, the mean value of each variable should be subtracted, and then divided by its standard deviation. It could be expressed as following equation:

$$\bar{X}_s = [X - (1 \ 1 \ \dots \ 1)^T M] \text{diag} \left(\frac{1}{s_1} \ \frac{1}{s_2} \ \dots \ \frac{1}{s_m} \right) \quad (1)$$

where $M = [m_1 \ m_2 \ \dots \ m_m]$ is the mean value of X , $s = [s_1 \ s_2 \ \dots \ s_m]$ is the standard deviation of X .

In this paper, 52 spectral lines from Fe/Cr/Ni/Ar/O elements were selected from the original data as the input variable of PCA. The original spectral data in an integration time are shown in Fig. 3. The data analysis methods library provided by Scikit-learn [14] was used to standardize the data and reduce the dimension by principal component analysis, so as to obtain the interpretation of data changes by principal component models with different numbers of PC. As shown in Fig. 4, PCA results showed that the first six principal components contributed more than 99.5% of the variance. Furthermore, the original 52-dimensional data can be reduced to

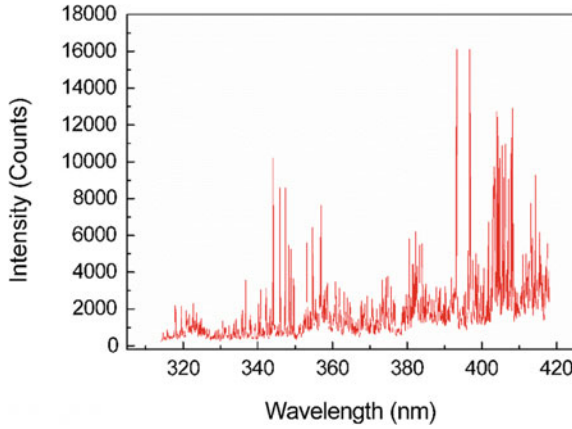


Fig. 3 Original spectral data in an integration time

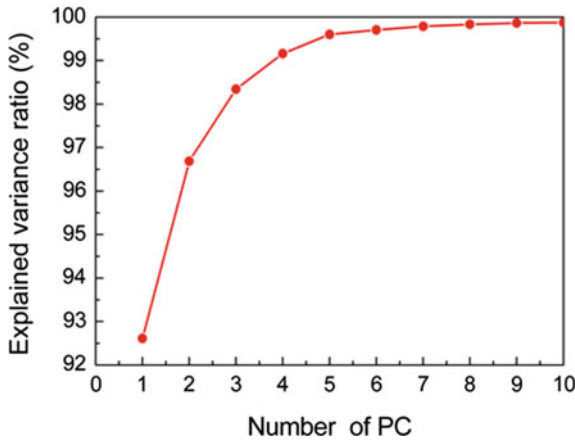


Fig. 4 Interpretation of data changes by principal component models with different principal component numbers

six-dimensional data through PCA without losing most of the information in the data.

After PCA dimension reduction, six linearly independent principal components of spectral data are obtained, and MSPC control chart can be drawn by using these principal components.

Stability monitoring is considered first. Assume that monitored vector X_1, X_2, \dots, X_n independent identical distribution, and distribution obey $N_p(\mu, \Sigma)$, then calculated the T^2 for the j point:

$$T_j^2 = (x - \bar{x})^T S^{-1} (x - \bar{x}) \tag{2}$$

where x is the observations of sample, \bar{x} is the mean value of the observations, S is

the covariance matrix of the variables in the sample, and $S = \begin{bmatrix} s_{11} & \cdots & s_{1n} \\ \vdots & \ddots & \vdots \\ s_{m1} & \cdots & s_{mn} \end{bmatrix}$, where

$s_{ij}(i, j = 1, 2, \dots, p)$ is the covariance of the variable x_i with x_j .

Equation (1) has standardized the X , so $\bar{x} = 0$; consequently, the above equation can be simplified as:

$$T_j^2 = x^T S^{-1} x \tag{3}$$

Then, the T^2 value was drawn on the time axis, and the lower control limits was set as zero, while the upper control limits could be set as $\chi_p^2(0.01)$ and its value can be obtained by looking up the table. When the T^2 value is below the upper control limits (UCL), the process can be considered stable within the 99% confidence interval.

Then consider setting up control fields for future observations. If the current observed process is stable, the control fields of a single observed value in the future can be predicted based on the current observed value. Assume that monitored vector X_1, X_2, \dots, X_n independent identical distribution, and the distribution obey $N_p(\mu, \Sigma)$; let X be a future observation from the same distribution, then [15]

$T^2 = \frac{n}{n+1}(X - \bar{X})^T S^{-1}(X - \bar{X})$ obeys $\frac{(n-1)p}{n-p} F_{p,n-p}$ distribution.

So, for each new observation x , apply Eq. (3) in chronological order to get T^2

$$T = \frac{n}{n+1} x^T S^{-1} x \tag{4}$$

where x is the sample data, S is the covariance matrix of the stable data, and n is the number of samples of the stable data.

It is important to note that process changes are not necessarily caused by changes that adversely affect the process. If the T^2 statistic or other statistic exceeds the control limits, and it can only indicate that there are sample points in the system that are far away from the data aggregation range, that is, specific points [15]. The existence of such points is sometimes caused by the characteristics of the process itself. When analyzing the statistical process control chart, it is necessary to combine the specific process knowledge, that is the characteristics of the welding process itself, which is of great significance for obtaining correct results.

The basic drawing steps of the statistical process control chart used to monitor the stability of welding process are as follows:

- (a) Determine the variables to be monitored and collect spectral data from the normal welding process.
- (b) The monitored variables were dimensionalized by PCA, and the T^2 value was calculated according to Eq. (3). After the UCL was determined, the control chart was drawn to observe the process stability.
- (c) On the basis of stable process, UCL of future observations could be set as:

$$UCL = \frac{(n - 1)p}{n - p} F_{p, n-p}(0.01)$$

The newly collected data were dimensionally reduced by PCA, and the T^2 value was calculated in time sequence according to Eq. (4).

3.2 Explanation of Statistical Process Control Chart

The T^2 value was calculated according to the above steps, the control chart of normal welding process was shown in Fig. 5, and the control chart of welding process with oil and oxide film was shown in Fig. 6.

Fig. 5 Control chart of normal welding process

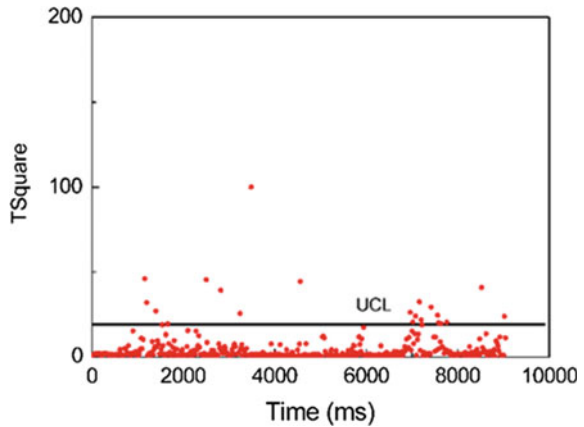


Fig. 6 Control chart of welding process with oil and oxide film

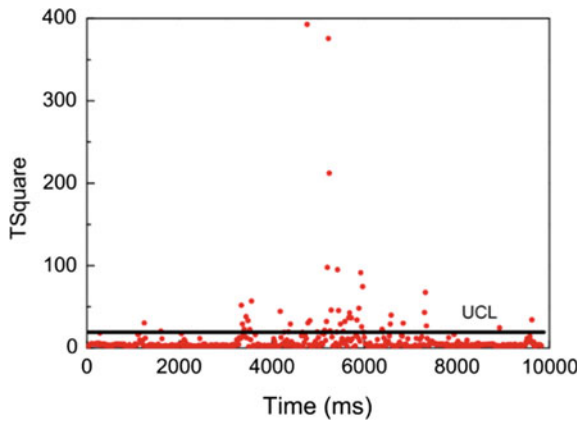




Fig. 7 Photograph of weld with oxide film

As shown in Fig. 5, in the normal welding process, only a small part of sporadic data exceeded the control limits, which was evenly distributed throughout the whole welding process with a small extent of deviation, which was a normal phenomenon due to the random fluctuation caused by the unstable transition of melt drops in MIG welding. However, in the middle of Fig. 6, there are a large volume of data beyond the control limit. These data are concentrated in the middle of the weld, and the range of data beyond the control limit is very large. It can be considered that there is something abnormal in the welding process here.

Abnormal causes can be analyzed by the PCA load matrix. The data analysis methods library provided by Scikit-learn [14] were used to calculate the load matrix of principal components, and the five spectral lines with the largest load among the four principal components were selected and drawn as Fig. 8, in which the spectral lines of oxygen elements were marked red and the spectral lines of other elements were marked blue. As shown in Fig. 8, three of the five spectral lines with the largest load on the first PC came from O element. Two of the five spectral lines with the largest load on the second principal component came from the O element. Three of the five spectral lines with the largest loading on the third and fourth principal components also came from O element. It can be seen that the characteristic spectral line of oxygen has the largest load on the first, second, third, and fourth principal components. Combined with the actual welding situation (as shown in Fig. 7), it can be judged that the oxygen content of the weld is too high.

The control chart of welding gap variation was calculated according to the above steps, as shown in Fig. 9, and the photograph of the weld was shown in Fig. 10.

In Fig. 9a, it can be found that the T^2 value of few sampling points exceeded the control limits before 3000 ms. However, there was a large number of points exceeded the control limits between 3000 and 6200 ms. After 6200 ms, the T^2 value of the point increased significantly and exceeded the control limits rapidly. In Fig. 9b, due to the axis scale, the upper control limits ($\chi_6^2(0.01) = 16.812$) almost overlapped with the coordinate axis. This control limits for the indices was calculated on a confidence limit of 99%. Some of these samples exceeded the control limits, these data are classified as the abnormal data.

By comparing the appearance of the weld (Fig. 10), it could be confirmed that after 2000 ms, due to the sudden change of the gap, there was an underfill defect. After 6200 ms, due to the sudden change of gap, the lack of penetration occurred.

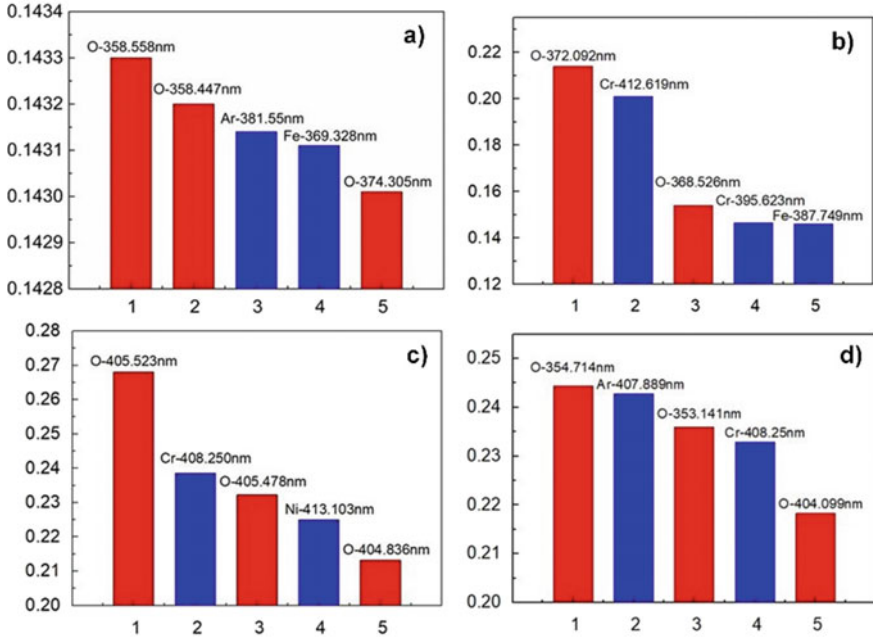


Fig. 8 Five spectral lines with the largest load in the first four principal components. a First PC b second PC c third PC d fourth PC

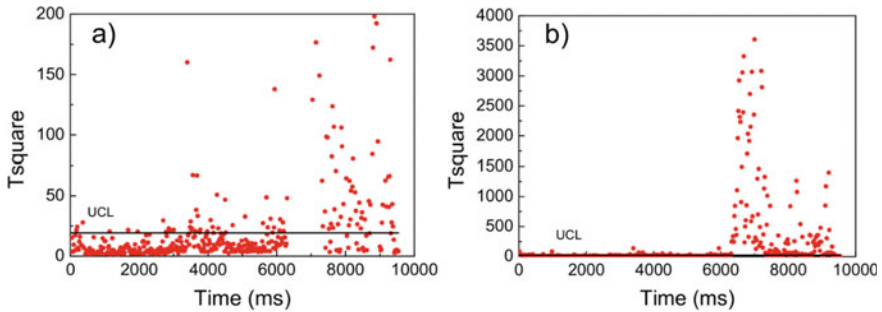


Fig. 9 Control charts of underfill and lack of penetration. a $T^2 \leq 200$ b $T^2 \leq 4000$

4 Conclusions

In this paper, the detection of oxide inclusion and the lack of penetration was carried out. The conclusions are as follows:

- (a) For highly correlated spectral data, PCA before MSPC can reduce the dimensionality of the original data, reduce the computation and the requirements on computing power, which is conducive to the realization of online monitoring.

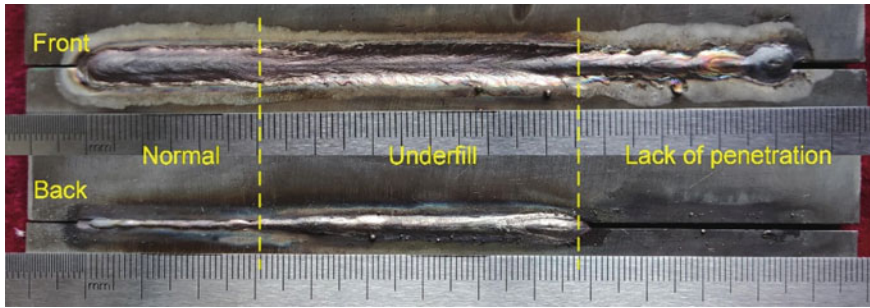


Fig. 10 Appearance of underfill and lack of penetration

- (b) Multivariable statistical process control can accurately identify the adverse effects of oxide inclusions and gap changes on the welding process. As a data-driven approach, MSPC can simultaneously detect multiple defects in the welding process, but it cannot classify them.

Acknowledgements This work was supported by the National Key Research and Development Program of China under the Grant (No. 2018YFB1107900), Shandong Provincial Natural Science Foundation, China, under the Grant (No. ZR2017MEE042), Shandong Provincial Key Research and Development Program under the Grant (No. 2018GGX103026).

References

1. You D, Gao X, Katayama S (2014) Multisensor fusion system for monitoring high-power disk laser welding using support vector machine. *IEEE Trans Industr Inf* 10(2):1285–1295
2. Steen WM, Mazumder J (2010) *Laser material processing*. Springer, London
3. Blackmon DR, Kearney FW (1983) A real time approach to quality control in welding. *Weld J* 3739(8):37
4. Shea JE, Gardner CS (1983) Spectroscopic measurement of hydrogen contamination in weld arc plasmas. *J Appl Phys* 54(9):4928–4938
5. Nilsen M, Sikström F, Christiansson A-K et al (2017) Vision and spectroscopic sensing for joint tracing in narrow gap laser butt welding. *Opt Laser Technol* 96:107–116
6. Ma J, Kong F, Carlson B et al (2013) Two-pass laser welding of galvanized high-strength dual-phase steel for a zero-gap lap joint configuration. *J Mater Process Technol* 213(3):495–507
7. Sibillano T, Ancona A, Berardi V et al (2006) A study of the shielding gas influence on the laser beam welding of AA5083 aluminum alloys by in-process spectroscopic investigation. *Opt Lasers Eng* 44(10):1039–1051
8. Ribic B, Burgardt P, DebRoy T (2011) Optical emission spectroscopy of metal vapor dominated laser-arc hybrid welding plasma. *J Appl Phys* 109(8)
9. Harooni M, Carlson B, Kovacevic R (2014) Detection of defects in laser welding of AZ31B magnesium alloy in zero-gap lap joint configuration by a real-time spectroscopic analysis. *Opt Lasers Eng* 56:54–66
10. Colombo D, Colosimo BM, Previtali B et al (2012) Through the optical combiner monitoring in remote fiber laser welding of zinc coated steels. In: *High power laser materials processing: lasers, beam delivery, diagnostics, and applications*

11. Zhang Z, Zhang L, Wen G (2019) Study of inner porosity detection for Al-Mg alloy in arc welding through on-line optical spectroscopy: correlation and feature reduction. *J Manuf Process* 39:79–92
12. Lacroix D, Jeandel G (1997) Spectroscopic characterization of laser-induced plasma created during welding with a pulsed Nd: YAG laser. *J Appl Phys* 81(10):6599–6606
13. Jin X, Fan J, Chow TWS (2019) Fault detection for rolling-element bearings using multivariate statistical process control methods. *IEEE Trans Instrum Meas* 68(9):3128–3136
14. Pedregosa F et al (2011) Scikit-learn: machine learning in python. *JMLR* 12:2825–2830
15. Johnson RA, Wichern DW (2008) *Applied multivariate statistical analysis*

Research on Laser DP-TIG Hybrid Thin Plate High-Speed Welding Process



Jialei Zhu, Cong Feng, Xiangdong Jiao, Zhibo Li, and Wei Li

Abstract Deep penetration TIG welding (DP-TIG) is a new efficient automatic welding method. Compared with traditional TIG welding, it can effectively increase welding penetration and improve welding efficiency. In thin plate welding, laser DP-TIG hybrid welding can significantly improve the welding speed on the premise of ensuring good weld formation. Taking the Q345B steel plate of 2 and 4 mm thickness as the base material, on the premise of ensuring the welding quality, this paper explores the maximum welding speed that can be achieved by laser DP-TIG hybrid welding under the conditions of hydrogenation of shielding gas, filler wire and different gaps and misalignment. The results show that the laser DP-TIG hybrid welding can significantly improve the welding speed and has good adaptability to the gap and misalignment. Adding a certain amount of hydrogen and filler wire in the experiment is beneficial to improve the weld formation and welding speed.

Keywords DP-TIG · Hybrid welding · High-speed welding

1 Introduction

Laser welding, as a kind of high energy beam welding, has the advantages of high welding speed, deep penetration, high degree of automation and small deformation. However, the welding method requires high assembly accuracy of workpiece [1–3]. In order to solve the problems of high cost and poor bridging of laser welding, W. M. Steen, a British scholar, first proposed the concept of laser arc hybrid welding in the

J. Zhu (✉) · C. Feng · X. Jiao · W. Li
School of Mechanical Engineering, Beijing Institute of Petrochemical Technology, 102617
Beijing, China
e-mail: zhujialei@bipt.edu.cn

C. Feng · W. Li
College of Electrical and Mechanical Engineering, Beijing University of Chemical Technology,
100029 Beijing, China

Z. Li
Tangshan Kaiyuan Welding Automation Technology Institute Co., Ltd., 063000 Tangshan, China

© Springer Nature Singapore Pte Ltd. 2020
S. Chen et al. (eds.), *Transactions on Intelligent Welding Manufacturing*,
Transactions on Intelligent Welding Manufacturing,
https://doi.org/10.1007/978-981-15-6922-7_5

Table 1 Chemical composition of Q345B mild steel and fill wire (wt%)

| Category | C | Si | Mn | P | S | V | Cr | Ni | Cu | Ti |
|----------|------|------|------|------|------|-------|------|------|-------|-----|
| Q345B | 0.09 | 0.35 | 1.65 | 0.03 | 0.03 | 0.15 | 0.2 | 0.45 | 0.28 | 0.1 |
| JM-68 | 0.09 | 0.77 | 1.61 | 0.01 | 0.01 | 0.004 | 0.06 | 0.06 | 0.025 | – |

early 1980s [4]. He combined two kinds of heat sources with completely different physical properties and energy transfer mechanisms, which not only gave full play to their advantages, but also made up for their disadvantages [5, 6].

The DP-TIG welding method realizes arc compression, improves energy density and increases welding penetration through high-speed cooling of tungsten electrode. Compared with TIG welding, this method has higher arc stiffness and higher energy density, which can realize the welding in the form of perforation and obtain a more stable single-sided welding and double-sided forming welding process [7].

In this paper, the laser DP-TIG hybrid method was used for welding experiments on 2 and 4 mm Q345B low carbon steel plates. By optimizing the welding parameters, the maximum welding speed of this method can be tested on the premise of good weld formation and no ultrasonic flaw detection defects. The arc shape and microstructure of the weld metal under the hybrid welding condition were studied as well. This is of great significance for the further study of this welding method and its application in industrial production.

2 Experimental Method

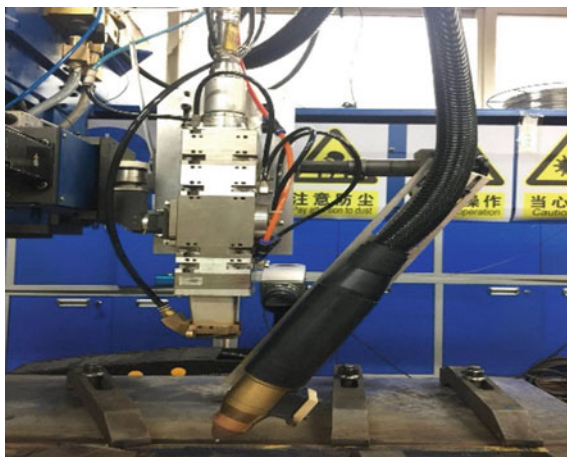
2.1 Experimental Materials

The test plate is Q345B low-alloy high-strength steel, with dimensions of 400 mm × 70 mm × 2 mm and 400 mm × 70 mm × 4 mm. The filler wire is jm-68 welding wire of Lincoln Jintai company, with a diameter of 1.2 mm. The chemical composition of test plate and filler wire are shown in Table 1.

2.2 Experimental Condition

The YLS-4000 fiber laser of IPG company was used in the experiment. The maximum laser power was 4 KW, and the focal length was 300 mm. It was mainly composed of laser welding head, control system, laser and water-cooling system. The DP-TIG welding machine is a Panasonic YC-500WX welding machine with a rated current of 500 A. It was connected to an external air feeding device and wire feeding device for integrated control. Using the DP-TIG welding torch independently developed by Tangshan Kaiyuan Group, the laser welding head and welding torch can adjust the

Fig. 1 Laser DP-TIG hybrid welding system



position and angle through the self-designed clamping device, as shown in Fig. 1. The multi-function CNC motion welding platform designed by Tangshan Kaiyuan Group can realize multi-axis composite motion, which can meet the various needs of laser arc hybrid welding, with convenient operation and high running accuracy.

Adopt the welding method of plate self-fusion welding and plate butt welding. Before welding, remove the oxide film on the surface of the workpiece and clean it with acetone to remove oil. Two composite welding processes are adopted: hydrogenation and non-hydrogenation. The former is a mixed gas of 95% argon and 5% hydrogen, while the latter is pure argon with a flow rate of 15 L/min. During the experiment, the defocus amount and the distance between the heat sources were both 0 mm. The forward wire feeding method and welding direction with laser in front and arc in back were used.

3 Experimental Results and Discussion

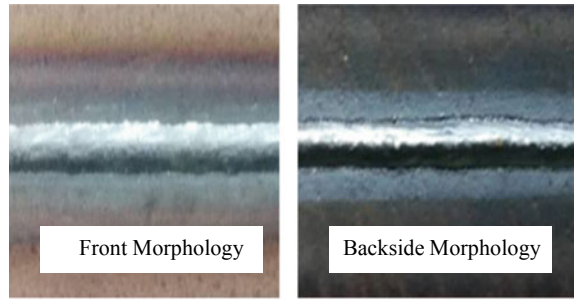
3.1 Research on 2 mm Test Plate Process

3.1.1 Pure Argon Shielding Gas

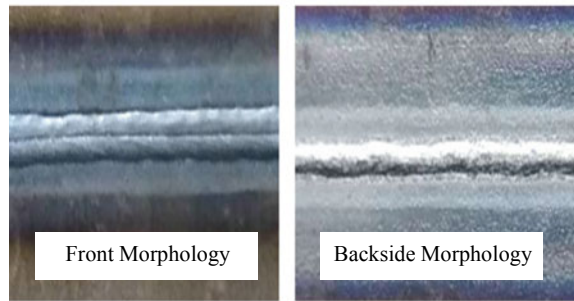
By adjusting the laser power and welding current, the plate self-fusion welding and plate butt welding were carried out. On the premise of ensuring the welding quality, the welding speed was gradually increased. In order to improve the quality of weld formation, a front wire feeding device was used in several groups of experiments to fill the wire. Several typical experimental results are shown in Fig. 2.

It can be seen from the experimental results that in the process of plate self-fusion welding, by adjusting the laser power and welding current, the welding speed can

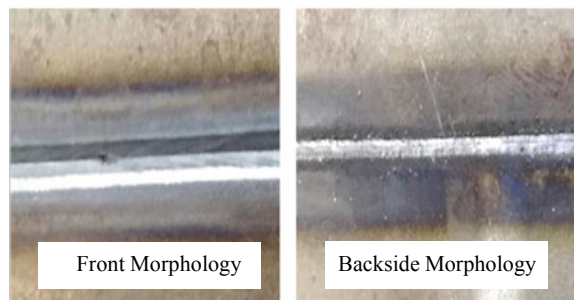
Fig. 2 Weld morphology of 2 mm thick and low carbon steel plate



(a) Plate self-fusion welding, $P=2500W$ $I=200A$
 $V=2.5m/min$, Forward wire feeding



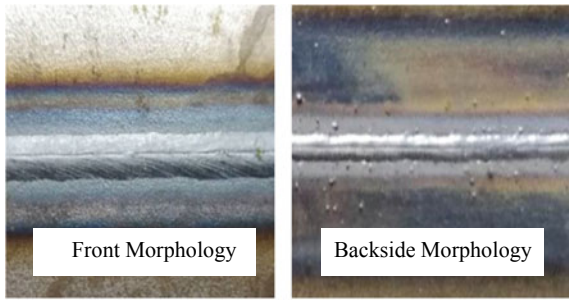
(b) Plate self-fusion welding, $P=2500W$ $I=200A$
 $V=3m/min$, No wire feeding



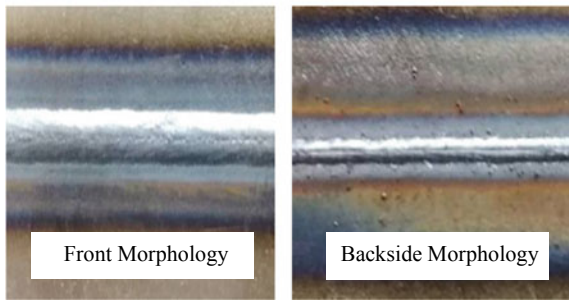
(c) Plate butt welding, $P=2500W$ $I=150A$
 $V=2.5m/min$, Forward wire feeding

reach 3 m/min on the premise of ensuring good weld formation while the speed of plate butt welding can reach 2.5 m/min. The addition of welding wire can improve the weld surface formation, but has no obvious effect on increasing the penetration and welding speed.

Fig. 3 Weld morphology of 2 mm thick and low carbon steel plate under hydrogen



(a) Plate self-fusion welding, P=3500W I=200A V=3.5m/min, Forward wire feeding



(b) Plate self-fusion welding, P=3500W I=200A V=4m/min, Forward wire feeding

3.1.2 Shielding Gas of 95% Argon and 5% Hydrogen Mixed Gas

Pass 5% active gas hydrogen gas into the protective gas and adjust the welding parameters to carry out the experiment. On the premise of ensuring good weld formation, the welding speed was gradually increased. Several groups of typical experimental results are shown in Fig. 3.

From the experimental process and results, it can be seen that in the process of plate self-fusion welding, passing a certain amount of hydrogen gas into the shielding gas can improve the melt pool fluidity and the weld formation. Moreover, the welding speed can be increased to 4 m/min. However, in the process of plate butt welding, shielding gas has little effect on welding speed.

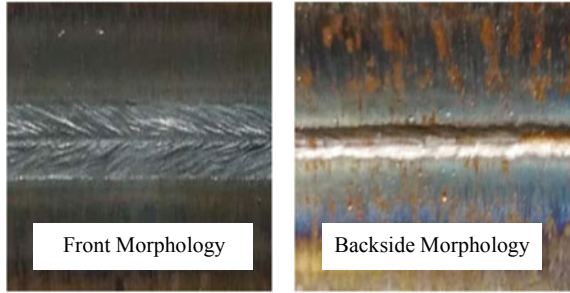
3.2 Research on 4 mm Test Plate Process

Taking 4 mm thick low carbon steel plate as the object, using hydrogen gas mixture as the shielding gas, using the wire filling method of front wire feeding, through

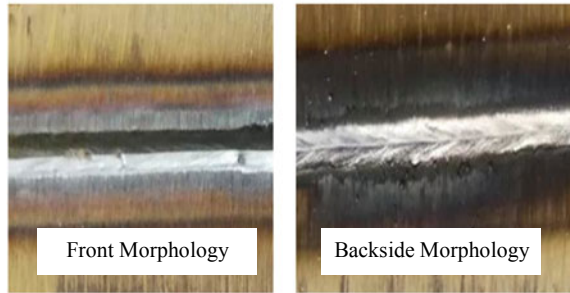
adjusting the welding parameters, the experiments of plate self-fusion welding and plate butt welding were carried out. On the premise of good weld formation, the welding speed was gradually increased. Several typical experimental results are shown in Fig. 4.

It can be seen from the experimental results that the welding speed can be up to 2 m/min for plate self-fusion welding and 1.5 m/min for plate butt welding. The

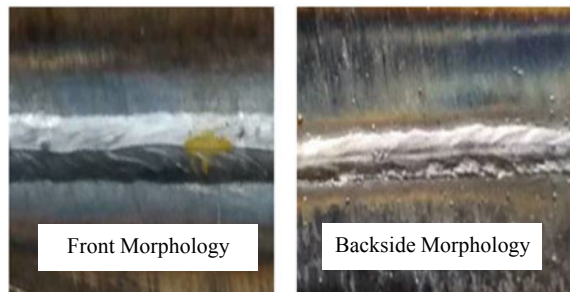
Fig. 4 Weld morphology of 4 mm thick and low carbon steel plate



(a) Plate butt welding, P=4000W I=150A V=1.5m/min, Forward wire feeding



(b) Plate butt welding, P=4000W I=150A V=1.5m/min, 0.5mm gap 1mm misalignment Forward wire feeding



(c) Plate self-fusion welding, P=4000W I=150A V=2m/min, Forward wire feeding

welding process has good adaptability to gap and misalignment. The value of gap depends on the laser spot diameter. The maximum value is 0.5 mm, and the single misalignment can reach 1 mm.

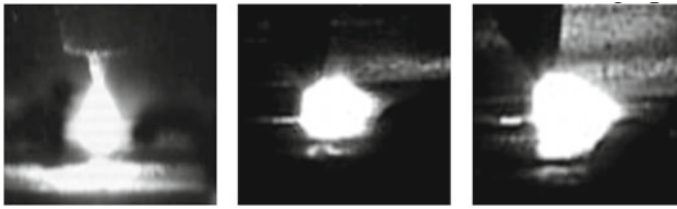
3.3 Arc Shape Observation

In laser DP-TIG hybrid thin plate high-speed welding, the laser power decides the penetration, and the welding current plays the role of improving the weld formation and increasing the weld width. Therefore, on the premise of ensuring laser penetration, the welding current plays a major role in improving the welding speed. Several experiments under the condition of 2 mm plate thickness were filmed with high-speed camera to observe the influence of welding parameters on arc shape.

It can be seen from Fig. 5 that the laser has an attracting effect on the arc, and the hybrid arc is offset to the direction of the laser beam. The arc burns most intensely at the focus of the laser. In high-speed welding, this kind of attractive effect can better control the direction of the arc and improve the weld formation. In the process of hybrid welding, the welding current and laser power have an optimal matching parameter. From Fig. 4c and d, it can be seen that when the welding power is 2500 W and the welding current is 200 A, the arc stiffness and directivity are the best, and the effect of improving the weld formation and welding speed is the best. It can be seen from the Fig. 4d that when the current is too large, although the laser attraction to the arc still exists, the arc diverges at this time and the stability is poor. In addition, too much plasma produced by high current dilutes the laser energy, reduces the penetration, and the back cannot be formed when the welding speed is too fast.

3.4 Weld Microstructure

The metallographic specimen was prepared by selecting the welding specimen at the welding speed of 1.5 m/min, and the microstructure of the welded joint was observed by metallographic microscope. Figure 5 shows the microstructure of the hybrid welded joint. The base material in Fig. 6a is mainly composed of pearlite and ferrite. The pearlite grains are located between the ferrite grains, and the grains are small; in Fig. 6b, the heat-affected zone consists of coarse-grained zone and fine-grained zone, which are mainly composed of martensite and bainite. Coarse-grained zone has high phase transition temperature, fast cooling speed and high hardness. The cooling speed of fine-grained zone is slower than that of coarse-grained zone which results in grain refinement. Therefore, the comprehensive performance of fine-grained zone is better than that of coarse-grained zone; Fig. 6c shows the central area of the hybrid weld, in which the white phase is the eutectoid acicular ferrite. The eutectoid ferrite grows in the form of columnar crystals, which is perpendicular to the fusion line and points to the midline of the weld. The rest of the structure is

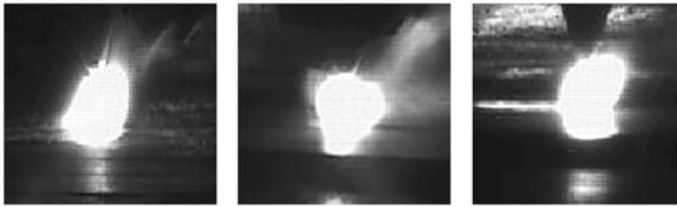


V=1.5m/min

V=2.5m/min

V=3.5m/min

(a) I=150A

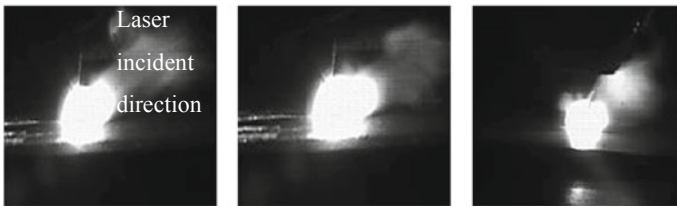


V=1.5m/min

V=2.5m/min

V=3.5m/min

(b) P=2000W I=150A



V=1.5m/min

V=2.5m/min

V=3.5m/min

(c) P=2500W I=200A



V=1.5m/min

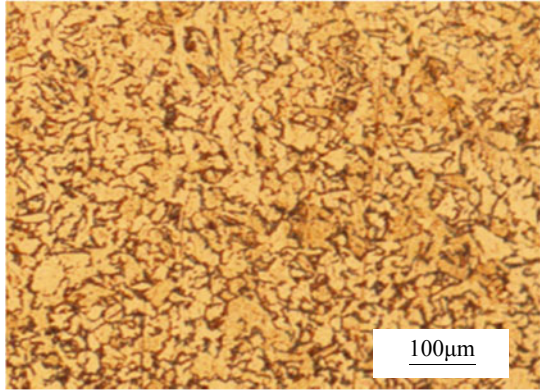
V=2.5m/min

V=3.5m/min

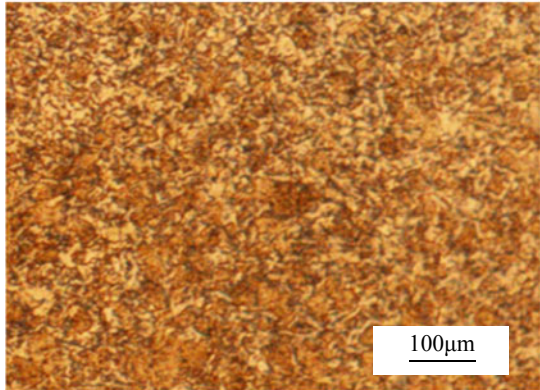
(d) P=2500W I=300A

Fig. 5 Arc shape of welding speed under different welding current

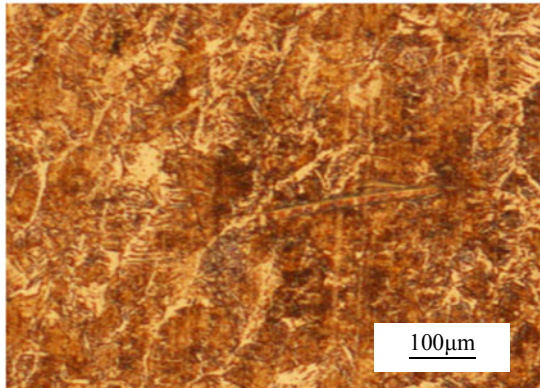
Fig. 6 Microstructure of hybrid weld joint



(a) Base material



(b) Heat affected zone



(c) Central area of hybrid weld

mainly granular bainite and a small amount of martensite. The grains are fine and uniform, and the comprehensive mechanical properties are good.

4 Conclusion

1. Laser DP-TIG hybrid welding can significantly improve the welding speed of thin plate welding on the premise of ensuring the good formation of the weld and has good adaptability to the gap and misalignment.
2. Using hydrogen gas and filler wire in hybrid welding can improve weld formation and welding speed, but the adjustment of wire feeder is complex.
3. In hybrid welding, the welding current and laser power have a certain matching range. The best matching parameters of 2 mm thick plate are about 2500 W laser power and 200 A welding current; The best matching parameters for 4 mm thick plates are about 4000 W laser power and 200 A welding current. If the current is too small, the weld formation is poor, and if the current is too large, the laser will be diluted to reduce the penetration. In high-speed welding, laser power plays an important role in penetration, and welding current is mainly used to improve weld formation and increase weld width.
4. The microstructure of the hybrid weld is mainly bainite and martensite, with fine grains and directionality.

References

1. Xu G, Ying Z, Hang Z, Zhong L, Wu B, Liu X (2016) CO₂ laser-MAG hybrid welding properties of high strength steel. *Trans China Weld Inst* 37(07):17–21
2. Chen M, Li CB, Liu L (2014) Coupling behavior of plasma in laser-arc hybrid welding. *Trans China Weld Inst* 35(10):53–56+115
3. Jiang Y, Yang S, Wang Y, Yang Z (2016) Research status of laser-arc hybrid welding technology. *Weld Technol* 45(03):1–4
4. Steen WM (1980) Arc augmented laser processing of materials. *J Appl Phys* 51(11):5636–5641
5. Xiao R, Wu S (2008) Progress in laser-arc hybrid welding. *China Laser* 35(11):1680–1685
6. Lu T, Wenyi G (2005) Laser arc hybrid welding—a new welding method. *Locomo Roll Stock process* (02):5–7+10
7. Liu Z, Qu H, Cao R, Sun W (2017) DP-TIG welding process research. *Welding* (03):61–65+76

Influence of Welding Sequence on Welding Deformation of T-Joint



Yong Qin, Ziquan Jiao, Zhiqiang Feng, Nanhui Shi, Junfeng Han, and Xian Wei

Abstract Aiming at carbon dioxide gas shielded welding of T-groove of low carbon steel sheets in ship compartments, three practical welding processes were simulated by welding software Simufact Welding, and the effect of welding sequence on welding deformation was studied. The results show that the final deformation of cross-back-welding and simultaneous back-welding is smaller, while the process requirements of cross-back-welding are lower, which is most in line with the actual production requirements.

Keywords Simufact welding · CO₂ gas shielded welding · Cross-back-welding · Welding deformation

1 Introduction

Effective control of welding deformation is one of the key factors affecting the welding quality and production efficiency of components, and different welding methods, base metal properties, plate size, welding speed, welding sequence and thermal input have different effects on welding deformation.

This thesis mainly researches the cabin cubicle; its main function is to separate the space. Most of the plates are thick, and the joint form is T-joint without groove. At the same time, due to the large thickness of the base metal, the heat transfer is slow during welding, and the difference between the heat of the welded surface and the unwelded surface is large, which is easy to cause the angular deformation. Compared with the deformation correction of thin plate, the correction of thick plate is easier, but it will still increase the construction cost and prolong the construction period. Therefore, it is very important to choose a reasonable welding sequence [1].

Y. Qin

Guilin University of Electronic Technology, School of Mechanical and Electrical Engineering, 541004 Guilin, China

Y. Qin · Z. Jiao · Z. Feng (✉) · N. Shi · J. Han · X. Wei

Beibu Gulf University, College of Mechanical and Marine Engineering, 535011 QinZhou, China
e-mail: fzqsjtu@163.com

In this paper, the welding process is simulated by the professional welding software Simufact Welding 8.0, and the influence of welding sequence on the welding deformation of T-joint between cabin grids is studied. It provides relevant technical basis for accurate prediction of welding deformation of ship structure.

2 Establishment of Welding Model

2.1 Structural Model

In this study, the bottom bulkhead of the hull cabin is taken as the research object, and the SolidWorks software is used for modeling, which is composed of the bottom slab and eight bulkheads of the same size [2]. The actual size is shown in Fig. 1, the size of base plate is 6400 mm \times 6000 mm \times 20 mm, and the size of diaphragm is 400 mm \times 6000 mm \times 12 mm. Because the size of the original model is too large, in order to facilitate the mesh division and the subsequent simulation test, the model is simplified according to the symmetry, and only a combined model of diaphragm and base plate is studied. Because this paper is the fillet weld of T-joint without groove, the thickness of the welded plate is kept unchanged, the length and width of the plate are reduced proportionally, and the simplified model size is shown in Fig. 2. The base plate size is set as 300 mm \times 800 mm \times 20 mm, and the vertical plate is set as 60 mm \times 800 mm \times 12 mm.



Fig. 1 Original geometric model

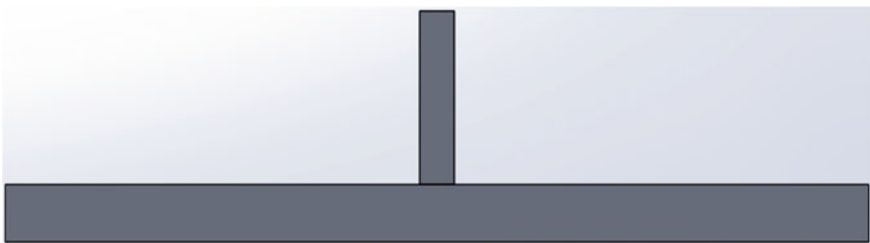


Fig. 2 Simplified geometric model of fillet welding

2.2 Technique Plan

The material used in the experiment is S355J2G3, which is a common low-alloy structural steel for ships. Its welding process can be regarded as a nonlinear transient heat transfer process with centralized input of heat source. During the welding process, the parameters such as heat transfer coefficient, thermal conductivity and specific heat capacity will change with the change of temperature and tend to be constant at a certain temperature, meeting the control equation of nonlinear transient heat transfer problem. It can be expressed as [3]:

$$\rho c \frac{\partial T}{\partial t} = \frac{\partial}{\partial x} \left(\lambda \frac{\partial T}{\partial x} \right) + \frac{\partial}{\partial y} \left(\lambda \frac{\partial T}{\partial y} \right) + \frac{\partial}{\partial z} \left(\lambda \frac{\partial T}{\partial z} \right) + Q_n \tag{1}$$

where ρ is the density of the material; c is the specific heat capacity of the material; λ is the thermal conductivity of the material; T is the instantaneous temperature of the material; Q_n is the heat generated inside the object.

The chemical composition and parameters of S355J2G3 low-carbon steel change with temperature as shown in Tables 1 and 2 [4, 5].

In the actual welding process, for the workpiece with a long weld, it is often used to control the welding deformation and other welding defects by means of sectional step back-welding, leap welding and other processes [6]. For example, the step back-welding process is to specify a large welding direction after a long workpiece is segmented, and the welding direction of each small section is opposite to the large direction. Step skip welding is the welding of each small segment along the general direction of welding, while welding is not carried out in accordance with the sequence, as shown in Fig. 3. These two technologies can effectively control the welding deformation and improve the welding efficiency.

Table 1 Chemical composition of low-carbon steel

| Element | C | Si | Mn | P | S | Nb | V | Ti | Cr | Ni | Cu | N | Mo |
|-----------------|-----|-----|-----|-------|-------|------|------|-----|-----|-----|-----|-------|-----|
| Content max (%) | 0.2 | 0.5 | 1.7 | 0.035 | 0.035 | 0.07 | 0.15 | 0.2 | 0.3 | 0.5 | 0.3 | 0.012 | 0.1 |

Table 2 Material property parameters of low-carbon steel changing with temperature

| Temperature T (°C) | 20 | 200 | 400 | 600 | 800 | 1000 | 1300 | 1842 | 2227 |
|--|-------|-------|-------|-------|--------|-------|-------|-------|-------|
| Density P (kg/m ³) | 7820 | 7740 | 7710 | 7650 | 7620 | 7580 | 7500 | 7200 | 7200 |
| Specific heat capacity c (J/kg · °C) | 460.0 | 491.7 | 557.8 | 667.1 | 1108.0 | 626.4 | 637.9 | 645.5 | 645.5 |
| Thermal conductivity λ (J/m · s · °C) | 50.0 | 51.1 | 44.4 | 39.4 | 31.8 | 26.4 | 29.7 | 105 | 105 |
| Heat transfer hc (J/m ² · s · °C) | 1.00 | 1.50 | 1.70 | 1.86 | 1.98 | 2.09 | 2.22 | 2.29 | 2.32 |

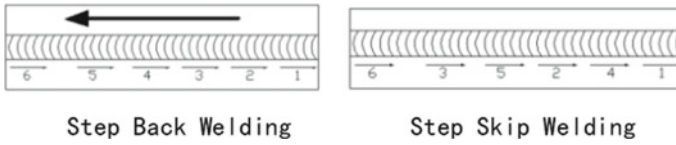


Fig. 3 Step back-welding and step skip welding

In fillet welding of structural parts with large thickness and no bearing force, the welding process without groove and without penetration is often adopted. Therefore, the welding joint of this paper is the fillet weld of T-joint without groove. Three schemes are adopted to study the welding deformation law.

As shown in Fig. 4, the following scheme is adopted to study the welding deformation law, and the numbers in the figure are the welding sequence.

In scheme 1, adopting step cross-back-welding, the welding direction of each section is opposite to the general welding direction, and the process of left and right cross-welding is adopted.

The second option is the process of no cross-sectional welding. The welding direction of each section is opposite to the general welding direction, but the welding is carried out from left to right.

In scheme 3, the welding shall be carried out in sections at the same time. There is no long cooling time between each welding process of the three schemes, and the same cooling is carried out after the final welding of all cooling.

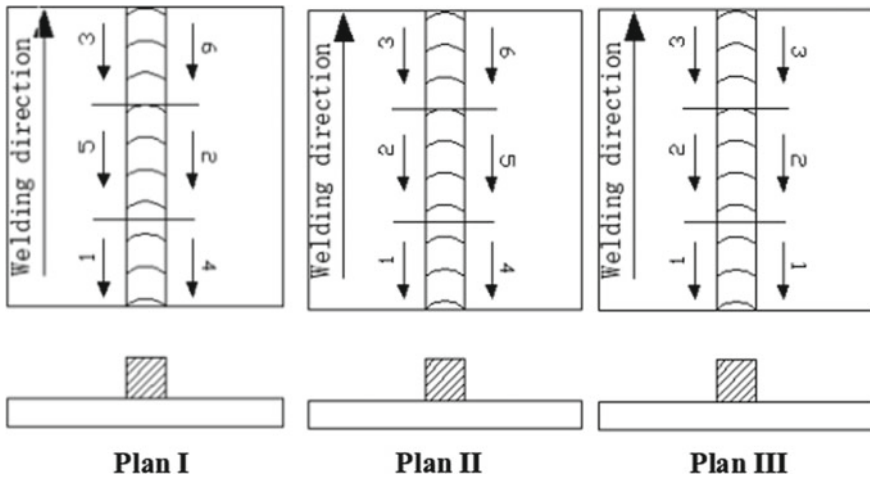


Fig. 4 Welding process plan

3 FEM Analysis Model

3.1 Heat Source Model

There are many kinds of welding heat source models. Different heat source models are selected according to different welding structures, material specifications, plate thickness and welding methods. At present, the best choice is ellipse heat source model, double-ellipse heat source model and Gauss heat source model. According to the symmetry of the welding seam, the key points can only be selected from half of the base metal. Using double-ellipse model to load heat source can better carry out numerical simulation, and the simulation results are closer to the measured results [7].

Goldark’s double-ellipse heat source model overcomes the shortcomings of different heat source gradients in the front and rear hemispheres of the ellipse heat source model, that is, the temperature gradients in the first half of the ellipse heat source model are not as steep as the actual temperature gradients, and the temperature gradients in the second half are relatively slow [8]. The double-ellipse heat source model is shown in Fig. 5.

The first half of the double-ellipse heat source model is a one-fourth ellipsoid model, and the second half is another one-fourth ellipsoid model. Then, the heat source model distribution expression of the first half ellipsoid is:

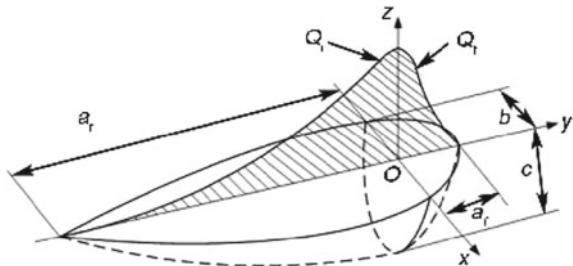
$$q(r) = \frac{6\sqrt{3}f_1Q}{\pi^{3/2}a_rbc} \exp\left\{-3\left[\left(\frac{x}{a_r}\right)^2 + \left(\frac{y}{b}\right)^2 + \left(\frac{z}{c}\right)^2\right]\right\} \quad (2)$$

The distribution expression of heat source model for the second half ellipsoid is:

$$q(r) = \frac{6\sqrt{3}f_2Q}{\pi^{3/2}a_fbc} \exp\left\{-3\left[\left(\frac{x}{a_f}\right)^2 + \left(\frac{y}{b}\right)^2 + \left(\frac{z}{c}\right)^2\right]\right\} \quad (3)$$

where f_1 and f_2 are the distribution functions of heat flux density, respectively, and $f_1 + f_2 = 2$; Q is the input heat source power and $Q = \eta UI$; at the same time,

Fig. 5 Double-ellipse heat source model



a_r , a_f , b and c are the parameters of defining ellipse, which have no influence on each other and can take different values.

In this paper, the simulation is based on Simufact Welding 8.0 software, which only needs to be based on the size of the weld pool and the actual welding process. In addition, the simulated heat source model needs to wrap 3–5 grids in each direction of the weld area to simulate accurately. Therefore, the numerical selection of A, B and C can be made according to the size of the weld pool obtained in the ideal state by using the backward method.

3.2 Parameter Configuration and Analysis Calculation

As shown in Fig. 6, the weldment is divided into weld zone, near weld zone and base metal zone according to the effect of welding heat on base metal. In order to facilitate the calculation, the grid size of the weld area is set to 2 mm, and the near weld area and the base metal area are combined. The grid is divided by dense and sparse grid, so as to minimize the number of grid. The number of final volume grid cells is 168,000, and the number of nodes is 201,000.

This thesis mainly researches the actual welding process of CO₂ gas shielded welding at room temperature 20 °C is simulated. According to the welding process and the thickness and size of the plate, the welding current and voltage are set as 360 A and 35 V, the thermal efficiency is 0.8. The parameters of the Gaussian double-ellipse heat source model are set, the front section is 5 mm, the back end is 15 mm long, the width is 9 mm, the depth is 12 mm, and the parameters of the Gaussian heat source are 3. As shown in Fig. 7, the weld adopts triangle shape, which is automatically generated by the software. “ a ” refers to the depth of weld and the height of the triangle, “ b ” refers to the reinforcement and can be raised or concave, Z_1 and Z_2 refer to the weld fillet size, $Z_1 = Z_2$ is set as 5 mm, $b = 0$ mm, and “ a ” dimension is automatically generated as 3.53553 mm. Figure 8 shows the automatically generated weld shape.

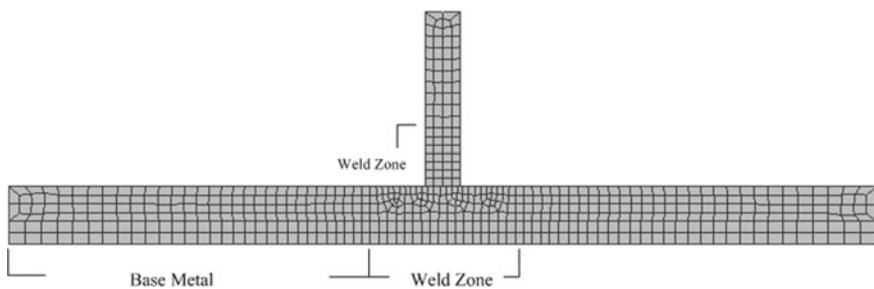


Fig. 6 Mesh generation plan

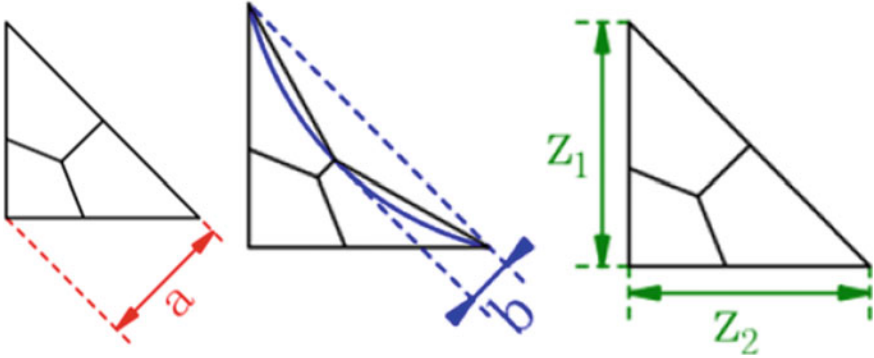
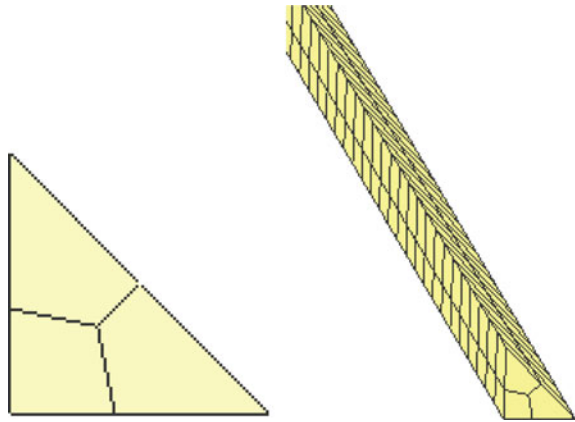


Fig. 7 Weld size definition

Fig. 8 Geometric model of weld



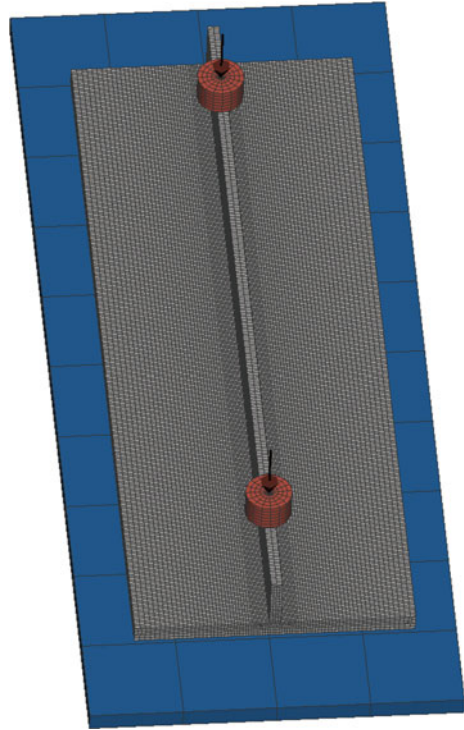
As shown in Fig. 9, boundary conditions are defined. One base plate located on four corners was four clamping devices; Q345 steel, S355J2G3, corresponding to the software, were selected as the base material, weld material and welding wire material. In particular, this simulation does not prevent rigid fixation at the four corners of the bottom plate, which is to study the state of the bottom plate warping after welding to a greater extent.

4 Analysis of Simulation Results

4.1 Result Analysis of Scheme 1

Observe the simulation results under the condition of three times magnification, as shown in Fig. 10 is the deformation of base metal after the first three sections of

Fig. 9 Define boundary conditions



welding. The diaphragm is distorted. Because in the process of segmented back-welding, there is a large gap between the two sides of the baffle plate. As shown in Fig. 11, after the completion of the six-section welding, the distortion of the diaphragm basically recovers, and there is no obvious distortion under three times magnification. In scheme 1, before the welding is finished and the cooling and heat release step is started, the cross section along the z-axis is magnified by three times, and it can be seen that there are different degrees of deformation on the y-axis and x-axis. Among them, both ends of the bottom plate are obviously raised.

With the increase of cooling time, the deformation of the four corners of the bottom plate decreases as the base metal temperature approaches to room temperature. As shown in Figs. 12 and 13, they are the deformation of the bottom plate when cooling for 8 min and 15 min, respectively. The deformation trend gradually spreads to the two points (upper left corner) at the end of the weld, and the deformation at both ends of the first end of the weld gradually decreases. According to the actual welding process, the thicker the base metal, the longer the cooling time to room temperature. The maximum deformation position of the final base metal is at the end of the last welding section.

Fig. 10 Front three sections of diaphragm are twisted and deformed after welding

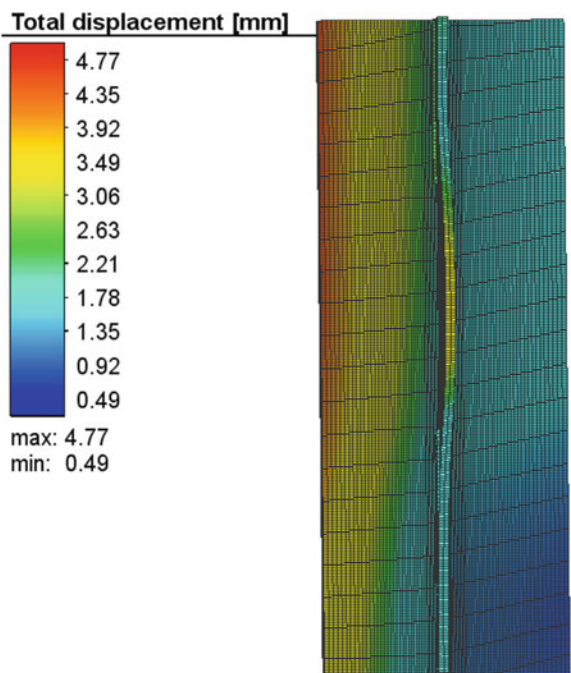


Fig. 11 Baffle plate is twisted and deformed after welding

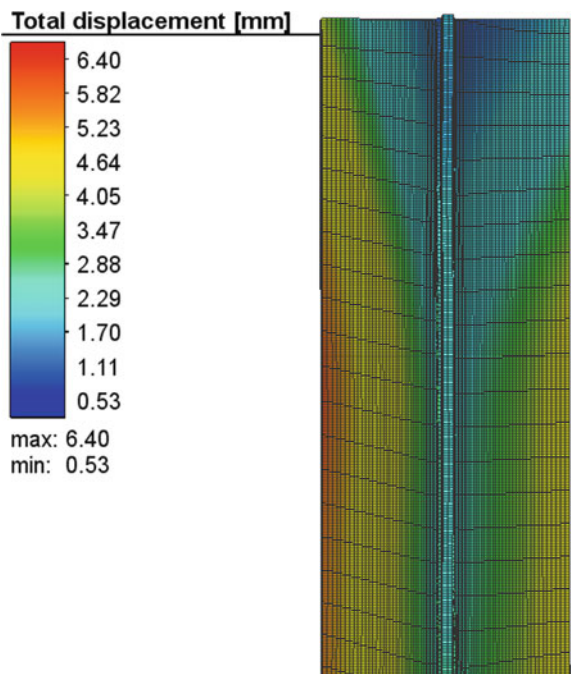


Fig. 12 Diagram of deformation after cooling for 8 min

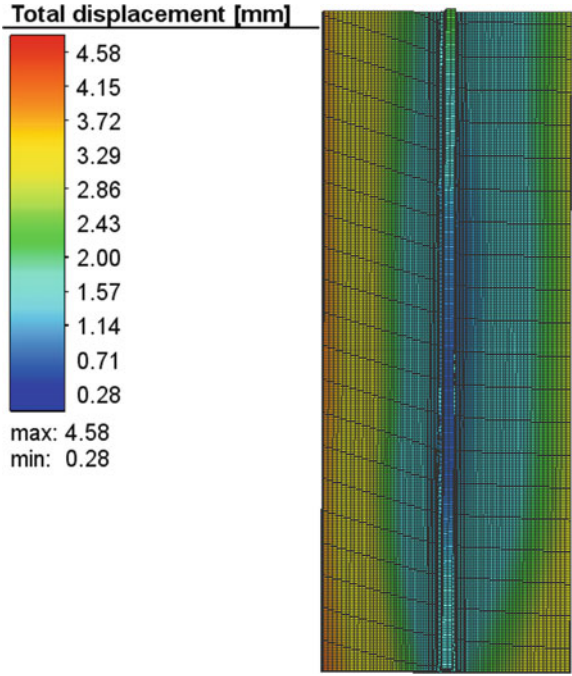
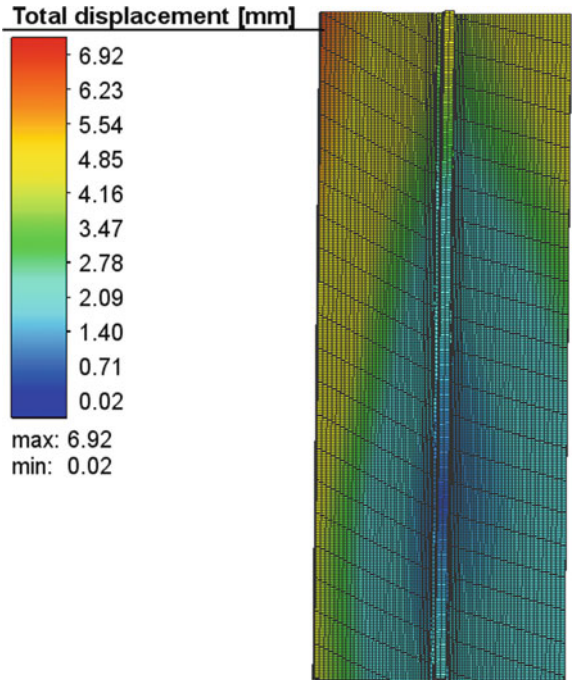


Fig. 13 Diagram of deformation after cooling for 15 min



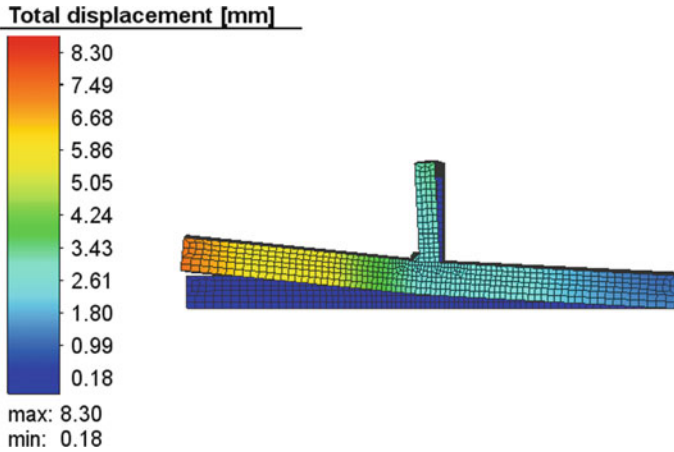


Fig. 14 Angular distortion of the first three sections after welding

4.2 Result Analysis of Scheme 2

Observe the simulation results under the condition of three times magnification, as shown in Fig. 14 is the deformation of base metal after the first three sections of welding are completed. The distortion of the diaphragm is small, but the angle between the base plate and the diaphragm is serious. Because the first three sections of welding only act on the same side, the temperature distribution in the thickness direction of the plate is uneven, the welding side has a large thermal expansion, and the expansion on the other side is small, which leads to the expansion of the welding side being hindered and serious transverse compression deformation. As shown in Fig. 15, the deformation state at the end of all welding is shown. The right bottom plate has a small up-warping, the partition plate returns to a vertical state, and the angular deformation is small. Because the welding temperature on the left side is too high, it is equivalent to preheating the welding on the right side, so that the temperature difference on the right side is low and the deformation is small.

With the increase of cooling time, when the temperature of base metal approaches to room temperature, the elastic deformation and plastic deformation in the base metal tend to be stable, and the overall deformation does not change much. As shown in Fig. 16, the deformation state after final cooling. Serious angular deformation occurs on the right side, large floor warping, no obvious left floor warping, small deformation.

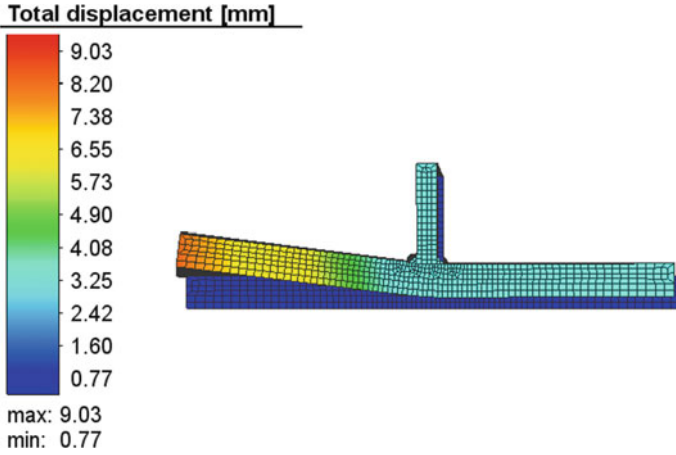
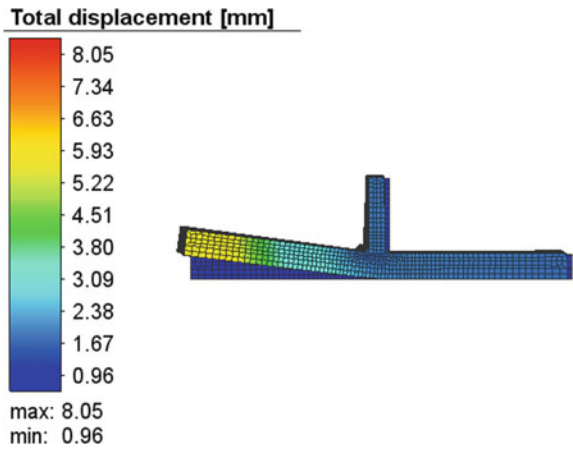


Fig. 15 Angular distortion after welding

Fig. 16 Schematic diagram after cooling



4.3 Result Analysis of Scheme 3

As shown in Fig. 17, the welding process flowchart of scheme 3, the change and migration rule of deformation can be seen. The deformation at both ends of the base plate is the largest, and the maximum deformation also changes with the moving direction of the welding. As shown in Figs. 18 and 19, the total deformation of cooling for 8 min and cooling for 15 min respectively. At this time, the temperature of the base metal is close to room temperature, and the elastic deformation in the base metal is gradually reduced, and the deformation is stable.

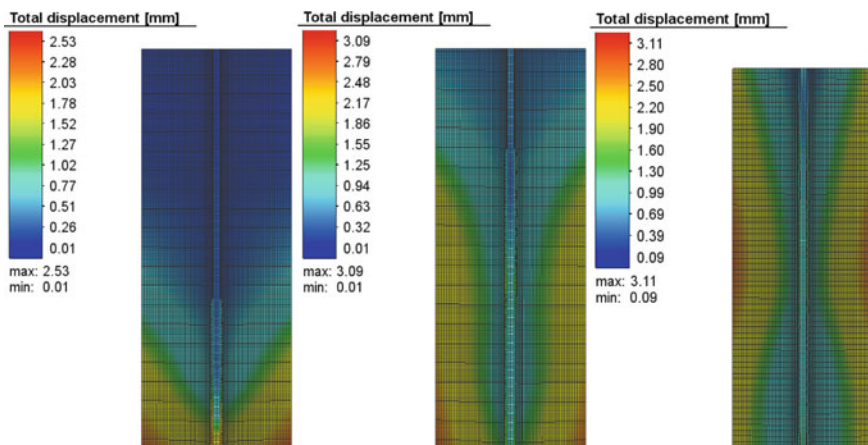


Fig. 17 Welding process deformation flowchart

Fig. 18 Diagram of deformation after cooling for 8 min

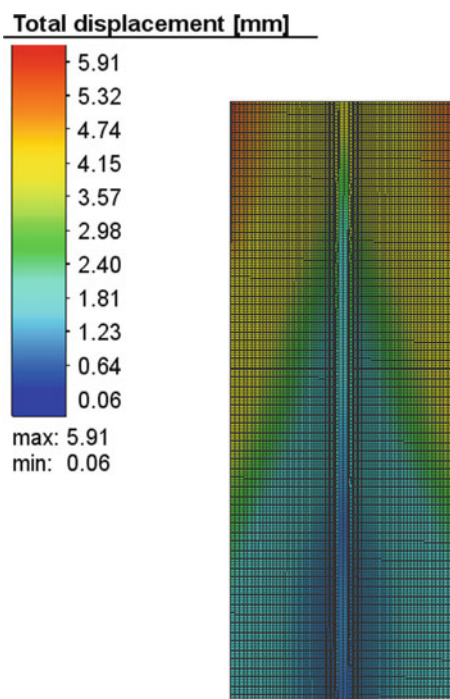
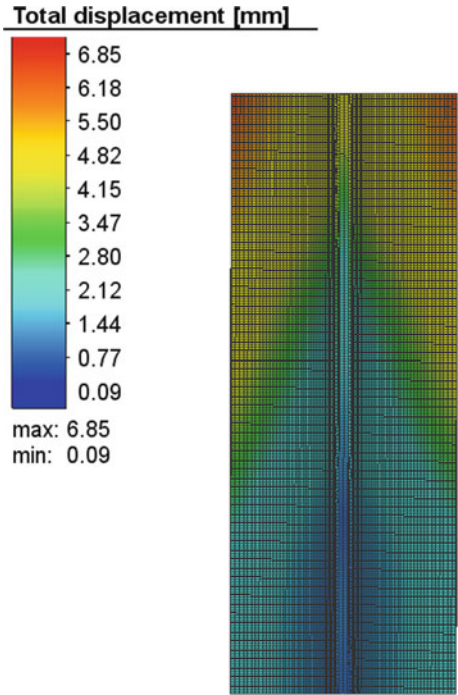


Fig. 19 Diagram of deformation after cooling for 15 min



5 Conclusion

According to the analysis of the experimental results of the numerical simulation of the welding process of three schemes, it is found that the selection of welding sequence has a very obvious effect on the deformation. In the actual welding process, for the T-joint fillet welding process, the most appropriate welding process should be cross-welding or symmetrical welding, and the deformation of the plate after welding is small. However, the welding process of scheme 2 will have a large deformation effect.

For the actual production process, in consideration of cost saving and human and material resources, the welding process of cross-back-welding is more used. In addition, the deformation gap between the two ends of the bottom plate in scheme II is large. Considering the factors, compression clamps can be applied on the left and right sides of the bottom plate, or fixed clamps with large pressure can be applied on the left side, i.e., the welding side first, so that the deformation gap between the left and right ends is small.

References

1. Wang JC, Yi B, Zhou H (2019) Prediction and control of welding induced buckling in reinforced thin plate ship structure. *Naval Arch Ocean Eng* 35(01):58–63
2. Zhao DS, Miao TJ, Wu LL, Liu YJ (2019) Experimental parameter design and calculation of welding deformation correction by flame straightening. *Lab Sci* 22(03):20–23
3. Zhang WY (1989) Theory of welding heat conductance. China Machine Press, Beijing, pp 1–6
4. Zhang X, Qu HY (2015) Simulation of local model multi-pass welding simulation based on SYSWELD. *J Hebei United Univ* 37(04):27–33 (Natural Science)
5. Zhao KL (2009) Study on simulation of welding deformation of hull blocks based on FEA. Harbin Engineering University
6. Ying CC (2013) Shipping technology. Shanghai: Shanghai Jiao Tong University press, pp 403–404
7. Mo LC, Qian BN, Guo XM, Yu SF (2001) The development of models about welding heat sources calculation. *Weld J* (03):93–96+101
8. John G (1984) A new finite model for welding heat source. *Metall Trans* 15B(2):299–305

Short Papers and Technical Notes

Research on Machine Vision Image Mosaic Algorithm for Multi-workpiece Cutting Platform



Long Xue, Yingyu Cao, Junfen Huang, Jiqiang Huang, Zhengyu Zhang, Lanlan Bai, and Jianting Xi

Abstract The cutter head parts of the tunnel boring machine (TBM) are of different sizes, and the cutting platform is of large size. The panoramic view of the cutting platform that meets the accuracy requirements through image stitching is a prerequisite for realizing the visual guidance of autonomous cutting. An image stitching algorithm is studied to reduce the complexity of the algorithm on the basis of ensuring the stitching precision. The ORB algorithm is selected to implement feature detection, and a series of strategies are adopted on this basis. The ROI region is extracted, and only the images in the region of interest are matched. Then, the feature detection, description and matching are performed by the ORB feature detection algorithm and Hamming distance. The feature points are purified by the RANSAC algorithm, and the transformation matrix H is calculated. Finally, the image fusion is carried out. The experimental results show that the ROI-based ORB image stitching algorithm satisfies the accuracy requirements of subsequent visual guidance.

Keywords Machine vision · Image stitching · ORB algorithm

1 Introduction

The groove processing of cutter head parts of shield machine belongs to the typical small batch discretization mode [1]. The structure of this parts is complex and diverse, and the forms of groove are also different. At present, manual groove and semi-automatic groove are the main two forms [2], which means the quality of groove depends on the proficiency of the workers, and always the production efficiency is very low. Therefore, it is urgent to develop an automatic groove cutting system for the cutter head parts of the robot shield machine, so that the workers can place the workpiece to be cut on the robot working platform at will, and the robot will sense

L. Xue · Y. Cao (✉) · J. Huang · J. Huang · Z. Zhang · L. Bai · J. Xi
School of Mechanical Engineering, Beijing Institute of Petrochemical Technology, Beijing
102617, China
e-mail: caoyingyu@bipt.edu.cn

© Springer Nature Singapore Pte Ltd. 2020
S. Chen et al. (eds.), *Transactions on Intelligent Welding Manufacturing*,
Transactions on Intelligent Welding Manufacturing,
https://doi.org/10.1007/978-981-15-6922-7_7

the workpiece position and plan the cutting path independently, so as to improve the production efficiency and groove processing accuracy.

Robots usually work in the static and structured environment, that is, to keep their position fixed and to complete tasks by running programs written offline in advance [3]. However, in the autonomous cutting system, robots need to meet the requirements of autonomous planning: Autonomous planning means that robots can realize intelligent perception of the external environment, identify, locate the workpiece and plan the path [4]. Now, visual guidance is a more mainstream way of perceiving the environment, which uses two-dimensional or three-dimensional camera to obtain the working environment image to realize the environmental perception. Because the size of cutter head parts of shield machine varies, the smallest one is tens of centimeters, the largest one will be five or six meters, so it is difficult to use a single camera to obtain a panorama of cutting work with required accuracy. Moreover, because the camera needs to be mounted on the mobile mechanism, the acquired image will be deformed due to mechanical jitter. Therefore, it is a prerequisite for independent planning of visual guidance to generate panorama of cutting platform with required accuracy through image splicing algorithm.

In this paper, oriented fast and rotated brief (ORB) algorithm is proposed to splice panoramic images of cutting platform. ORB algorithm is a matching algorithm proposed by Roblee E et al. in 2011 by the IEEE International Conference on compute vision. Its operation speed is greatly improved compared with scale-invariant feature transform (SIFT) and speed-up robot features (SUFT). It is suitable for the industrial environment with high requirements for splicing time and accuracy. Based on the original algorithm, the matching is limited to region of interest (ROI), which reduces the occurrence of matching time and mismatch.

2 ORB Image Mosaic Based on ROI

The experiment was carried out under the condition of workshop. The shoot target of the experiment was a 600 mm × 800 mm working platform. Da Heng GT2450 camera and Computer M0824-MPW2 industrial lens were used. The computer configuration was Intel I5 590 processor with 8G RAM. The algorithm compiling environment was Visual Studio 2015, and OpenCV image processing algorithm library was called. The camera was about 400 mm away from the workpiece, and the shooting field size was 232.7 mm × 172.9 mm. The camera was installed on the six-axis flange of KUKA mechanical arm. The camera moved in one direction to shoot, and the camera position was adjusted to ensure that the coincidence area between the two adjacent images was about 60%.

ORB is a kind of local invariant feature descriptors, which has certain scale invariance to matrix transformation of image such as translation, rotation and scaling. The algorithm flowchart is shown in Fig. 1. The core idea of the algorithm is to use the improved FAST (oriented FAST) algorithm to detect corner points on the image pyramid and generate the main direction, so that the feature points have certain scale

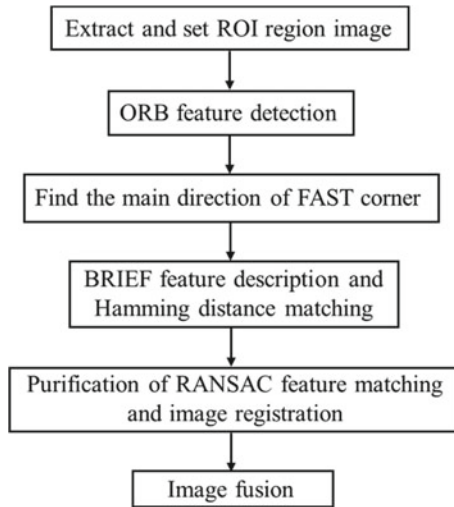


Fig. 1 Algorithm flow of ORB image mosaic based on ROI

invariance [5]; then use the binary robot independent element features (BRIEF) to describe the features, so that the descriptors have certain scale invariance. Finally, through Random Sample Consensus (RANSAC) algorithm, the feature points are purified to find the matching feature points; according to the matching feature points, image registration and image fusion are carried out to realize image splicing.

2.1 Improved Image Matching of ROI

Feature detection and description is a time-consuming part of image mosaic and during image registration; only the feature points in the coincidence areas of different images, which is, the region of interest, are needed. Therefore, if the whole image is matched, the useless feature points outside the overlapped region will consume a lot of time and easily produce mismatches. In this paper, ROI is used to limit image matching to feature points in the region of interest [6], which not only reduces the time of ORB feature extraction, but also reduces the time of matching and mismatching. As shown in Fig. 2, the left and right images are image sequences collected by camera, the coincidence area is the middle part of the two images, the left image's region of interest is the right part, the rest is the uninterested region; similarly, the right image's region of interest is the left part, and the rest is the uninterested region. Generally, the coincidence area of the video frame collected by the camera is 30–60%, In this paper, the camera is installed on the manipulator, and the manipulator will be moved to ensure the coincidence area is about 60%, and 50% of the whole image is considered as ROI area.

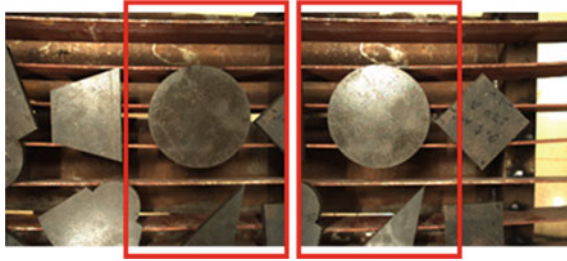


Fig. 2 ROI region selection

2.2 ORB Feature Detection

ORB algorithm uses FAST corner detection to extract feature points. The basic idea of FAST algorithm is that there are enough pixels in the circle neighborhood of a certain radius around the pixel point and the point is in the different area. In gray image, the algorithm can be explained as there are enough pixels whose gray value differs from the point's by more than a certain constant, and then, the pixel point can be considered as a corner point. As shown in Fig. 3, select any pixel point P , and set the pixel value of the point as I_p ; compare the pixel point with the surrounding 16 pixels. If the circle composed of 16 pixels with P as the center has N consecutive pixels, the pixel value is either greater than $I_p + T$ or smaller than $I_p - T$; then, it can be considered as a corner point, where N is generally 9 or 12, and T is the selected threshold.

However, FAST corner detection only compares the gray value of the pixel. Although it has the advantages of simple calculation and fast speed, the feature points detected by FAST do not have scale invariance or rotation invariance. Therefore, it is necessary to calculate the main direction of the feature points so that the algorithm has certain rotation invariance and increases the robustness of the algorithm.

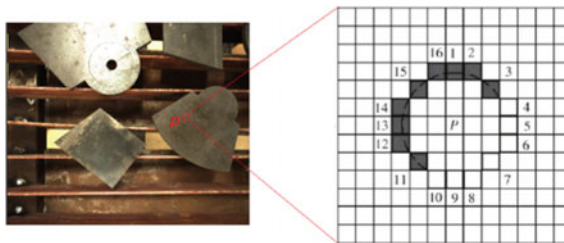


Fig. 3 FAST corner detection

2.3 Finding the Main Direction of Feature Points

In order to make the descriptors obtained by ORB algorithm have rotation invariance, it is necessary to assign a main direction to each feature point. The main direction of FAST corner is calculated by Intensity Centroid [7], which takes the feature point as the center, calculates the position of the center of mass in its neighborhood S , and then constructs a vector with the feature point as the starting point and the center of mass as the end point. The direction of the vector is the main direction of the feature point. The definition is shown in Formula (1):

$$m_{p*q} = \sum_{(x,y) \in S} x^p y^q f(x, y) \quad (1)$$

where p and q are the order of pixel moments in the neighborhood; x and y are the corresponding row and column values; $f(x, y)$ is the gray value of the image, and then, the location of the region's center of mass is:

$$C = \left(\frac{m_{1,0}}{m_{0,0}}, \frac{m_{0,1}}{m_{0,0}} \right) \quad (2)$$

Thus, the direction of the feature points is:

$$\theta = \text{atan}(m_{01}, m_{10}) = \arctan\left(\frac{m_{01}}{m_{10}}\right) = \arctan\left(\frac{\sum_{x*y} yI(x, y)}{\sum_{x*y} xI(x, y)}\right) \quad (3)$$

In order to improve the rotation invariance of the method, it is necessary to ensure that x and y are in the circular region with radius r , which is $x, y \in [-R, R]$, R is equal to the neighborhood radius. After calculating the main direction, the feature points need to be described to prepare for feature point matching.

2.4 Feature Point Description

In ORB, the BRIEF descriptors are used to describe the detected feature points, which solves the primary defect that the BRIEF descriptors do not have rotation invariance.

BRIEF descriptors, which are simple and fast in calculation, contain the main thought that image's neighborhood can provide a relatively small amount of intensity contrast to express.

Define the criterion τ of $S \times S$ size image's neighborhood P as:

$$\tau(p : x, y) = \begin{cases} 1, & p(x) < p(y) \\ 0, & \text{else} \end{cases} \quad (4)$$

where $p(x)$ is the gray value of the image's neighborhood P at $x = (u, v)$ τ after smoothing.

Select n_d sets of (x, y) position pairs, define the binary criterion uniquely, and the BRIEF descriptor is the binary bit string of n_d dimension:

$$f_{nd} = \sum_{1 \leq i \leq 2^{i-1}} \tau(p : x_i, y_i) \quad (5)$$

n_d can be 128, 256, 512, etc. Selecting different values requires a trade-off between speed, storage efficiency and recognition rate. By weighing speed, storage efficiency and recognition rate, n_d in this experiment was set to be 256.

The criterion of image neighborhood only considers a single pixel, which makes its sensitivity toward noise. In order to solve this problem, each test point uses 5×5 sub-windows in the 31×31 -pixel domain, in which the selection of sub-windows follows the Gaussian distribution, and then uses the integral image to accelerate the calculation.

BRIEF descriptors do not have direction or rotation invariance. The solution of ORB is trying to add a direction to BRIEF. For any n pair (x_i, y_i) , define a $2n$ matrix:

$$S = \begin{pmatrix} x_1, x_2, \dots, x_n \\ y_1, y_2, \dots, y_n \end{pmatrix} \quad (6)$$

Using the neighborhood direction θ and the corresponding rotation matrix R_θ , we construct a corrected version of S : $S_\theta : S_\theta = R_\theta S$, then steered BRIEF descriptors will be: $g_n(p, \theta) = f_{nd}(p) | (x_i, y_i) \in S_\theta$.

After obtaining the steered BRIEF, a greedy search is performed to find 256-pixel block pairs with the lowest correlation from all possible pixel block pairs, i.e., the final rotated BRIEF.

2.5 Feature Matching Purification and Image Registration

The feature point detection algorithm described above is used to detect and mark the feature points. The result of feature point matching using Hamming distance is shown in Fig. 4. The connecting points inside figure are the matching feature point pairs in the two images. There are inevitably some mismatches between the feature point pair detected and matched using BRIEF descriptor and Hamming distance. In this paper, RANSAC algorithm is used, and the RANSAC algorithm is a robust parameter estimation algorithm proposed by Fischler and Bons [8].

Image registration is to solve the projection transformation between two images according to the coincidence area of them, i.e., plane homography matrix, so that the images to be spliced under different coordinate systems can be aligned in image space.

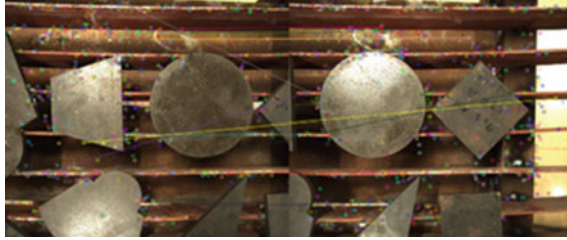


Fig. 4 Show match points

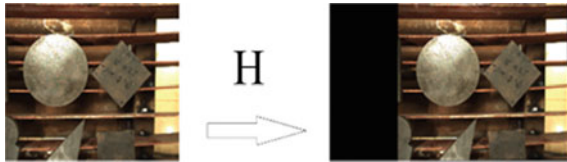


Fig. 5 Image registration

Using matrix H to define the plane homography matrix of two images, $M(x, y)$ and $m(x, y)$ are a set of correctly matched feature point pairs, so the corresponding relationship is:

$$\begin{bmatrix} x'_i \\ y'_i \\ 1 \end{bmatrix} = H \begin{bmatrix} x_i \\ y_i \\ 1 \end{bmatrix} = \begin{bmatrix} h_0 & h_1 & h_2 \\ h_3 & h_4 & h_5 \\ h_6 & h_7 & 1 \end{bmatrix} \begin{bmatrix} x_i \\ y_i \\ 1 \end{bmatrix} \tag{7}$$

According to Formula (6), eight degrees of freedom of H matrix can be solved by four pairs of correct feature points, which means, H matrix can be calculated, and then coordinate transformation can be carried out for the image to be registered. Image registration will be realized by applying H matrix transformation to the corresponding image. The result of applying H matrix change to the image to be matched in the above is shown in Fig. 5, and the left picture in the figure is the one before registration, while the pictures right side are after registration.

2.6 Image Fusion

The images collected by different cameras will inevitably have different light intensity, angles, etc. Thus, the simple application of transformation matrix H for transformation and splicing will produce seams, and the worse images will also have defects such as ghosting, distortion and blur. Then, the image fusion part is set to solve this problem and smooth the seams of image splicing. Generally speaking, the

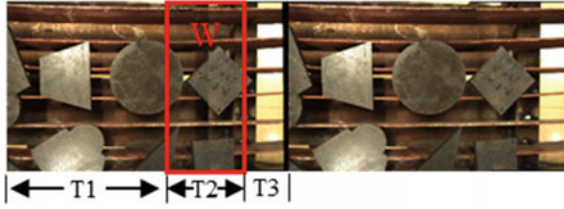


Fig. 6 Before and after image fusion

methods of image fusion include average value method, position weighting method, weighted method with threshold value and Laplace fusion method. Because the camera-moving mode involved in this paper is only translation, position weighting algorithm is adopted [9]. The algorithm complexity is small, and the image fusion effect is good under this condition.

Assuming that $I_1(x, y)$, $I_2(x, y)$ are two images with coincidence areas to be spliced, and the pixels of the fused image are $f(x, y)$, the fusion formula is:

$$f(x, y) = \begin{cases} I_1(x, y) & (x, y) \in T_1 \\ d_1 I_1(x, y) + d_2 I_2(x, y) & (x, y) \in T_2 \\ I_2(x, y) & (x, y) \in T_3 \end{cases} \quad (8)$$

$$\begin{cases} d_1 + d_2 = 1 \\ d_2 = \frac{w_i}{W} \end{cases} \quad (9)$$

d_1, d_2 are the weight values used in the fusion process, w_i is the transverse distance between the current pixel point and the left edge of the coincidence area, W is the total width of the coincidence area of the two images, in this experiment, W was set as 200. T_1 is the value in the left image, T_2 is the value in the coincidence area, and T_3 is the value in the right image. The image is smoothly transitioned by weighting. As shown in Fig. 6, the left image is before image fusion, and the right one is after image fusion. Before image fusion, the stitching trace can be seen clearly. After image fusion using position weighting algorithm, the stitching trace basically disappears that means the success of image fusion.

3 Experimental Results and Analysis

Based on the parameters of the test platform and the requirement of a certain coincidence area between the two images, $3 \times 2 = 6$ images were selected for splicing. Before the images were taken, the optical axis of the camera was adjusted to be perpendicular to the workbench, and the distance that the workbench need to move before and after the two taken adjacent images was determined according to the field

size of the camera and the size that the adjacent images need to be overlapped; then adjusted the camera and lens manually. After the clear image with good contrast could be taken, placed the calibration plate above the workpiece, took the calibration plate image and completed the camera calibration. Finally, the upper left corner of the worktable started to take pictures of the workpieces in blocks. According to the image splicing sequence shown in Fig. 7, the splicing of panoramic images of the large worktable for six images was completed.

Figure 8 shows the six images to be spliced, and Fig. 9 shows the final splicing result. The splicing result is ideal, and the whole splicing process took 3.2 s in debug mode.

As shown in Fig. 9, image correction was carried out for the spliced image. The external and internal participants of the calibrated camera were used to convert the image coordinate system to the world coordinate system. Five lines $L1-L5$ at the junction of the spliced image are taken for accuracy verification. The results were as in Table 1.

According to the calculation results, the error between the length of the line segment in the coincidence area of the mosaic image and the actual length is less than 2 mm, which meets the subsequent needs of the autonomous cutting visual guidance processing.

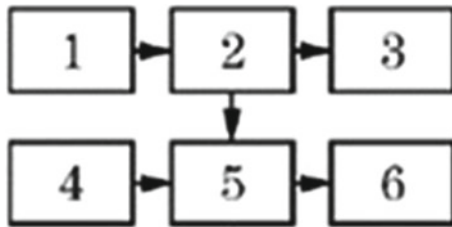


Fig. 7 Splicing method

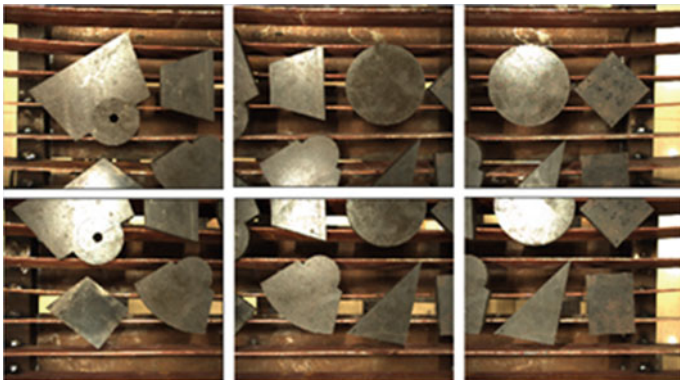


Fig. 8 Six original images to be spliced



Fig. 9 Splicing result

Table 1 Image mosaic accuracy verification (unit: mm)

| Line number | Actual size | Calculated size | Error |
|-------------|-------------|-----------------|-------|
| <i>L1</i> | 112.50 | 111.64 | 0.86 |
| <i>L2</i> | 117.51 | 118.68 | 1.17 |
| <i>L3</i> | 253.52 | 255.19 | 1.67 |
| <i>L4</i> | 137.90 | 139.29 | 1.39 |
| <i>L5</i> | 212.20 | 213.89 | 1.69 |

4 Conclusion

An image mosaic algorithm for large-scale workpiece cutting platform is proposed, which uses ROI to limit the image-matching feature points in the region of interest; use ORB algorithm to extract feature points, determine the main direction of feature points, and describe the detected feature points; use RANSAC algorithm to combine the plane homography matrix estimation method to eliminate the unmatched points to optimize the matching point sets, and carry out image registration; Finally, the position weighting algorithm is used to complete image fusion and realize image splicing. The experimental results show that the accuracy of panorama obtained by splicing meets the requirements of autonomous cutting vision guidance.

Acknowledgements Thanks for National Key Research and Development Program of China (2017YFB1303300) and Project jointly supported by Beijing Natural Science Foundation and Beijing Education Commission (KZ201810017022).

References

1. Liu XL, Chen S (2010) Current status and prospect of shield machine automatic control technology. *J Mech Eng* 46(20):152–160
2. Wang TM (2007) Fully promote Chinese robot technology. *Robot Technol Appl* 2:17–23
3. Xu F (2007) Industrial robot industry status and development. *Robot Technol Appl* 05:20–30
4. Hong Z (2007) Image processing and analyzing-the core of machine vision. *J Appl Opt* 28(1):121–124
5. Zhang YS, Zhou ZR (2013) Remote registration image automatic registration method based on improved ORB algorithm. *Land Resour Remote Sens* 25(3):20–24
6. Shou ZY, Ning OY, Zhang HJ (2013) Real-time video stitching based on SURF and dynamic ROI. *Comput Eng Des* 34(3):998–1003
7. Rosin PL (1999) Measuring corner properties. *Comput Vis Image Underst* 73(2):291–307
8. Li XH, Xie CM, Jia YZ (2013) Fast target detection algorithm based on ORB features. *J Electron Meas Instrum* 27(5):455–460
9. Fei L, Wang WX, Wang XL (2015) Real-time video stitching method based on improved SURF. *Comput Technol Dev* 25(3):32–35

Intelligent Welding Technology for Large Deep and Narrow Shaped Box with Robot



Hu Lan, Huajun Zhang, Jun Fu, Libin Gao, and Rui Pan

Abstract Aiming at the difficulty in customizing the production of shaped boxes in large-scale port lifting equipment, a cantilever welding robot comprised of Cartesian and articulation was developed. Based on field bus technology, a fast parameter programming system suitable for robot welding of shaped box developed. Also, the composite sensing method of laser ranging, wire contact seeking and “bow”-shaped oscillating arc tracking is proposed, which overcomes the difficulty of positional accessibility of deep and narrow lattice space, and the long time and single contact of traditional online/offline task programming. Finally, the internal robot intelligent welding of the large-beam box lifting equipment with a length of about 80 m, a height of about 2.4 m and an internal net width of about 0.6 m realized.

Keywords Marine engineering equipment · Intelligent welding · Parametric programming · Laser sensing

1 Introduction

Marine engineering equipment has important national strategic significance in China’s marine resource development, new energy construction, logistics, port trade, military and other fields. At present, more than 60% of the world’s active port machinery is provided by China, and large port lifting equipment is a product with monopoly advantage of China [1]. Due to the different operating conditions of the marine environment, shipping routes, user terminals, etc., as well as the differences in international standards, national regulations and regional culture, customers’ needs for the design, quality and life cycle of port lifting equipment vary greatly, products face many problems such as high degree of customization, small batch size, strict

H. Lan (✉) · R. Pan

Key Laboratory of Urban Rail Transit Intelligent Operation and Maintenance Technology & Equipment of Zhejiang Province, Zhejiang Normal University, 321005 Jinhua, Zhejiang, China
e-mail: lanhu@zjnu.edu.cn

H. Lan · H. Zhang · J. Fu · L. Gao

Technology Department, Shanghai Zhenhua Heavy Industries Co., Ltd., 200125 Shanghai, China

© Springer Nature Singapore Pte Ltd. 2020

S. Chen et al. (eds.), *Transactions on Intelligent Welding Manufacturing*,

Transactions on Intelligent Welding Manufacturing,

https://doi.org/10.1007/978-981-15-6922-7_8

delivery deadline control and long manufacturing cycle and long supply chain. As a result, flexible intelligent manufacturing is the highlight. As the core load-bearing component of large port lifting equipment, the box has the characteristics of complex structure, thin and long plate, narrow space, diversified welding positions and strict welding requirements. The manufacturing quality of the box directly affects the safety and use effect of the large port lifting equipment in service. Therefore, the research and development of intelligent welding common key technologies such as robot welding technology, equipment and process sensing suitable for large deep and narrow shaped boxes have important promotion and application value, which can also provide reference and support for the technical development of China's large steel structure manufacturing industry.

2 Box Structure Features

The structure of lifting equipment for large ports is shown in Fig. 1. The main structural components such as front/rear beams, upper/lower beams, columns and connecting beams are all in the form of a box, especially the front/rear beams are most typical, as shown in Fig. 2. The whole box section is pentagonal rather than “mouth” shaped, mainly composed of upper/lower wing plates, straight/inclined webs, baffles, angle steel and T-shaped steel. Since this product is customized, the size of the front/rear beams is 52.5–79.5 m long, 1.2–1.4 m wide, and 1.3–2.4 m high, which belongs to a super-shaped steel structure. The thickness of the box wing plate is between 10 and 28 mm, and the thickness of the straight/inclined web is 8–14 mm, the thickness of the baffles is between 8 and 16 mm, the number of baffles of a single beam is between 28 and 41, and the total length of the weld is more than 600 m. The verticality of the box and the baffles before and after welding should all

Fig. 1 Structure of lifting equipment for large ports

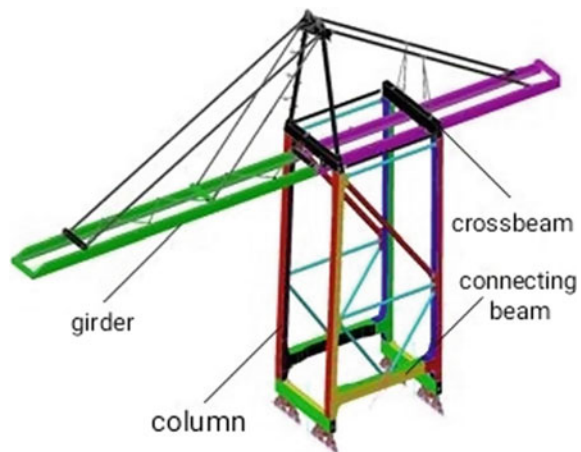
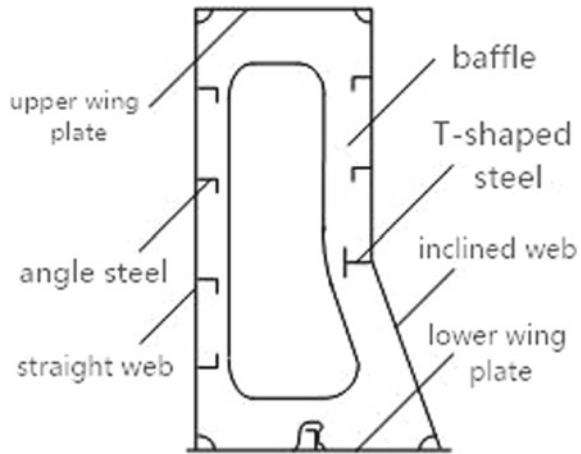


Fig. 2 Structure of boom and girder



be controlled within 3 mm. The straightness at the root position of the web and wing should be controlled within 2 mm/2 m, the (single pass) welding leg size should be 5–8 mm and the deviation on both sides should be controlled within 1 mm. It can be seen that the manufacture of the box structure has the features of large scale, thin plate, many baffles, narrow space, fillet welds and high requirements. It is necessary to develop a special welding robot system suitable for super-large deep and narrow shaped box manufacturing.

3 Automated Robot Welding System for Deep and Narrow Shaped Box

To realize the automatic welding of welds between internal baffles and webs, baffles and wing plates, webs and wing plates, wing plates and angle steel of large-scale port lifting equipment boxes, it is necessary to break through the difficulties of robot position accessibility and posture compliance in super-scale and narrow space, and to develop a compound robot with right angle + articulated cantilever (as shown in Fig. 3). The system is equipped with a total of 10 axes, the robot body has six axes and the external four axes. The working range of the small short-arm robot is about 700 mm, it can flexibly adjust the posture in the space with a clear width of 500–600 mm inside the box. At the same time, in order to make the robot working range cover the maximum size of the beam, the robot adopts external axis linkage in the X- and Z-directions to ensure continuous and efficient welding process, and through the rotation and translation mechanism driven by external servo to achieve workstation assembly and welding cross-operation. The X-axis travel of the cantilever transfer mechanism is 160.0 m, the Y-axis travel is 1.5 m, the Z-axis travel is 2.0 m, and

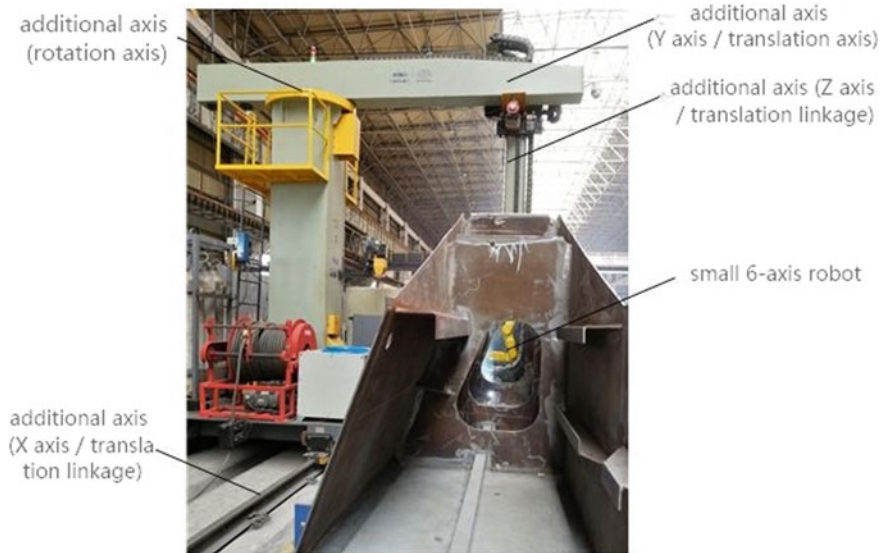


Fig. 3 Cantilever welding robot used for ultra-narrow shaped box

the rotation angle around the Z-axis is 180° . The motion control architecture of the entire system is shown in Fig. 4.

4 Fast Parameter Programming System Suitable for Robot Welding of Shaped Box

Lifting equipment for large port is a customized product. Its beam structure has many specifications, long welds and narrow space. So the teaching workload will be large if the traditional online/offline programming method is used, and the programmer needs to confirm the key points on the robot path one by one, and the potential safety risk is also great. How to realize the rapid intelligent programming for robot welding of such special-shaped box is another bottleneck faced by large-scale steel manufacturing industry [2–5]. According to the characteristics of our products' structure, a software system for batch transmission of structural feature parameters and automatic generation of task programs based on field bus technology was developed. During the actual operation, the programmer only needs to enter the box structure parameters such as beam size (length/width/height), the number of baffles and the spacing of the baffles, baffle feature parameters such as baffles width, height, thickness, angle and welding process parameters such as welding sequence, welding position, welding material type and welding foot size on the upper computer man-machine interface (as shown in Fig. 5). The host computer will set the above parameters to the PLC data register in a pointer way through the local area network, and then, the PLC will

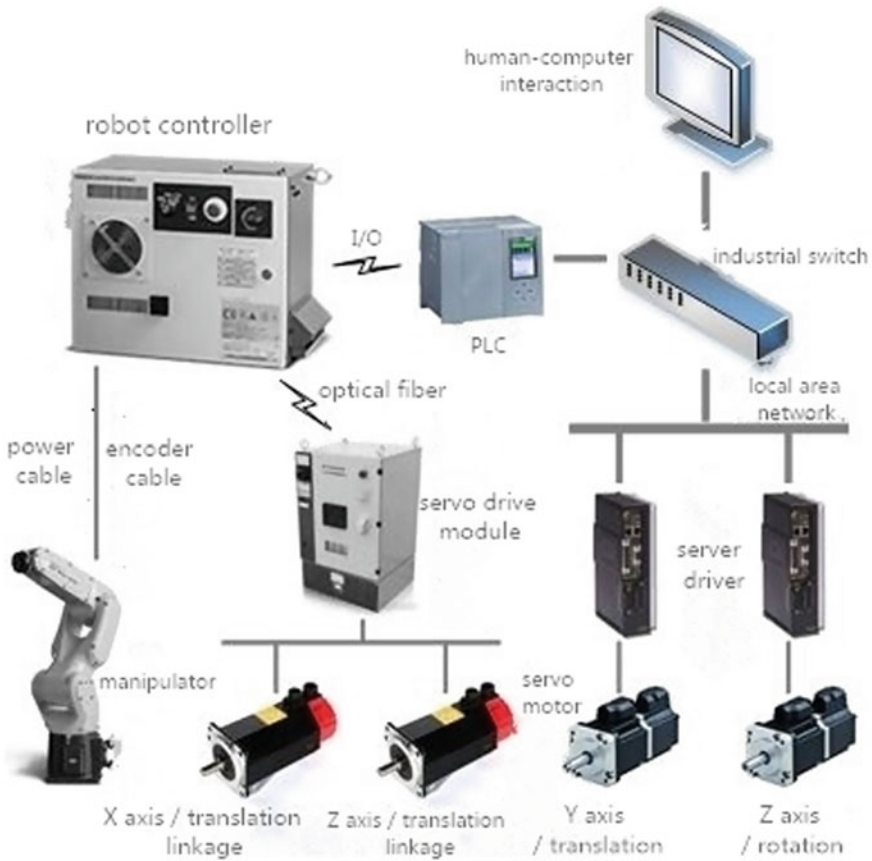


Fig. 4 System architecture of the cantilever welding robot comprised of Cartesian and articulation

send each baffle parameter to the robot controller through the CC-Link communication protocol. After receiving the data, the robot automatically changes the welding program position variable in the internal program library, and the welding expert table is automatically generated by referring to the welding expert library for the welding program to directly call. Through this fast parameter programming system (system architecture is shown in Fig. 6), corresponding program module can be selected according to different product specifications, and the programming time can be shortened to less than 1 h, which solves the problem of long programming time when traditionally welding special-shaped box structures by robots.



Fig. 5 Parametric programming interface for shaped box welding with robot

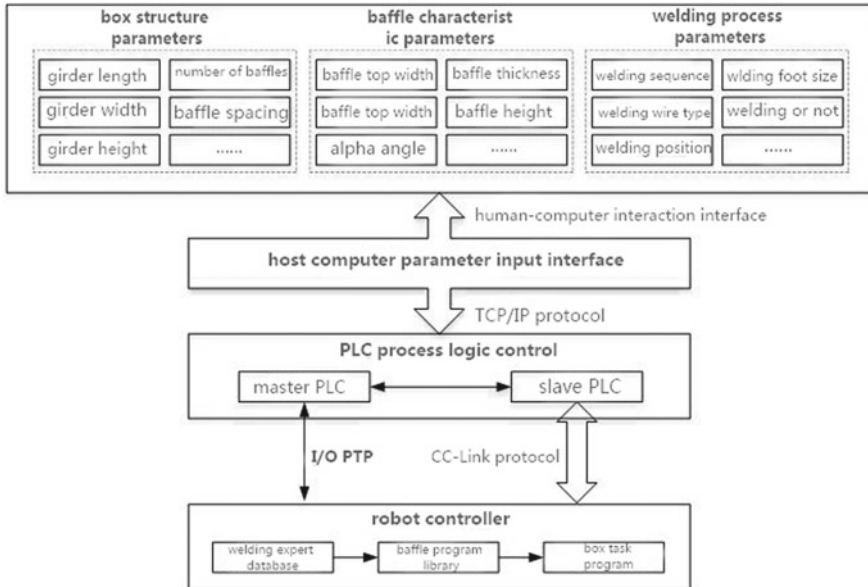


Fig. 6 Data flow of parametric programming for shaped box welding with robot

5 Robot Welding Process and Intelligent Sensor Control Technology of Large Box

In addition to solving the convenience of operating equipment and fast task programming, the automatic welding process and process adaptive control of the special-shaped box of lifting equipment for large port are the third problem faced by the equipment manufacturing industry. It is not difficult to see from Fig. 2 that the baffle plate and the wing plate are T-joint transverse fillet welding (2F), the baffle plate and the web/inclined web are T-joint vertical fillet welding (65° – 90° , 3F). Compared with the 2F position, welding process of the T-joint 3F position is more difficult, and the factors such as processing, assembly errors and welding thermal deformation caused by the thin and long plate of the large box require robot welding to have self-locating and tracking functions, which needs to take into account the adaptability of the process to the working conditions and the ability of the equipment to perceive and correct the working conditions. Contact seeking + arc tracking is the traditional mainstream method basically used to solve this problem. Due to the large number of welds in the box (350–550 welds), if we only rely on the contact of the welding wire or the nozzle of the welding gun to find the starting point of the weld, it is not only time-consuming and inefficient, but also the gun is prone to crash during the positioning process [6–15]; at the same time, the process parameters of the vertical fillet welding are small (welding current 120–140 A), the traditional zigzag vector swings are harmful to the stable acquisition of welding current in arc tracking which will lead to the occurrence of welding deviation, and the deviation of the welding feet on both sides of the fillet weld will exceed 1 mm. For this reason, a new process of medium-thick plate T-joint robots vertical fillet welding is developed using flux cored wire, and the weld seam is well formed (as shown in Fig. 7); the composite sensing method of laser point distance measurement and welding wire contact positioning is proposed. The laser arc sensor is used to perform the rough positioning of the welding arc starting point (with an accuracy of up to 10 mm), and then, the welding arc contact is used to accurately locate the arc starting point. It can effectively shorten the contact positioning empty stroke. The arc tracking process uses the “bow” shape vector swing technology to stably collect the welding current on both sides of the swing position. The above process technology effectively breaks through technical bottlenecks such as the vertical fillet robot welding, long traditional single-contact sensor positioning time, single-laser sensor interference and rifle gun, and the reliability of the tracking process of vertical fillet welding, and have reduced the online preparation time of the task program after the parameterized programming of the robot welding of the box to less than 15 min, realizing the intelligent robot welding in the internal space of the large deep and narrow shaped box.

Fig. 7 Vertical fillet welding of shaped box T-joint with robot



(a) Robot vertical welding



(b) Forming of vertical welding joint

6 Conclusion

1. Developed a right angle + joint compound cantilever robot, which broke through the problem of robot position accessibility in deep and narrow lattice space of super-large shaped box, and realized the robot welding of the box with a length of about 80 m, a height of about 2.4 m and an internal clear width of about 0.6 m for large port lifting equipment.
2. Based on the field bus technology, a robot welding parameter programming system suitable for special-shaped box structures was developed, broke the problem of long time-consuming of traditional online/offline task programming and realized fast and intelligent programming of robot welding for customized large port lifting equipment box.
3. Developed a robot welding process and intelligent sensor control technology suitable for large boxes and proposed a composite sensing method of laser point distance measurement + wire contact positioning + “bow” swing arc tracking, which effectively breaks through technical bottlenecks such as the vertical fillet robot welding, long traditional single-contact sensor positioning time, single-laser sensor interference and rifle gun, and the reliability of the tracking process of vertical fillet welding, realized the intelligent robot welding for large port lifting equipment box.

References

1. Liu E (2018) Review and outlook of the global ocean engineering equipment market. *China Ship Surv* 01:80–86
2. Zhang S, Deng H (2018) Parametric programming process for large parts of aluminum alloy car body. *Metal Working (Metal Cutting)* 2018(06):70–72
3. Xu L (2017) Online intelligent programming system of multiple robots for painting task. Southeast University
4. Wu J (2018) Research on the parameterized programming of macro program based on FANUC0i-MB system. *Digit Technol Appl* 36(01):53–54
5. Du S, Gu W, Liu Y (2018) Intelligent programming for industrial robot based on camera space. *Appl Res Comput* 35(08):2383–2385
6. Wu X (2017) V seam tracking based on a mobile welding robot with double line laser vision sensing. Nanchang University
7. Wang Z (2017) Research on the robot rapid MAG welding process of U steel with large gap. China Academy of Machinery Science and Technology
8. Luo Y, Zhang Z, Zhou C et al (2018) System modeling and simulation of narrow groove GMAW process for oscillating arc sensing. *Trans China Weld Inst* 39(01):5–8
9. Zhang Z (2017) Research on adaptive tracking technology of groove width with swing arc sensor in MAG arc welding. Beijing University of Chemical Technology
10. Sun M, Du S, Tian X et al (2017) Research on double-sided vertical welding process of rack-joining narrow gap robot in intelligent welding workshop. *MW Metal Forming* 10:7–9
11. Lan H (2016) The welding process and metallurgical characteristics of narrow gap MAG welding of thick Q690E steel at vertical position with arc swinging and shifting. Harbin University of Science and Technology

12. Niu M (2017) Analysis of forming and sensing characteristics of narrow gap welding at vertical position. Tianjin Polytechnic University
13. Zhao T, Zhang H, Li L et al (2017) Welding process of light turbine generator case with box structure. *Mech Eng* 2017(01):253–254
14. Liu X, Chen X, Chen H et al (2016) Weld planning and robot welding system development based on laser vision sensing for ship profiles. *J Shanghai Jiaotong Univ* 50(S1):44–46
15. Ding B, Guo X, Chen X (2016) Research on automatic vertical fillet welding process and application value analysis in hull construction. *MW Metal Forming* 14:69–71

Optimization of Laser Deep Penetration TIG Hybrid Welding Technology for Stainless Steel



Jialei Zhu, Wei Li, Zhibo Li, Xiangdong Jiao, Cong Feng, and Kai Wang

Abstract The experiment is carried out on the stainless steel with a thickness of 4 mm. A laser deep penetration TIG hybrid welding machine is used in hybrid welding. The influence of main process parameters on weld forming is analyzed, and high-quality weld joint is obtained. The results show that to ensure that other welding parameters remain unchanged. At the space 0–2 mm, the defocus –1.5–0 mm, weld is good. At the laser power 3 Kw, the arc current 270 A, the velocity 1.2 m/min, the tensile strength of the joint reached up to 99.44%, and hardness is higher than base metal.

Keywords Laser-arc hybrid welding · Welding speed · Stainless steel

1 Introduction

Stainless steel has a decisive position in the industrial field [1]. Among them, austenitic stainless steel, as the main steel, has good corrosion resistance, good mechanical properties, and strong moldability. As a typical austenitic stainless steel, 304 stainless steel has a wide range of applications in engineering structures such as nuclear power, underwater oil production platforms, and subsea oil pipelines [2]. Scholars at home and abroad have made a detailed study on the welding methods and welding characteristics of 304 stainless steel. Li et al.'s finds of Harbin Institute of Technology [3] carried out an underwater wet welding test on 304 stainless steel using self-protected nickel strip flux-cored wire and analyzed the microstructure and

J. Zhu (✉) · W. Li · X. Jiao · C. Feng · K. Wang
School of Mechanical Engineering, Beijing Institute of Petrochemical Technology, 102617
Beijing, China
e-mail: zhujialei@bipt.edu.cn

W. Li · C. Feng · K. Wang
College of Electrical and Mechanical Engineering, Beijing University of Chemical Technology,
100029 Beijing, China

Z. Li
Tangshan Kaiyuan Welding Automation Technology Institute Co., Ltd., 063000 Tangshan, China

mechanical properties of the welded joint; Han et al. find [4] the thickness of 304 stainless steel plate with 5 mm thickness was welded by laser-MIG hybrid welding. The effect of laser-wire distance on weld formation and mechanical properties was studied, and the mechanism of arc on microstructure and microhardness of weld was analyzed. The results show that the laser-wire distance affects the synergistic effect between the laser heat source and the arc heat source and the stability of the droplet transfer. When the laser-wire distance is 1 mm, the droplet transfer is stable and the weld is well formed. Su et al. finds of Tianjin University [5] used pulse melt inert-gas welding (MIG) to weld 304 stainless steel. The signal acquisition system and high-speed camera perform synchronous acquisition to study the droplet transition. The results show that the addition of laser improves the welding quality and welding efficiency; Zhang et al. finds of Tsinghua University [6] adopted laser-MIG arc hybrid welding method, and the research object was SUS444 ferrite with gap of 0.5 mm and thickness of 1 mm. The butt joint has a good welding seam forming quality, and the limit welding speed of penetration can reach 12 m/min, while the limit welding speed of the lap joint is 5 m/min. In 1997, the Commonwealth Scientific and Technological Research Organization of Australia improved TIG welding and invented the keyhole TIG (K-TIG) welding method [7]. K-TIG welding has a tungsten current-carrying capacity of 300 A or higher [8]. It can realize single-sided welding and double-sided forming on 3–6 mm stainless steel plates without gaskets. The welding process is stable [9, 10]. K-TIG welding is a small hole welding similar to plasma welding, but K-TIG welding equipment is less expensive than plasma arc welding equipment, welding costs are low, and welding automation is easier to achieve [11]. Laser deep penetration TIG hybrid welding is similar to laser plasma hybrid welding, and its main advantage is high-speed welding of thin plates. With regard to this type of hybrid welding, domestic scholars have also made related research. Li et al. finds of Hunan University of Science and Technology [12] aimed at high-power laser deep penetration welding of 304 austenitic stainless steel, the quality of the weld is poor, and a “nail head” is easily formed. At the same time, the welding speed, defocus amount, and side blow protection were studied. The influence of the air nozzle diameter on the weld morphology was also studied. The effect of adding active sulfur powder on the weld pool and the effect on the formation of the weld seam were also studied. The results show that the optimization of welding process parameters and the addition of active powder are the effective method of welding to controlling “nail heads”. This paper mainly studies the process optimization of laser deep-melting TIG arc hybrid high-speed welding of stainless steel.

Table 1 Chemical composition of 304 stainless steel

| Grade | C | Si | Mn | P | S | Cr | Ni |
|----------|--------|--------|--------|--------|--------|--------|--------|
| 0Cr18Ni9 | 0.0436 | 0.5020 | 1.1274 | 0.0301 | 0.0021 | 17.245 | 8.0520 |

Table 2 Mechanical properties of 304 stainless steel

| Project | Stretching test | | | Hardness test |
|----------|--------------------|------------------|------------|---------------|
| Property | Yield strength 0.2 | Tensile strength | Elongation | HV |
| Value | 274 | 642 | 58% | 164 |

2 Experimental Program

2.1 Experimental Materials

The experimental material used a 4 mm-thick 304 stainless steel plate with a plate size of 150 mm × 130 mm and a thickness of (4 ± 0.1) mm. The chemical composition and mechanical properties of 304 stainless steel are shown in Tables 1 and 2.

2.2 Experimental Equipment and Methods

The laser deep-melting TIG hybrid welding experimental system is mainly divided into four parts: laser-integrated equipment, deep-melting TIG welding equipment, motion table, and high-speed camera acquisition equipment, as shown in Fig. 1. Among them, the laser equipment is the YSL-4000 laser produced by the United States IPG company, the largest fiber laser manufacturer. Panasonic YC-500WX welding machine is used for deep-melting TIG welding machine, and the rated current

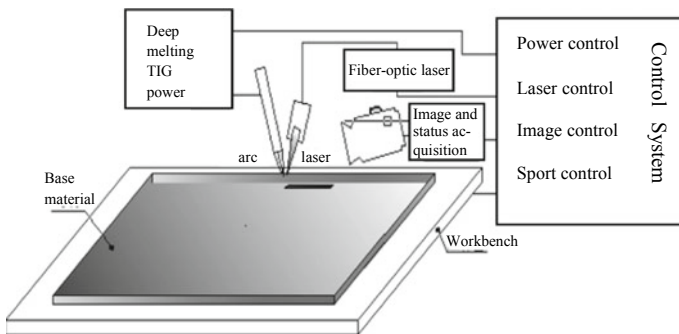
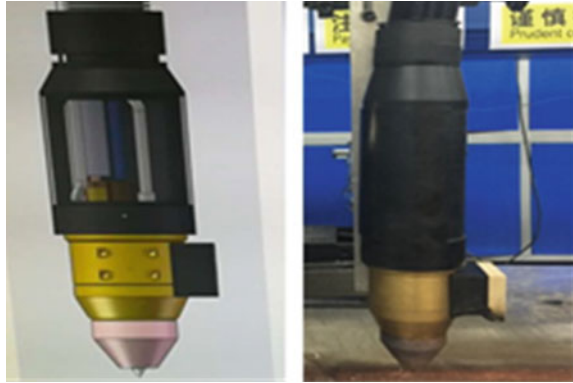


Fig. 1 Experiment system of laser deep TIG hybrid welding

Fig. 2 Three-dimensional map and physical map of deep TIG welding torch



is 500 A. The welding torch is a deep-melting TIG welding torch independently developed by Tangshan Kaiyuan, as shown in Fig. 2.

2.3 *Experimental Process*

A schematic diagram of the welding process is shown in Fig. 1. The welding torch and laser are compound with a range axis, each inclined at 15° . The energy output of the two is always on a straight line. The laser is in the front, and the arc is behind. The different welding parameters are grouped in Table 3. The variables in the hybrid process are laser power, welding current, welding speed, defocus amount, and heat source distance.

3 Experimental Results and Analysis

3.1 *Influence of Process Parameters on Weld Formation*

For 4 mm stainless steel laser deep-melting TIG single-sided welding and double-sided forming process, the matching value of laser power and arc current is very important. For example, Chen et al. of Huazhong University of Science and Technology [13] studied the welding penetration of MAG and YAG laser hybrid welding at different currents with laser power. Experiments have concluded that when the laser power exceeds 1.5 Kw and the arc current is 157 A, the maximum penetration depth is obtained. However, when the current is 200 A, the obtained penetration is equivalent to that obtained by laser welding. In addition, the laser-arc hybrid welding with a large welding current does not have a tendency to reduce welding spatter and a tendency to increase penetration during the welding process. It can be




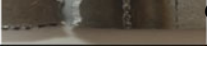
Table 3 Experimental parameters

| Number | La- ser pow er P_L | Weld- ing cur- rent I | Weld- ing speed V | Defocus amount Δf | Heat source dis- tance D_{LA} | Heat Input | Welding surface forming |
|--------|-------------------------------|----------------------------------|------------------------------|---------------------------------|---|---------------|-------------------------|
| | Kw | A | m/min | mm | mm | KJ/m^2 | |
| 1 | 4 | 0 | 2 | 0 | 0 | 0.12 | |
| 2 | 4 | 150 | 1.8 | 0 | 0 | 0.20 | |
| 3 | 4 | 180 | 2 | 0 | 0 | 0.18 | |
| 4 | 4 | 180 | 2 | 0 | 1 | 0.18 | |
| 5 | 4 | 180 | 2 | 0 | 2 | 0.18 | |
| 6 | 4 | 180 | 2 | 0 | 3 | 0.18 | |
| 7 | 4 | 180 | 2 | 0 | 4 | 0.18 | |
| 8 | 4 | 180 | 2 | 0 | 5 | 0.18 | |
| 9 | 4 | 180 | 2 | -1.5 | 0 | 0.18 | |
| 10 | 4 | 180 | 2 | -5 | 0 | 0.18 | |
| 11 | 4 | 180 | 2 | 1.5 | 0 | 0.18 | |
| 12 | 4 | 180 | 2 | 5 | 0 | 0.18 | |
| 13 | 3 | 270 | 1.2 | 0 | 0 | 0.40 | |
| 14 | 2.5 | 250 | 1 | 0 | 0 | 0.34 | |

seen that there is a large difference in parameter adjustment between laser-arc hybrid welding and conventional welding methods, which requires a detailed exploration. In addition, the two heat sources of laser and deep penetration TIG belong to deep penetration welding of small holes, and the recombination process of the two is more complicated.

As can be seen in Table 3, the experiment obtained a total of four sets of valid data, and the weld surface was free of any defects: $P_L = 4 Kw, I = 150 A, V =$

Table 4 Results of tensile testes

| Sample No | Morphology after breaking test | Tensile strength /MPa | Achieving base material performance percentage /% | Fracture location |
|-----------|---|-----------------------|---|--------------------|
| 2 |  | 614.688 | 95.75% | Heat affected zone |
| 3 |  | 635.42 | 99.12% | Base material |
| 13 |  | 638.333 | 99.44% | Base material |
| 14 |  | 630.56 | 98.22% | Base material |

1.8 m/min; $P_L = 4$ Kw, $I = 180$ A, $V = 2$ m/min; $P_L = 3$ Kw, $I = 270$ A, $V = 1.2$ m/min and $P_L = 2.5$ Kw, $I = 250$ A, $V = 1$ m/min.

On this basis, the influence of the distance between the heat source and the amount of defocus on the formation of the weld seam is explored. The experimental data are 5–13 groups. When other welding parameters are kept constant, the welding seam is well formed when the heat source distance is 0–2 mm; when the heat source distance is 3 mm, the spatter is large, but the formation is good; when the heat source distance is 4–5 mm, the concave of the front side of the weld is increased. There are spatters during welding, but the back penetration is good; when the spacing gradually increases, the back penetration starts to be uneven. When other welding parameters are not changed, when the defocus amount is -1.5 – 0 mm, the weld seam is well formed.

3.2 Tensile Properties of Welded Joints

Table 4 shows the test results of the tensile properties of the welded joints of the above four sets of valid data. It can be known from the table that three groups of the four effective parameters of the welded joint are subjected to the tensile test fracture position of the base metal, and the tensile strength can reach a maximum of 99.44% of the performance of the base metal.

3.3 Hardness Analysis

The hardness of a material refers to the ability of a metal to resist elastic deformation, plastic deformation, or cracking within a small surface or volume. It can reflect a

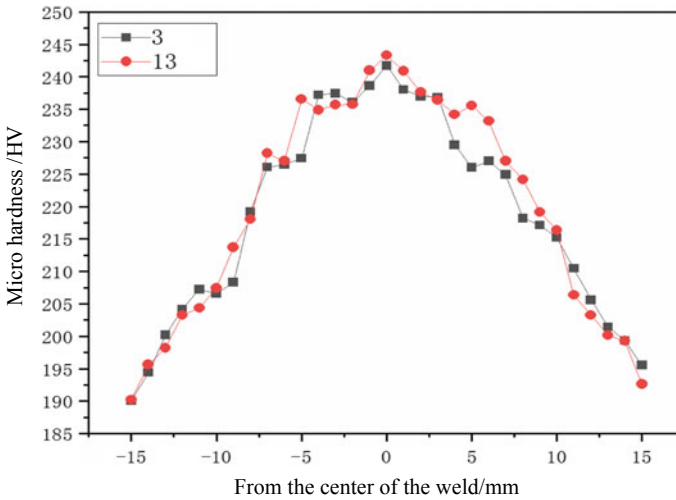


Fig. 3 Hardness graph of welded joint

series of different mechanical performance indicators such as elasticity, strength, plasticity, and toughness. In addition to the above mechanical properties, the hardness of welded joints can also characterize the uniformity of the weld structure distribution after welding and the distribution of some special phases [14]. Figure 3 shows the hardness distribution of 304 stainless steel welded joints in groups 3 and 13.

It can be seen from Fig. 3 that the hardness of the portion near the center of the weld in the laser deep-melting TIG welding joint is the highest, the hardness away from the center of the weld gradually decreases, and the heat-affected zone 3 reflected by the image is wider, more than about 1 cm. Corresponding to the morphology of composite welded joint. The weld seam has a higher hardness than the base metal.

4 Conclusion

1. For laser deep penetration TIG hybrid welding of 4 mm stainless steel, the matching value of laser power and arc current is very important. In this experiment, a total of four effective parameters were obtained.
2. Under the condition that other welding parameters are unchanged, the welding seam is well formed when the heat source distance is 0–2 mm and the defocus amount is $-1.5 - 0$ mm.
3. The hybrid welding parameters are obtained when the laser power is 3 Kw, the arc current is 280 A, the welding speed is 1.2 m/min, or the laser power is 4 Kw, the arc current is 180 A, and the welding speed is 2 m/min. The welded joint has a tensile strength of more than 99% of the base metal and a higher hardness than the base metal.

References

1. Li L, Zhang X, Liu H et al (2013) Production technology and application of stainless steel clad plate. *Steel Roll* 30(3):43–47
2. Wang L, Chong W (2013) Stainless steel welding technology and its engineering application. *Intelligence* (5)
3. Li H, Liu D, Yu Y et al (2017) Underwater wet welding process of 304 stainless steel. *Trans China Weld Institut* 38(9):5–8
4. Han L, Cai D, Zhang Y et al (2018) Influence of laser-arc distance on joint of 304 stainless steel by laser-mig hybrid welding. *Laser Optoelectr Prog* 55(6)
5. Su Z, Li H, Wei H et al (2016) Improvement of laser on metal transfer in pulsed MIG welding. *Trans China Weld Institut* 37(9):91–95
6. Zhou Z, Shan J, Wu A et al (2015) Study on high speed laser-MIG hybrid welding for large gap joint of stainless steel sheet. *Trans China Weld Institut* 36(10):109–112
7. Zhang R, Li H, Li M, Wang R, Leng X (2012) Numerical analysis on keyhole gas tungsten arc welding. *Electr Weld Mach* 42(12):7–11
8. Fan W, Luo Z, Feng Y, Li Y, Ao S (2016) Study on the deep penetration TIG welding of Q345 steel. *J ShangHai Jiao Tong Univ* 50(S1):102–105
9. Li H (2011) Numerical analysis on keyhole gas tungsten arc welding. *Lanzhou University of Technology*
10. Vinogradov VA, Stchavelev LN, Popenko AV (1991) Power density stabilization system in argon tungsten-arc welding. In: *Proceedings of the international conference, Beijing, China*, pp 49–54
11. Jarvis BL, Ahmed NU (2000) Development of keyhole mode gas tungsten arc welding process. *Sci Technol Weld Join* 5(1):1–7
12. Li S, Liao S, Chen G (2017) Study on appearance of weld during deep-penetration laser welding of 304 stainless steel 07(8):681–689
13. Li C, Dong C, Lu G et al (2004) Research on YAG laser/MAG arc hybrid welding. *Weld Technol* 33(4):21–23
14. Xue F, Yu W, Wang Z et al (2012) Evaluation of thermal aging effect on primary pipe material in nuclear power plant by micro hardness test method. *Atom Energy Sci Technol* 46(7):809–814

Information for Authors

Aims and Scopes

Transactions on Intelligent Welding Manufacturing (TIWM) is authorized by Springer for periodical publication of research papers and monograph on intelligentized welding manufacturing (IWM).

The TIWM is a multidisciplinary and interdisciplinary publication series focusing on the development of intelligent modelling, controlling, monitoring, and evaluating and optimizing the welding manufacturing processes related to the following scopes:

- Scientific theory of intelligentized welding manufacturing
- Planning and optimizing of welding techniques
- Virtual & digital welding /additive manufacturing
- Sensing technologies for welding process
- Intelligent control of welding processes and quality
- Knowledge modeling of welding process
- Intelligentized robotic welding technologies
- Intelligentized, digitalized welding equipment
- Telecontrol and network welding technologies
- Intelligentized welding technology applications
- Intelligentized welding workshop implementation
- Other related intelligent manufacturing topics.

Submission

Manuscripts must be submitted electronically in WORD version on online submission system: <https://ocs.springer.com/ocs/en/home/TIWM2017>. Further assistance can be obtained by emailing Editorial Office of TIWM, Dr. Yan ZHANG: zm_1977nsh@163.com, or anyone of the Editors-in-chief of TIWM.

Style of Manuscripts

The TIWM includes two types of contributions in scopes aforementioned, the periodical proceedings of research papers and research monographs. Research papers include four types of contributions: Invited Feature Articles, Regular Research Papers, Short Papers and Technical Notes. It is better to limit the full-length of Invited Feature Articles in 20 pages; Regular Research Papers in 12 pages; and Short Papers and Technical Notes both in 6 pages. The cover page should contain: Paper title, Authors name, Affiliation, Address, Telephone number, Email address of the corresponding author, Abstract (100–200 words), Keywords (3–6 words) and the suggested technical area.

Format of Manuscripts

The manuscripts must be well written in English and should be electronically prepared preferably from the template “splsproc1110.dotm” which can be downloaded from the website: <https://rwlab.sjtu.edu.cn/tiwm/index.html>. The manuscript including texts, figures, tables, references, and appendixes (if any) must be submitted as a single WORD file.

Originality and Copyright

The manuscripts should be original, and must not have been submitted simultaneously to any other journals. Authors are responsible for obtaining permission to use drawings, photographs, tables, and other previously published materials. It is the policy of Springer and TIWM to own the copyright of all contributions it publishes and to permit and facilitate appropriate reuses of such published materials by others. To comply with the related copyright law, authors are required to sign a Copyright Transfer Form before publication. This form is supplied to the authors by the editor after papers have been accepted for publication and grants authors and their employers the full rights to reuse of their own works for noncommercial purposes such as classroom teaching etc.

Author Index

B

Bai, Lanlan, 101

C

Cao, Yingyu, 101

Chen, Bo, 61

Chen, Shanben, 3

F

Fan, Ding, 35

Feng, Cong, 73, 123

Feng, Jicai, 61

Feng, Zhiqiang, 83

Fu, Jun, 113

G

Gao, Libin, 113

Guo, Wenwen, 47

H

Han, Junfeng, 83

Huang, Jiankang, 35

Huang, Jiqiang, 47, 101

Huang, Junfen, 47, 101

J

Jiao, Xiangdong, 73, 123

Jiao, Ziquan, 83

L

Lan, Hu, 113

Li, Nan, 35

Li, Wei, 73, 123

Li, Zhibo, 73, 123

M

Ma, Chengyuan, 61

P

Pan, Rui, 113

Q

Qin, Yong, 83

S

Shi, Nanhui, 83

Song, Xiaoguo, 61

T

Tan, Caiwang, 61

W

Wang, Jizong, 47

Wang, Kai, 123

Wei, Xian, 83

X

Xi, Jianting, 101

Xue, Long, 47, 101

YYuan, Wen, [35](#)Yu, Shurong, [35](#)**Z**Zhang, Huajun, [113](#)Zhang, Zhengyu, [101](#)Zhu, Jialei, [73](#), [123](#)Zou, Yong, [47](#)